

Ca(OH)<sub>2</sub>/CaO Chemical Heat Pump for Thermoamplification in  
Integrated Energy Systems: Thermodynamic Modeling, Experimental  
Investigations, and Techno-Economic Analysis

A Dissertation

Presented in Partial Fulfillment of the Requirements for the  
Degree of Doctor of Philosophy

with a

Major in Chemical Engineering

College of Graduate Studies

University of Idaho

by

Aman Gupta

Approved by:

Major Professor: Vivek Utgikar, Ph.D.

Committee Members: Piyush Sabharwall, Ph.D, Brian M. Fronk, Ph.D,

Wudneh Admassu, Ph.D.

Department Administrator: Dev Shrestha, Ph.D.

August 2022

## Abstract

The energy economy is continually evolving in response to socio-political factors in the nature of primary energy sources, their conversions to useful forms such as electricity and heat, and their utilization in different sectors. Nuclear energy has a crucial role to play in the evolution of energy economy due to its clean and non-carbon-emitting characteristics. Integrated Energy Systems (IES) are collaboratively controlled systems may dynamically apportion thermal and/or electrical energy to promote the production of various energy products, and have potential to reduce GHG emissions, improve energy efficiency, improve electrical grid dependability, and enhance energy economics. The reversible decomposition reaction of  $\text{Ca(OH)}_2$  has attracted wide attention and research for thermochemical energy storage system (TCES). Chemical Heat Pump (ChHP) or temperature amplification aspect of the system was not studied in detail in the literature. In this work, thermodynamic modeling, experimental investigation and techno-economic analysis were conducted. A refinement of the equilibrium relationship between pressure and temperature governing the reversible reaction is presented by incorporating temperature dependence of the thermodynamic properties and the effect of non-ideality in the vapor phase. The results showed the temperature dependence of enthalpy influences the equilibrium and the non-ideality in vapor phase can become significant at pressures greater than 2 MPa. The refined relationship predicts higher equilibrium pressures for any temperature than those equilibrium relationships that neglect the temperature dependence of thermodynamic quantities. Thermogravimetric analyzer was used to perform kinetic analysis of pure  $\text{Ca(OH)}_2$  decomposition at various temperatures, yielding kinetic parameters - activation energy and Arrhenius constant with derived rate control equations for isothermal and non-isothermal conditions.  $\text{CaTiO}_3$  is added to  $\text{Ca(OH)}_2$  at different compositions to enhance kinetic parameters in form of composite pellets which showed significant increase in activation energy and Arrhenius constant values. Repeated dehydration-hydration cycles were conducted in a bench scale reactor system under various reaction conditions. The experiments were firstly conducted with powdered and pelletized  $\text{Ca(OH)}_2$  and then with composite pellets comprising inert agent. It was found that the temperature rise during hydration reaction was dependent on the extent of conversion during the dehydration process. Visual and scanning electron microscopic examinations of the product after each

reaction revealed structural changes and formation of cracks in the  $\text{Ca(OH)}_2$  pellets but no cracks were developed after 20 cycles when composite pellets we used. A techno-economic analysis was undertaken to establish the viability of selling heat along with electricity for an advanced  $100 \text{ MW}_{\text{th}}$  small modular reactor (SMR) and four nuclear hybrid energy system (NHES) configurations featuring the SMR paired with chemical heat pump (ChHP) systems providing a thermal output ranging from 1 to  $50 \text{ MW}_{\text{th}}$ . Net present value, payback period, discounted cash flow rate of return and levelized cost of energy were evaluated for these systems for different regions of U.S. reflecting a range of electricity and thermal energy costs. The analysis indicated that selling heat to high temperature industrial processes showed profitable outcomes compared to the sale of only electricity. Higher carbon taxes improved the economic parameters of the NHES alternatives significantly. Providing heat to high temperature industries could be very beneficial, helping to cut down the greenhouse gases emission by reducing the fossil fuel consumption.

## Acknowledgments

Throughout my four-year Ph.D. journey, I have been fortunate to receive a lot of help and guidance from so many people. I hope the mixed feelings can accompany me on a more exciting journey, and that everyone I've met is well and happy on their colorful journeys.

I had the unique opportunity to pursue my graduate research I felt passionate about, with the support of Dr. Vivek Utgikar. Dr. Utgikar is a great advisor and instructor in many aspects, so I have luckily had an exciting and enjoyable Ph.D. journey. The broad perspective and open mind of Dr. Utgikar enriched my research experience with a variety of interesting topics. In Dr. Utgikar's Lab, I have enjoyed exploring all kind of scientific and engineering problems. The group's highly diverse research topics and cultural backgrounds have created an excellent environment for my graduate studies. I am grateful to all of my colleagues, as well as Dr. Utgikar, for creating such an environment. My mentor and committee member from INL, Dr. Piyush Sabharwall, has always encouraged me to expand upon the project goals, challenging me to come up with novel ideas and to incorporate ideas and input from collaborators at other universities as well. I feel grateful for the interactions with my other committee member Dr. Brian M. Fronk from collaborated university (Oregon State University). Dr. Fronk's views and expertise on my research were always valuable. I would like to thank Dr. Wudneh Admassu my committee member for his guidance, help and giving thoughtful feedback on my research work. I would like to thank Paul D. Armatis for being awesome colleague, sharing his views on the project and helping me out. I really enjoyed our long technical discussions.

This work would not have been possible without all the technical help and advice received from Dr. Dave MacPherson and Charles Cornwall. I would like to thank the rest of the Chemical and Biological department including Judy Vandegrift, Gail Bergman and Margaret Baker who had always been extremely supportive during my graduate years.

I would like to thank U.S Department of Energy Nuclear Energy University Program (Award Number DE-NE0008775) for funding this project.

## **Dedication**

My parents, Ajay Gupta and Suman Gupta, have been the people who care about me the most. Thank you for giving me everything. I would like to thank my friends and close ones

Anubhav, Ankit, Samiksha, JoLeigh, Aayush, Sagarika, Tushar, Ranjitha, Chaithanya, Tejaswini, Rashmi, Anumeha, Ketan and Moorti for their constant support. This dissertation is dedicated to my family, my friends and all my professors who helped me in my tough times to finish my Ph.D.

## Table of Contents

Abstract.....	ii
Acknowledgments.....	iv
Dedication.....	v
List of Tables .....	ix
List of Figures .....	x
Chapter 1 Introduction .....	1
1.1 Nuclear Energy Current Status.....	1
1.2 Integrated Energy System .....	2
1.3 Chemical Heat Pump.....	4
1.4 SMR and ChHP Economics .....	7
References .....	9
Chapter 2 Thermodynamic Modeling of $\text{Ca(OH)}_2/\text{CaO}$ Reversible Reaction System.....	13
2.1 Objective .....	13
2.2 Thermodynamic Analysis .....	14
2.2.1 Temperature dependence of thermodynamic properties .....	14
2.2.2 Non-ideality in vapor phase.....	18
2.3 Results and Discussions .....	19
2.3.1 Non-ideality in vapor phase.....	20
2.3.2 Incorporating temperature dependence on enthalpy.....	22
2.3.3 Implication of the Derived Clausius-Clapeyron Equilibrium on $\text{Ca(OH)}_2/\text{CaO}$ and ChHP System.....	27
Nomenclature .....	29
References .....	32
Chapter 3 Kinetic Modeling of $\text{Ca(OH)}_2$ Decomposition.....	33
3.1 Objective .....	33

3.2 Materials and Methods .....	33
3.2.1 Reagents and apparatus .....	33
3.2.2 Experimental Procedure .....	34
3.2.3 Composite Material Synthesis .....	35
3.2.4 Ca(OH) <sub>2</sub> Pellet Enhancement Concept .....	35
3.3 Results and Discussions .....	36
3.3.1 Isothermal Decomposition of Pure Ca(OH) <sub>2</sub> .....	36
3.3.2 Kinetics of Decomposition of Ca(OH) <sub>2</sub> .....	39
3.3.3 Kinetic of Decomposition of Ca(OH) <sub>2</sub> in Composite Ca(OH) <sub>2</sub> :CaTiO <sub>3</sub> Pellets ....	46
3.3.4 Comparison of kinetic parameters for Ca(OH) <sub>2</sub> and composite pellet with reported data.....	54
3.3.5 Structure and Mechanical Compressive Strength Analysis.....	55
Nomenclature .....	56
References .....	58
Chapter 4 Cyclability Study of Ca(OH) <sub>2</sub> /CaO Dehydration-Hydration Reaction at Bench-Scale .....	59
4.1 Objective .....	59
4.2 Experimental Investigation .....	59
4.2.1 Experimental Setup.....	59
4.2.2 Experimental Procedure .....	61
4.2.3 Experimental Data Analysis .....	63
4.3 Results and Discussion.....	64
4.3.1 Thermal Gravimetric Analysis .....	64
4.3.2 Preliminary Experimental Results and Analysis of Pure Ca(OH) <sub>2</sub> Pellets.....	68
4.3.3 Pure Ca(OH) <sub>2</sub> Pellet vs Powder Comparison .....	80
4.3.4 Experimental Results on Composite Pellet (1:0.5 :: Ca(OH) <sub>2</sub> :CaTiO <sub>3</sub> ).....	88

References .....	94
Chapter 5 Preliminary Pilot-Scale Study and Techno-Economic Analysis of Chemical Heat Pump .....	95
5.1 Objective .....	95
5.2 Scalability Study of Chemical Heat Pump .....	95
5.2.1 Literature Review of Pilot-Scale Study .....	96
5.2.2 Pilot Plant Design .....	107
5.2.3 Thermal Calculations.....	108
5.3 Techno-Economic Analysis .....	113
5.3.1 Methodology.....	113
5.3.2 Study Approach and Assessment Scenarios .....	119
5.4 Results and Discussion.....	122
5.4.1 Economic Parameter Analysis.....	123
5.4.2 Parametric Study on Overnight Capital Cost of Advanced SMR .....	127
5.4.3 Impact of Increased Carbon Taxes .....	131
Nomenclature .....	135
References .....	138
Chapter 6 Summary and Conclusions.....	141
6.1 Conclusions .....	141
6.2 Future Considerations .....	143

## List of Tables

Table 2.1 Reported Clausius-Clapeyron equilibrium relation for $\text{Ca(OH)}_2/\text{CaO}$ system.....	13
Table 2.2 Values of Parameters in Eq. 2.3.....	15
Table 2.3 Parametric Values of constants in Eq. 2.4 .....	16
Table 2.4 Comparison of equilibrium pressure values at different temperatures .....	26
Table 3.1 Chemical composition of $\text{Ca(OH)}_2$ and $\text{CaTiO}_3$ .....	34
Table 3.2 Comparison of % mass change of pure $\text{Ca(OH)}_2$ at different decomposition temperature .....	37
Table 3.3 Rate constant for $\text{Ca(OH)}_2$ decomposition as a function of temperature .....	41
Table 3.4 Comparison of time required to achieve respective conversion at different maximum temperature .....	50
Table 3.5 Rate constant for 1:0.5 and 1:1 $\text{Ca(OH)}_2:\text{CaTiO}_3$ decomposition as a function of temperature .....	53
Table 3.6 Comparison of kinetic parameters of pure $\text{Ca(OH)}_2$ and composite pellet .....	54
Table 3.7 Compressive strength of $\text{Ca(OH)}_2$ and composite pellets before decomposition...	56
Table 4.1 Percentage mass loss and reaction enthalpy of $\text{Ca(OH)}_2$ at different heating rate .	66
Table 4.2 Reaction enthalpies during dehydration at different decomposition temperatures for $\text{Ca(OH)}_2/\text{CaO}$ system.....	73
Table 4.3 Reaction enthalpies at different hydration temperatures for $\text{Ca(OH)}_2/\text{CaO}$ system	74
Table 4.4 Gross heat input-output at different repeated cycles for $\text{Ca(OH)}_2/\text{CaO}$ system* ...	75
Table 4.5 Exergy available-output at different repeated cycles for $\text{Ca(OH)}_2/\text{CaO}$ system ....	76
Table 4.6 Operating conditions for the experiments.....	80
Table 4.7 Dehydration-hydration peak temperatures for different cycles .....	90
Table 5.1 Specifications of the reactor .....	96
Table 5.2. Technical features of the moving bed reactor.....	103
Table 5.3 Pilot-scale process parameters .....	111
Table 5.4 Total capital investment for ChHP pilot-scale system.....	112
Table 5.5 Utility data for different regions .....	120
Table 5.6 Parameters assumed for this study .....	121

## List of Figures

Figure 1.1 Example of Integrated Energy Systems .....	3
Figure 1.2 High-temperature industrial thermal processes with temperature requirements [7] 4	4
Figure 1.3 (a) Schematics of components of Ca(OH) <sub>2</sub> /CaO ChHP system; (b) Clausius- Clapeyron Diagram.....	5
Figure 2.1 Fugacity coefficient as a function of fugacity at different temperatures.....	21
Figure 2.2 Fugacity coefficient as a function of pressure at different temperatures.....	22
Figure 2.3 Reaction equilibrium for Ca(OH) <sub>2</sub> /CaO system in (a) P vs T.....	23
Figure 2.4 Reaction equilibrium for Ca(OH) <sub>2</sub> /CaO system in lnP vs 1/T.....	24
Figure 2.5 Comparison of different Clausius-Clapeyron equations for Ca(OH) <sub>2</sub> /CaO system .....	25
Figure 2.6 Comparison of different Clausius-Clapeyron equations for Ca(OH) <sub>2</sub> /CaO with reported experimental data points.....	26
Figure 2.7 Derived Clausius-Clapeyron Ca(OH) <sub>2</sub> /CaO equilibrium line and water equilibrium .....	29
Figure 3.1 Temperature program for thermal decomposition of Ca(OH) <sub>2</sub> .....	35
Figure 3.2 A schematic representation of pellet enhancement process .....	36
Figure 3.3 Percentage mass loss vs time at different maximum temperatures: a) 400°C; b) 425°C; c) 450°C; d) 475°C; e) 500°C.....	37
Figure 3.4 Conversion profile vs time at different isothermal temperature for decomposition of Ca(OH) <sub>2</sub> .....	39
Figure 3.5 Linear regression results for rate constant estimation for decomposition of Ca(OH) <sub>2</sub> at isothermal temperatures: a) 400°C; b) 425°C; c) 450°C; d) 475°C; e) 500°C ....	41
Figure 3.6 Linear regression curve between ln(k) vs 1/T for activation energy and Arrhenius constant estimation for decomposition of Ca(OH) <sub>2</sub> .....	42
Figure 3.7 Comparison of isothermal derived equation with experimental data.....	44
Figure 3.8 Comparison of non-isothermal derived equation with experimental data.....	45
Figure 3.9 Percentage mass loss vs time at different maximum temperatures for 1:0.5 Ca(OH) <sub>2</sub> :CaTiO <sub>3</sub> composite pellet: a) 400°C; b) 425°C; c) 450°C .....	46

Figure 3.10 Percentage mass loss vs time at different maximum temperatures for 1:1 Ca(OH) <sub>2</sub> :CaTiO <sub>3</sub> composite pellet: a) 400°C; b) 425°C; c) 450°C .....	47
Figure 3.11 Conversion of inert modified Ca(OH) <sub>2</sub> pellet at maximum temperature of 400°C .....	48
Figure 3.12 Conversion of inert modified Ca(OH) <sub>2</sub> pellet at maximum temperature of 425°C .....	49
Figure 3.13 Conversion of inert modified Ca(OH) <sub>2</sub> pellet at maximum temperature of 450°C .....	50
Figure 3.14 XRD diffraction patterns of composite pellet before and after decomposition...	51
Figure 3.15 Linear regression results for rate constant estimation at 400°C, 425°C and 450°C isothermal temperatures for decomposition of 1:0.5 Ca(OH) <sub>2</sub> :CaTiO <sub>3</sub> .....	52
Figure 3.16 Linear regression results for rate constant estimation at 400°C, 425°C and 450°C isothermal temperatures for decomposition of 1:1 Ca(OH) <sub>2</sub> :CaTiO <sub>3</sub> .....	52
Figure 3.17 Linear regression curve between ln(k) vs 1/T for activation energy and Arrhenius constant estimation for decomposition of 1:0.5 and 1:0.5 Ca(OH) <sub>2</sub> :CaTiO <sub>3</sub> .....	54
Figure 3.18 Pellet after the first decomposition of Ca(OH) <sub>2</sub> : (a) pure Ca(OH) <sub>2</sub> , (b) composite pellet.....	55
Figure 4.1 Netzsch TGA-DSC instrument.....	60
Figure 4.2 Schematic of the experimental setup .....	61
Figure 4.3 Lab scale experimental setup (left side: chemical reactor; right side: condenser/evaporator).....	61
Figure 4.4 The TGA percentage mass loss vs temperature curve of Ca(OH) <sub>2</sub> decomposition at different heating rates .....	67
Figure 4.5 The DSC heat vs temperature curve of Ca(OH) <sub>2</sub> decomposition at different heating rates .....	68
Figure 4.6 Chemical reactor center temperature and unreacted mole fraction vs time during dehydration reaction (Pressure ≈ 2.4 kPa) .....	70
Figure 4.7 Chemical reactor center temperature and mole fraction of Ca(OH) <sub>2</sub> vs time during the hydration reaction (Pressure ≈ 470 kPa).....	72
Figure 4.8 Energy storage/release process in a Ca(OH) <sub>2</sub> /CaO system under different decomposition temperatures .....	73

Figure 4.9 Gross heat energy after repeated dehydration-hydration process.....	76
Figure 4.10 Exergy after repeated dehydration-hydration process .....	77
Figure 4.11 Energy and exergy efficiencies after repeated dehydration-hydration process...	78
Figure 4.12 SEM images of fresh $\text{Ca}(\text{OH})_2$ pellet at magnification (i) 100 X (ii) 500 X (iii) 1000 X.....	79
Figure 4.13 SEM images after 1 <sup>st</sup> dehydration reaction at magnification (i) 100 X (ii) 500 X (iii) 1000 X.....	79
Figure 4.14 SEM images after 1 <sup>st</sup> hydration reaction at magnification (i) 100 X (ii) 500 X (iii) 1000 X.....	79
Figure 4.15 SEM images after 6 <sup>th</sup> dehydration reaction at magnification (i) 100 X (ii) 500 X (iii) 1000 X.....	79
Figure 4.16 SEM images after 6 <sup>th</sup> hydration reaction at magnification (i) 100 X (ii) 500 X (iii).....	80
Figure 4.17 Thermocouples position in chemical reactor.....	80
Figure 4.18 Temperature (outer) vs time plot during dehydration with pellet and powder....	82
Figure 4.19 Temperature (middle) vs time plot during dehydration with pellet and powder.	83
Figure 4.20 Temperature (center) vs time plot during dehydration with pellet and powder ..	83
Figure 4.21 Unreacted mole fraction of reactant during dehydration with pellets and powder .....	84
Figure 4.22 Temperature (outer) vs time plot during hydration with pellet and powder .....	85
Figure 4.23 Temperature (middle) vs time plot during hydration with pellet and powder ....	86
Figure 4.24 Temperature (center) vs time plot during hydration with pellet and powder .....	86
Figure 4.25 Mole fraction of $\text{Ca}(\text{OH})_2$ during hydration with pellets and powder.....	87
Figure 4.26 Powder condition after completing 2nd cycle .....	87
Figure 4.27 Temperature and mole fraction of $\text{Ca}(\text{OH})_2$ for 1 <sup>st</sup> repeated dehydration-hydration cycle.....	89
Figure 4.28 Temperature of $\text{Ca}(\text{OH})_2$ for 3 <sup>rd</sup> and 4 <sup>th</sup> continuous dehydration-hydration cycle .....	89
Figure 4.29 Mole fraction of $\text{Ca}(\text{OH})_2$ for 20 dehydration-hydration cycles .....	90
Figure 4.30 Pellet after the first decomposition of $\text{Ca}(\text{OH})_2$ : (a) pure $\text{Ca}(\text{OH})_2$ , (b) composite pellet and c) after 20 cycles .....	91

Figure 4.31 Compressive strength of composite pellet at different cycles .....	92
Figure 4.32 SEM images of composite pellets after 1 <sup>st</sup> cycle a) 50 X and b) 100 X.....	92
Figure 4.33 SEM images of composite pellets after 10 <sup>th</sup> cycle a) 50 X and b) 100 X .....	93
Figure 4.34 SEM images of composite pellets after 20 <sup>th</sup> cycle a) 50 X and b) 100 X .....	93
Figure 5.1 (a) Schematic of the cross-flow diagram of the pilot reactor; (b) Reactor filled with 20 kg of Ca(OH) <sub>2</sub> [1] .....	97
Figure 5.2 Process flow diagram of the test bench [1] .....	98
Figure 5.3 (a) Indirectly operated thermochemical storage reactor; (b) multifunctional test bench; (c) process flow diagram of the test bench with integrated indirectly operated reactor [2]......	99
Figure 5.4 Schematic of a thermochemical storage system with separation of power (heat exchanger/reactor) and capacity (silos) [3].....	100
Figure 5.5. Reactor design of a continuous MW-scale FBR for thermochemical energy storage [3] .....	100
Figure 5.6. (a) Heat exchanger design for moving particles and air; (b) complete reactor design [4] .....	101
Figure 5.7. Reactor design of a continuous MW-scale FBR for thermochemical energy storage [4] .....	102
Figure 5.8. Integration scheme of the pilot plant into existing thermochemical test bench at DLR (German Aerospace Center) [4].....	103
Figure 5.9. (a) Schematic representation of the flow of the HTF and storage material; (b) 3D image of the tube-bundle reactor [5].....	104
Figure 5.10. Schematics of the moving bed reactor integrated in the test bench [5]......	105
Figure 5.11 Schematics of the pilot-scale ChHP system with two chemical beds .....	108
Figure 5.12 Cross-section view of single tube inside .....	110
Figure 5.13 Overview of economic analysis methodology .....	113
Figure 5.14 Schematic of ChHP coupled with SMR system.....	115
Figure 5.15 Advanced SMR and SMR-ChHP combined scenarios .....	121
Figure 5.16 NPV values at different regions for SMR and different SMR-ChHP output scenarios.....	123
Figure 5.17 PBP at different regions for SMR and different SMR-ChHP output scenarios	124

Figure 5.18 Percentage deviation of PBP for different NHES scenarios from SMR values	125
Figure 5.19 DCFR at different regions for SMR and different SMR-ChHP output scenarios	126
Figure 5.20 Percentage deviation of DCFR for different NHES scenarios from SMR values	126
Figure 5.21 LCOE for SMR and different SMR-ChHP output scenarios	127
Figure 5.22 NPV and PBP versus overnight cost of advanced SMR for the California region	128
Figure 5.23 NPV and PBP versus overnight cost of advanced SMR for the Midwest region	129
Figure 5.24 NPV and PBP versus overnight cost of advanced SMR for the Northwest region	129
Figure 5.25 NPV and PBP versus overnight cost of advanced SMR for Southwest region.	130
Figure 5.26 NPV and PBP versus overnight cost of advanced SMR for the New England region	131
Figure 5.27 NPV and PBP versus overnight cost of advanced SMR for the PJM region	131
Figure 5.28 Percentage deviation in PBP based on increased carbon tax for the California region	132
Figure 5.29 Percentage deviation in PBP based on increased carbon tax for the Midwest region	133
Figure 5.30 Percentage deviation in PBP based on increased carbon tax for the Northwest region	133
Figure 5.31 Percentage deviation in PBP based on increased carbon tax for the Southwest region	134
Figure 5.32 Percentage deviation in PBP based on increased carbon tax for the New England region	134
Figure 5.33 Percentage deviation in PBP based on increased carbon tax for the PJM region	135

## Chapter 1 Introduction

The world faces a new challenge in the twenty-first century—substantially lowering greenhouse gas emissions while simultaneously providing energy access and economic opportunity to billions of people. During the 2021 United Nations Climate Change Conference of the Parties (COP26), 137 countries including China, United States and India, committed to net-zero, carbon neutrality or being climate-neutral. To have a major impact on greenhouse gas (GHG) emissions, non-electric energy sectors’ (industry, commercial, residential, and transportation) carbon footprint must be considered to achieve long-term emission reduction targets. Growth of the nuclear power sector can help realize the goal of a reliable, carbon emission free energy mix. While nuclear power is technologically mature and reliable, the economics of nuclear power have been challenged due to an influx of highly incentivized and intermittent renewable energy sources. High penetration of solar and wind energy into the power grid drops the value of electricity to low or even negative prices at certain times of day and year, reducing the nuclear power plant viability [1]. This significantly increases the payback period and financial risk of investment in nuclear power plants, despite their ability to provide reliable base-load power.

### 1.1 Nuclear Energy Current Status

According to the Nuclear Energy Institute [2], the United States avoided more than 476 million metric tons of carbon dioxide emissions in 2019, which is equivalent to removing 100 million cars from the road and more than all other clean energy sources combined. Contributing massive amounts of carbon-free power, nuclear energy produces more electricity on less land than any other clean-air source. A typical 1,000-megawatt nuclear facility in the United States needs a little more than 1 square mile to operate. Wind farms require 360 times more land area to produce the same amount of electricity and solar photovoltaic plants require 75 times more space.

Cost has been the primary issue facing the nuclear industry for over 20 years. When explaining the relatively limited expansion of nuclear power, the recent MIT Future of Nuclear report stated cost as the fundamental problem [3]. The nuclear power plant fleet in the United States was profitable during the most of the 2000s: their capital costs having been largely amortized over previous decades, and their operational costs were cheap compared with the

relatively high cost of fossil and renewable alternatives. Utilities embarked on a flurry of market-driven nuclear power plant purchases, power uprates, and license extensions as they attempted to maximize the value of their nuclear assets.

Current nuclear power reactors produce usable energy in the form of heat at modest temperatures (approximately 300°C); this heat is then converted to electricity using a steam turbine power cycle. In advanced nuclear reactors (so-called Generation-IV designs), the initial energy product is again heat, but planned to be delivered at much higher temperatures (500°C–800°C). These higher operating temperatures offer a potential opportunity for nuclear high-temperature reactor technology to provide useful process heat directly in industrial applications.

The International Atomic Energy Agency (IAEA) formally defines small modular reactors (SMRs) as nuclear reactors capable of producing less than 300 MW<sub>e</sub> of power [4]. Microreactors can supply anywhere from 1 to 20 MW<sub>e</sub>, thus producing less than 7% of the power output by SMRs, less than 0.7% of existing commercial reactors, and are transportable, and often self-adjusting. In the United States, very few utility companies have the required equity to finance the large upfront capital costs associated with reactors over 700 MW<sub>e</sub>. Therefore, many new SMR designs are being seriously considered and are in the design, research and development, or licensing stages.

## **1.2 Integrated Energy System**

Researchers have been attracted by Integrated Energy Systems (IES) in recent years due to their potential to reduce GHG emissions, increase energy efficiency, improve electrical grid dependability, and enhance energy economics as shown in Fig. 1.1. IES are collaboratively controlled systems that dynamically apportion thermal and/or electrical energy to promote the production of various energy products while also providing responsive generation to the power grid. Multiple subsystems make up an IES, which may or may not be geographically co-located [5–6]. To realize the benefits of IES with the current reactor fleets by providing process heat and improving economics, selection and development of a complimentary temperature upgrading technology is necessary. Multiple distinct energy sources operate behind a single grid link in this case. Thermal energy can be used to generate power, be stored, or be used in industrial thermal processes. In response to changing electric market conditions, this energy

distribution can be modified to maximize the value of the IES. Solar thermal and nuclear power are becoming less appealing to investors as the price of electricity fluctuates due to the arrival of renewable energy sources such as solar photovoltaic panels and wind turbines. Solar thermal and nuclear facilities do minimize greenhouse gas emissions, but they come with high upfront investments that are difficult to recover rapidly in a fluctuating energy market. While thermal storage is a component of the solution, there is also an opportunity to sell heat instead of power when it is more profitable. Several heat sources with zero GHG emissions can be employed for industrial heating.

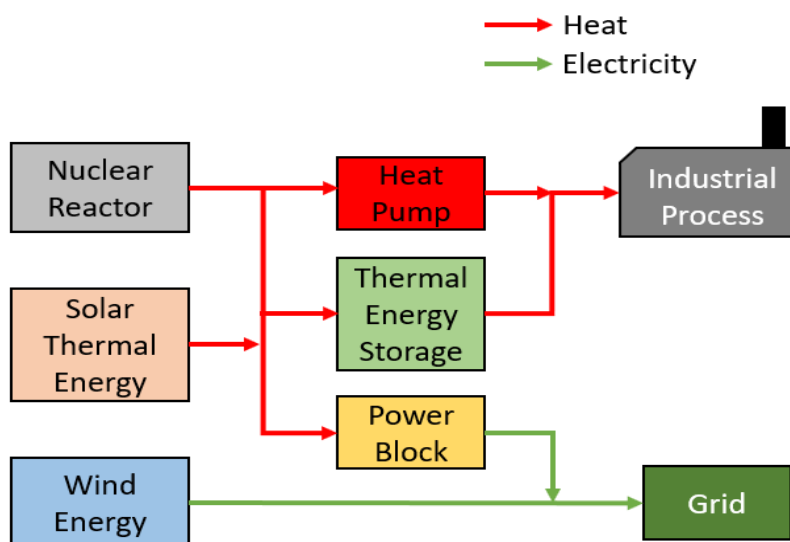


Figure 1.1 Example of Integrated Energy Systems

McMillan et al. gathered data on thermal energy consumption and CO<sub>2</sub> emissions for high-temperature thermal process businesses in the United States in 2016 [7]. They discovered that boilers or combined heat and power accounted for 70% of the 51 TBtu consumed in the U.S. industrial sector in 2014, while direct process heating accounted for another 24%. Because fossil fuels (mainly natural gas) are readily available, affordable, and simple to utilize, they are commonly used to generate the requisite high-temperature heat. Instead of fossil fuels, using nuclear or renewable thermal energy for these applications can significantly reduce GHG emissions. This also opens the possibility of using energy products other than electricity, which is not always feasible due to fluctuating electricity prices. The use of low-carbon energy sources could be improved by combining energy storage and better-integrated varied energy markets. Conventional nuclear reactors operate at 300–325°C, whereas the high-temperature

thermal industrial process typically requires heat at greater than 550°C, as shown in Fig. 1.2. To address the temperature mismatch, heat pumps are used between the nuclear power plant and the desired high-temperature thermal industries. Heat pump technologies are preferable to other alternatives (resistance heating) for achieving higher temperatures because they avoid the efficiency penalty associated with the thermal to electrical energy conversion while still enabling storage of thermal energy for later conversion to electricity if desired.

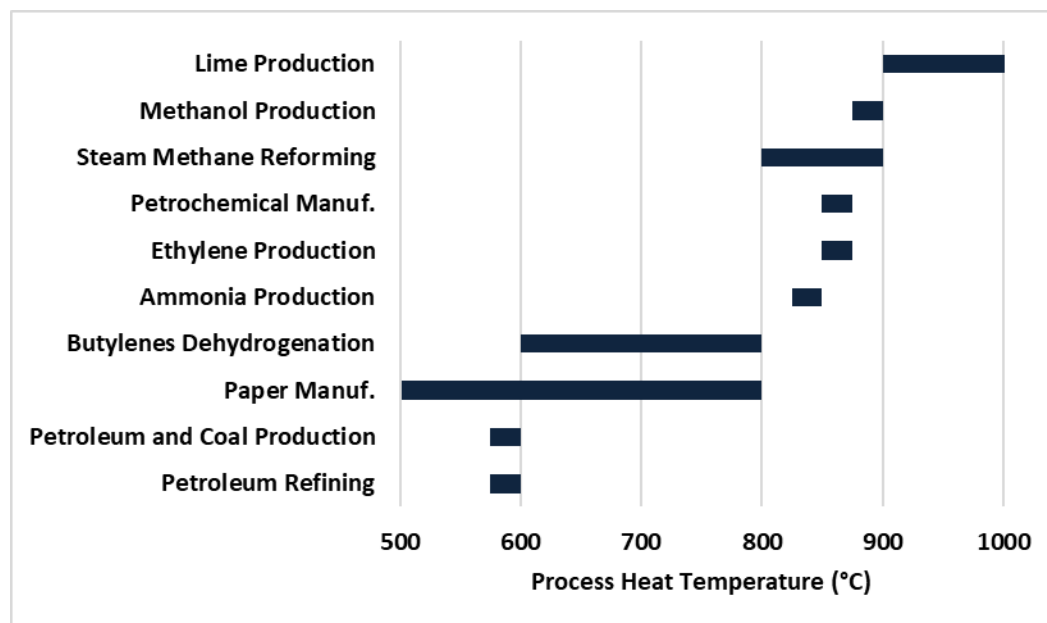


Figure 1.2 High-temperature industrial thermal processes with temperature requirements [7]

### 1.3 Chemical Heat Pump

Chemical Heat Pumps (ChHPs) utilize the reversible chemical reaction to change temperature levels of thermal energy (stored in chemical bonds of compounds) by manipulating reaction conditions. The advantages of ChHPs are their high-storage capacity, long-term storage of both reactant and product, lower heat loss, and energy upgrading for low-temperature heat [8]. Compared with mechanical and absorption heat pumps, ChHPs are capable of much higher temperature lifts with significantly less mechanical input [9]. A ChHP based on calcium hydroxide-oxide system is shown schematically in Figure 3. This system can also be operated as thermochemical energy storage system (TCES).

The attractiveness of  $\text{Ca(OH)}_2/\text{CaO}$  ChHP arises from the following points: (1) calcium hydroxide is relatively cheap and easily available, (2) the process has high storage density as

reaction enthalpy is high, and (3) there is a wide range of operating temperatures (300–650°C) for the system [8]. Other common systems include processes based on thermal decomposition of ammonium salts or metal hydrides; sulfur dioxide, carbon dioxide, or hydrogen systems; and adsorption on a solid sorbent. However, these systems are more costly, involve species that are toxic in nature (such as  $\text{NH}_3$  or  $\text{SO}_2$ , etc.), have issues related to reversibility, and the reagent handling is challenging, particularly when dealing with non-condensable gases.

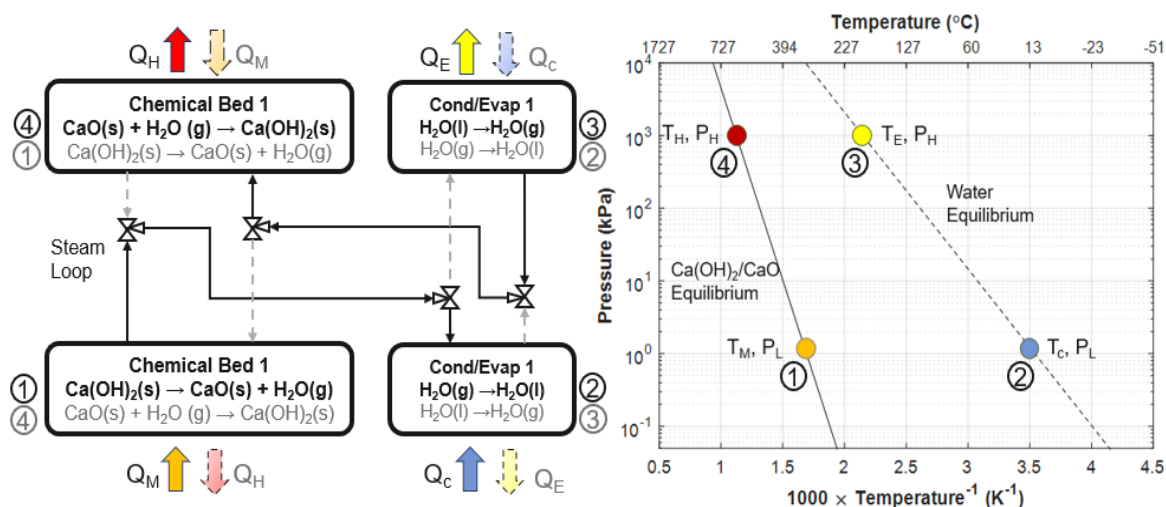


Figure 1.3 (a) Schematics of components of  $\text{Ca}(\text{OH})_2/\text{CaO}$  ChHP system; (b) Clausius-Clapeyron Diagram

The operation of this system can be described in two basic steps: charging and discharging, as shown in Fig 1.3. Charging starts with the addition of heat at  $T_M$  to dehydrate the chemical bed at low pressure. Then, the vapor is captured in a condenser and heat is rejected at  $T_C$ , usually the ambient temperature. For discharge, the vapor pressure is increased, and the water is evaporated with heat added at  $T_E$ . The vapor then hydrates the chemical bed, releasing the stored heat at  $T_H$ . Once the bed is done reacting, the bed can be charged again. The heat input and rejection temperatures of a chemical heat pump are mainly dictated by the saturation or equilibrium temperatures of the refrigerant or reactants used. In a survey conducted in 2013 by Sabharwall et al., the reversible  $\text{Ca}(\text{OH})_2/\text{CaO}$  reaction shown in Equation 1.1 was established as the best candidate for high-temperature boosting of heat from light-water reactors to high-temperature industrial thermal processes [10].



The  $\text{Ca(OH)}_2/\text{CaO}$  reaction has a high-energy density, fast-reaction kinetics, and an equilibrium curve appropriate for the high temperatures involved with the industries of interest. A schematic of the  $\text{Ca(OH)}_2/\text{CaO}$  ChHP is shown in Fig 1.3a. The Clausius-Clapeyron diagram in Fig. 1.3b shows the equilibrium curve for the reaction and the saturation curve of water. The calcium oxide hydration reaction has the potential to receive heat at  $350^\circ\text{C}$  during charging and deliver heat above  $600^\circ\text{C}$  during discharge. This means the reaction is not only helpful in delivering heat at high temperatures, but also temperature lifts greater than  $250^\circ\text{C}$ . High-temperature operation and large temperature lifts make the  $\text{CaO}/\text{Ca(OH)}_2$  chemical heat pump a great candidate for efficient high-temperature process heating using low-carbon thermal energy.

Several researchers have investigated the  $\text{Ca(OH)}_2/\text{CaO}$  reversible system both theoretically and experimentally. Schaube [11] and Matsuda [12] used thermogravimetric analysis with 10–30 mg of  $\text{Ca(OH)}_2$  for investigation of dehydration-hydration reversible reaction of  $\text{Ca(OH)}_2/\text{CaO}$ . Dai et al. [13] conducted dehydration and hydration on a small scale with powdered 20 g of  $\text{Ca(OH)}_2$ , and the gross heat input and outflow were calculated under standard conditions. Schmidt et al. [14] used a significantly bigger system containing 2.4-kg  $\text{Ca(OH)}_2$  at a low pressure to test heat transfer fluids under varied heating and cooling loads. Schmidt et al. [15] designed chemical reactor indirectly operated by integrating heat exchanger at high temperature for 20-kg  $\text{Ca(OH)}_2$  and Criado et al. [16] examined the reaction behavior in a fluidized bed system. Schaube et al. [17] studied the direct heat transfer output of  $\text{CaO}/\text{Ca(OH)}_2$  in a fixed bed reactor containing 60-g powdered  $\text{Ca(OH)}_2$ . Funayama et al. [18] used 60 g of calcium hydroxide pellets to enhance the temperature of the  $\text{Ca(OH)}_2/\text{CaO}$  dehydration-hydration cycle, and the heat storage density of the bed was calculated assuming constant reaction enthalpy. Most of the above studies focused on the thermochemical energy storage aspect of  $\text{Ca(OH)}_2/\text{CaO}$  reaction system.

Modifying the reactant to improve its mechanical and physical properties has been the topic of a few recent investigations as studies have found an agglomeration of reactant giving rise to low effective thermal conductivity and poor heat and mass transfer. Criado et al. [19] studied the crushing strength and mechanical stability of a  $\text{CaO}$ -based material with  $\text{Na}_2\text{Si}_3\text{O}_7$  as a modifier and discovered that decreasing the reaction time was a viable alternative for

increasing the reactants' mechanical stability. For incomplete conversion of CaO to Ca(OH)<sub>2</sub>, the crushing strength of CaO-based material particles was increased, but higher conversion resulted in a lower crushing strength. Yan et al. [20] looked at modifying a CaO-based material with LiOH to improve dehydration performance, but the modification had no effect on the solid reactant's structural integrity. Sakellarios et al. [21] added aluminum to CaO in the form of aluminum oxide, which improved structural stability while reduced the material's hydration activity. Adding a minimal amount of nano-SiO<sub>2</sub> to CaO particles prevented agglomeration and stabilized the bulk characteristics of CaO particles, but had little effect on lowering the dehydration temperature, according to Roßkopf et al. [22, 23].

#### **1.4 SMR and ChHP Economics**

The development of an SMR involves significantly less upfront money, resulting in lower financial risks and making it a viable alternative to large nuclear reactors (1 GW). SMR can also combine with a hybrid energy system to manage fluctuations in intermittent renewable energy generation while also storing energy or providing electricity/heat. Bolden et al. [24, 25] examined the SMR economics through a comprehensive model based on first-of-a-kind (FOAK) through nth-of-a-kind (NOAK). The model evaluates a project's feasibility in regards of market conditions and commonly used capital budgeting techniques like the net present value (NPV), internal rate of return (IRR), payback period (PBP), and the levelized cost of energy (LCOE). Sabharwall et al. [26] conducted a study on nuclear-renewable energy integration economics where study compares economic of three cases, i.e., nuclear, nuclear-wind and nuclear-wind-hydrogen for the PJM and Mid-C U.S. markets. Alonso et al. [27] conducted economic comparative study on SMR versus coal and combined cycle plants. They performed sensitivity analysis showing how NPV and IRR vary with changing discount rates and overnight capital cost. Within IES, there is an obvious requirement to resolve temperature mismatches between energy sources and demands in the most effective way feasible. The techno-economics model is critical for determining whether technical and market factors make the heat pump advantageous and appealing to investors.

Very few studies have focused on the economic feasibility of ChHPs because of low technology readiness level of the system. Spoelstra et al. [28] studied the techno-economic analysis of two different ChHPs for temperature amplification less than 150°C. The

isopropanol-acetone and ammonia-salt systems were proposed. The ammonia-salt vapor heat pump outperforms the isopropanol-acetone heat pump in terms of technical performance by evaluating internal rate of return of 7%, as it has a higher enthalpic efficiency, a higher coefficient of performance, and does not produce by-products. Karaca et al. [29] investigated economics of ChHP based on ethanol–formaldehyde–hydrogen, ethanol–acetaldehyde–hydrogen, iso-propanol–acetone–hydrogen and n-butanol–butyraldehyde–hydrogen systems for low-temperature heat upgrade from 77–200°C. These studies were conducted in 2002, and the economy and policy have changed significantly since then. Bayon et al. [30] explored the techno-economic feasibility of thermochemical energy storage systems when coupled with solar thermal energy. The working pair investigated were molten salts, alkaline-hydroxides, carbonates, and oxides. Of 17 working pairs analyzed, eight showed high potential for commercial applications with a cost lower than \$25 MJ<sup>-1</sup> including Ca(OH)<sub>2</sub>/CaO system. There have not been any techno-economic studies reported which focuses on ChHP for thermo-amplification to boost the temperature from 350°C to 600°C and above.

The objective of the research was to develop and demonstrate the technical feasibility of the Ca(OH)<sub>2</sub>/CaO ChHP system for temperature amplification in a bench scale system. The specific objectives included thermodynamic modeling, cyclability and reproducibility, kinetic study, and techno-economic analysis (TEA). In chapter 2, a modified Clausius-Clapeyron equation that incorporates the temperature dependence of thermodynamic quantities was developed to describe the equilibrium for the reversible calcium hydroxide decomposition/calcium oxide hydration reaction couple. Equilibrium relationships of greater accuracy are highly desired, as they have significant impact on the design and operation of the ChHP. In chapter 3, kinetic parameters were estimated based on the thermo-gravimetric analyzer (TGA) results at different isothermal temperatures. A rate equation was developed for the decomposition reaction. The effect of adding of CaTiO<sub>3</sub> to pure Ca(OH)<sub>2</sub> in the form of a composite pellet 1:0.5 and 1:1 Ca(OH)<sub>2</sub>:CaTiO<sub>3</sub> (by wt. %) on kinetic parameters was also studied. In chapter 4, study on cyclability of Ca(OH)<sub>2</sub>-CaO and inert modified composite pellets were reported. In chapter 5, a TEA was conducted for an advanced SMR and an SMR coupled with different thermal output ChHP systems to determine the profitability of selling heat rather than only electricity.

## References

1. C. Forsberg, S. Brick, and G. Haratyk. 2018. "Coupling heat storage to nuclear reactors for variable electricity output with baseload reactor operation," *The Electricity Journal* 31: 23–31. <https://doi.org/10.1016/j.tej.2018.03.008>.
2. NEI, "Cost Competitiveness of Micro-Reactors for Remote Markets" Nuclear Energy Institute. April 15, 2019. <https://www.nei.org/resources/reports-briefs/cost-competitiveness-micro-reactors-remote-markets> (accessed November 21, 2021).
3. J. Buongiorno, M. Corradini, J. Parsons, D. Petti. 2018. "The Future of Nuclear Energy in a Carbon-Constrained World," MIT, IEEE, vol. 275.
4. IAEA. 2020. "Advances in Small Modular Reactor Technology Developments A Supplement to: IAEA Advanced Reactors Information System (ARIS) 2020 Edition," *International Atomic Energy Agency (IAEA)*.
5. S. M. Bragg-Sitton, R. Boardman, C. Rabiti, and J. O'Brien. 2020. "Reimagining future energy systems: Overview of the US program to maximize energy utilization via integrated nuclear-renewable energy systems," *International Journal of Energy Research* 44:8156–8169. <https://doi.org/10.1002/er.5207>.
6. S. M. Bragg-Sitton, R. Boardman, C. Rabiti, J. Suk Kim, M. McKellar, P. Sabharwall, J. Chen, M. S. Cetiner, T. J. Harrison, and A. L. Qualls. 2016. "Nuclear-Renewable Hybrid Energy Systems: 2016 Technology Development Program Plan," INL/EXT-16-38165, Idaho National Laboratory, Idaho Falls, Idaho (United States); Oak Ridge National Laboratory, Oak Ridge, Tennessee (United States). <https://doi.org/10.2172/1333006>.
7. C. McMillan and M. Ruth. 2016. "Generation and Use of Thermal Energy in the U.S. Industrial Sector and Opportunities to Reduce its Carbon Emissions," INL/EXT-16-39680, Idaho National Laboratory. <https://doi.org/10.2172/1334495>.
8. W. Wongsuwan, S. Kumar, P. Neveu, and F. Meunier. 2021. "A review of chemical heat pump technology and applications." *Applied Thermal Engineering* 21:1489–1519. [https://doi.org/10.1016/S1359-4311\(01\)00022-9](https://doi.org/10.1016/S1359-4311(01)00022-9).

9. M. Arjmand, L. Liu, and I. Neretnieks. 2013. "Exergetic efficiency of high-temperature-lift chemical heat pump (CHP) based on CaO/CO<sub>2</sub> and CaO/H<sub>2</sub>O working pairs." *International Journal of Energy Research* 37:1122–1131. <https://doi.org/10.1002/er.2918>.
10. P. Sabharwall, D. Wendt, and V. P. Utgikar. 2013. "Application of Chemical Heat Pumps for Temperature Amplification in Nuclear Hybrid Energy Systems for Synthetic Transportation Fuel Production," INL/EXT-13-30463, Idaho National Laboratory. <https://doi:10.2172/1104502>.
11. F. Schaube, L. Koch, A. Wörner, and H. Müller-Steinhagen. 2012. "A thermodynamic and kinetic study of the de- and rehydration of Ca(OH)<sub>2</sub> at high H<sub>2</sub>O partial pressures for thermo-chemical heat storage," *Thermochimica Acta*. 538:9–20. <https://doi.org/10.1016/j.tca.2012.03.003>.
12. H. Matsuda, T. Ishizu, S. K. Lee, and M. Hasatani. 1985. "Kinetic study of Ca(OH)<sub>2</sub>/CaO reversible thermochemical reaction for thermal energy storage by means of chemical reaction," *Kagaku Kogaku Ronbunshu* 11:542–548. <https://doi.org/10.1252/kakoronbunshu.11.542>.
13. L. Dai, X. -F. Long, B. Lou, and J. Wu. 2018. "Thermal cycling stability of thermochemical energy storage system Ca(OH)<sub>2</sub>/CaO," *Applied Thermal Engineering* 133:261–268. <https://doi.org/10.1016/j.applthermaleng.2018.01.059>.
14. M. Schmidt, A. Gutierrez, and M. Linder. 2017. "Thermochemical energy storage with CaO/Ca(OH)<sub>2</sub> – Experimental investigation of the thermal capability at low vapor pressures in a lab scale reactor," *Applied Energy* 188:672–681. <https://doi.org/10.1016/j.apenergy.2016.11.023>.
15. M. Schmidt, C. Szczukowski, C. Roßkopf, M. Linder, and A. Wörner. 2014. "Experimental results of a 10 kW high temperature thermochemical storage reactor based on calcium hydroxide," *Applied Thermal Engineering* 62:553–559. <https://doi.org/10.1016/j.applthermaleng.2013.09.020>.
16. Y. A. Criado, M. Alonso, J. C. Abanades, and Z. Anxionnaz-Minvielle. 2014. "Conceptual process design of a CaO/Ca(OH)<sub>2</sub> thermochemical energy storage system using fluidized

- bed reactors," *Applied Thermal Engineering* 73:1087–1094. <https://doi.org/10.1016/j.applthermaleng.2014.08.065>.
17. F. Schaube, A. Kohzer, J. Schütz, A. Wörner, and H. Müller-Steinhagen. 2013. "De- and rehydration of  $\text{Ca}(\text{OH})_2$  in a reactor with direct heat transfer for thermo-chemical heat storage. Part A: Experimental results," *Chemical Engineering Research and Design* 91:856–864. <https://doi.org/10.1016/j.cherd.2012.09.020>.
18. S. Funayama, H. Takasu, M. Zamengo, J. Kariya, S. T. Kim, and Y. Kato. 2019. "Composite material for high-temperature thermochemical energy storage using calcium hydroxide and ceramic foam," *Energy Storage* 1:e53. <https://doi.org/10.1002/est2.53>.
19. Y. A. Criado, M. Alonso, and J. C. Abanades. 2016. "Enhancement of a  $\text{CaO}/\text{Ca}(\text{OH})_2$  based material for thermochemical energy storage," *Solar Energy* 135:800–809. <https://doi.org/10.1016/j.solener.2016.06.056>.
20. J. Yan and C. Y. Zhao. 2014. "First-principle study of  $\text{CaO}/\text{Ca}(\text{OH})_2$  thermochemical energy storage system by Li or Mg cation doping," *Chemical Engineering Science* 117:293–300. <https://doi.org/10.1016/j.ces.2014.07.007>.
21. K. G. Sakellariou, G. Karagiannakis, Y. A. Criado, and A. G. Konstandopoulos. 2015. "Calcium oxide based materials for thermochemical heat storage in concentrated solar power plants," *Solar Energy* 122:215–230. <https://doi.org/10.1016/j.solener.2015.08.011>.
22. C. Roßkopf, M. Haas, A. Faik, M. Linder, and A. Wörner. 2014. "Improving powder bed properties for thermochemical storage by adding nanoparticles," *Energy Conversion and Management* 86:93–98. <https://doi.org/10.1016/j.enconman.2014.05.017>.
23. C. Roßkopf, S. Afflerbach, M. Schmidt, B. Görtz, T. Kowald, M. Linder, and R. Trettin. 2015. "Investigations of nano coated calcium hydroxide cycled in a thermochemical heat storage," *Energy Conversion and Management* 97:94–102. <https://doi.org/10.1016/j.enconman.2015.03.034>.
24. L. Boldon. 2015. "Sustainability Efficiency Factor: Measuring Sustainability in Advanced Energy Systems through Exergy, Exergoeconomic, Life Cycle, and Economic Analyses," PhD Thesis, Rensselaer Polytechnic Institute. <https://ui.adsabs.harvard.edu/abs/2015PhDT.....258B> (accessed March 1, 2022).

25. L. M. Boldon and P. Sabharwall. 2014. "Small modular reactor: First-of-a-Kind (FOAK) and Nth-of-a-Kind (NOAK) Economic Analysis," INL/EXT-14-32616, Idaho National Laboratory. <https://doi.org/10.2172/1167545>.
26. P. Sabharwall, S. Bragg-Sitton, L. Boldon, and S. Blumsack. 2015. "Nuclear Renewable Energy Integration: An Economic Case Study," *The Electricity Journal* 28:85–95. <https://doi.org/10.1016/j.tej.2015.09.003>.
27. G. Alonso, S. Bilbao, and E. del Valle. 2016. "Economic competitiveness of small modular reactors versus coal and combined cycle plants," *Energy* 116:867–879. <https://doi.org/10.1016/j.energy.2016.10.030>.
28. S. Spoelstra, W. G. Haije, and J. W. Dijkstra. 2002. "Techno-economic feasibility of high-temperature high-lift chemical heat pumps for upgrading industrial waste heat," *Applied Thermal Engineering* 22:1619–1630. [https://doi.org/10.1016/S1359-4311\(02\)00077-7](https://doi.org/10.1016/S1359-4311(02)00077-7).
29. F. Karaca, O. Kıncay, and E. Bolat. 2002. "Economic analysis and comparison of chemical heat pump systems," *Applied Thermal Engineering* 22:1789–1799. [https://doi.org/10.1016/S1359-4311\(02\)00078-9](https://doi.org/10.1016/S1359-4311(02)00078-9).
30. A. Bayon, R. Bader, M. Jafarian, L. Fedunik-Hofman, Y. Sun, J. Hinkley, S. Miller, and W. Lipiński. 2018. "Techno-economic assessment of solid–gas thermochemical energy storage systems for solar thermal power applications," *Energy* 149:473–484. <https://doi.org/10.1016/j.energy.2017.11.084>.

## Chapter 2 Thermodynamic Modeling of Ca(OH)<sub>2</sub>/CaO Reversible Reaction System

### 2.1 Objective

The direction of the chemical transformation in a reversible reaction couple can be altered by manipulating the operating conditions, which creates a driving force for the transformation due to the deviation from thermodynamic equilibrium. Quantifying the magnitude of the driving force and identifying the direction of the transformation accurately requires an accurate description of thermodynamic equilibrium of the system. The thermodynamic equilibrium for the reversible reaction system is usually described by the Clausius-Clapeyron equation shown below in Eq. 2.1;  $P_{eq}$ , is the equilibrium pressure of the system, i.e., that of water vapor, at the system temperature  $T_{eq}$  and  $\zeta$  is the constant of integration.

$$\ln P_{eq} = -\frac{\Delta H}{RT_{eq}} + \zeta \quad (2.1)$$

As indicated by the equation, the equilibrium system pressure is determined by the reaction temperature. Conversely, manipulating the system pressure allows one to control the temperature, and manipulation of these variables allows one to control the direction of the reaction. Three of the most commonly used forms of the Clausius-Clapeyron equation for this chemical system reported in literature are shown in Table 2.1.

Table 2.1 Reported Clausius-Clapeyron equilibrium relation for Ca(OH)<sub>2</sub>/CaO system

Equation	References
$\ln\left(\frac{P_{eq}[Pa]}{10^5}\right) = -\frac{11375}{T[K]} + 14.574$	Samms and Evans [1]
$\ln\left(\frac{P_{eq}[Pa]}{10^5}\right) = -\frac{12845}{T[K]} + 16.508$	Schaube et. al. [2]

$$\ln\left(\frac{P_{eq}[\text{Pa}]}{10^5}\right) = -\frac{11607}{T[\text{K}]} + 14.648$$

Criado et al. [3]  
Barin and Platzki [4]

---

\*The values 11375, 12845 and 11607 in the above equilibrium relations are  $\Delta H/R$  and the unit is (K)

The equations listed above in Table 2.1 assumed a constant reaction enthalpy ( $\Delta H_r$ ) over the temperature range. However, rigorous application of thermodynamics requires consideration of its dependence on temperature and pressure. *In this chapter, we present a refinement of the thermodynamic equilibrium by incorporating the temperature dependence of the reaction enthalpy in the equation.* Further, we also present an analysis of the effect of non-ideality in the vapor phase for additional refinement and identification of conditions when the effect may be significant. These refinements will help improve the accuracy of the equilibrium relationships governing the process, increasing the understanding of the process, and ultimately leading to better process design.

## 2.2 Thermodynamic Analysis

Thermodynamic relationships describe the limiting conditions of the state of any system, and in case of a chemical reaction, the technical constraint on the conversion that can be achieved for that system. Temperature dependence on thermodynamic state functions enthalpy, entropy and Gibbs energy changes are described in section 2.2.1, and an analysis of the non-ideality in the vapor phase is presented in section 2.2.2.

### 2.2.1 Temperature dependence of thermodynamic properties

The enthalpy change for the  $\text{Ca}(\text{OH})_2/\text{CaO}$  decomposition reaction ( $\Delta H_r$ ) can be calculated at any given temperature from Eq. 2.2:

$$\Delta H_r = \sum_i^{n_p} \nu_i H_i - \sum_i^{n_r} \nu_i H_i$$

(2.2)

where  $H_i$  and  $v_i$  represent the molar enthalpy and the stoichiometric coefficient of the species  $i$ , respectively. The summation of enthalpies is carried over the total number of products and reactants,  $n_p$  and  $n_r$  respectively. The molar enthalpy of species  $i$  can be represented by a polynomial function of the temperature as shown by Eq. 2.3 [5].

$$H_i = H_{i,298.15}^0 + c_{i,1}t + \frac{c_{i,2}t^2}{2} + \frac{c_{i,3}t^3}{3} + \frac{c_{i,4}t^4}{4} - \frac{c_{i,5}}{t} + c_{i,6} - c_{i,8} \quad (2.3)$$

where  $t$  is related to the absolute temperature  $T$  by the equation  $t = T/1000$ . The values of constants in Eq. 4 for the three species involved in the reaction are shown in Table 2.2. The resulting enthalpy  $\Delta H_r$  has the units of kJ/mol.

Table 2.2 Values of Parameters in Eq. 2.3

i	Ca(OH) <sub>2</sub>	CaO	H <sub>2</sub> O
$c_{i,1}$	130.8253	49.95403	30.092
$c_{i,2}$	-82.69216	4.887916	6.832514
$c_{i,3}$	122.7690	-0.352056	6.793435
$c_{i,4}$	-50.39210	0.046187	-2.534480
$c_{i,5}$	-2.513146	-0.825097	0.082139
$c_{i,6}$	-1030.841	-652.9718	-250.8810
$c_{i,7}$	247.1857	92.56096	223.3967
$c_{i,8}$	-986.0851	-635.0894	-241.8264

The resulting reaction enthalpy as a function of  $t$  is shown in Eq. 2.4.

$$\Delta H_r = \Delta H_{r,298.15}^0 + c_{r,1}t + \frac{c_{r,2}t^2}{2} + \frac{c_{r,3}t^3}{3} + \frac{c_{r,4}t^4}{4} - \frac{c_{r,5}}{t} + c_{r,6} - c_{r,8} \quad (2.4)$$

where, the constants  $c_{r,j}$  are obtained by Eq. 2.5 in which  $j$  ranges from 1-8 and shown in Table 2.3.

$$c_{r,j} = \sum_i^{n_p} v_i c_{i,j} - \sum_i^{n_r} v_i c_{i,j} \quad (2.5)$$

Table 2.3 Parametric Values of constants in Eq. 2.4

$c_{r,1}$	$c_{r,2}$	$c_{r,3}$	$c_{r,4}$	$c_{r,5}$	$c_{r,6}$	$c_{r,7}$	$c_{r,8}$
-50.77927	94.41259	-116.32762	47.903807	1.770188	126.9882	68.7719	109.1693

The entropy change for the reaction is calculated in the same manner as the enthalpy change and the resulting  $\Delta S_r$  has the unit of J/mol K:

$$\Delta S_r = \sum_i^{n_p} \nu_i S_i - \sum_i^{n_r} \nu_i S_i \quad (2.6)$$

Where entropy of the species is given by:

$$S_i = c_{i,1} \ln(t) + c_{i,2} t + \frac{c_{i,3} t^2}{2} + \frac{c_{i,4} t^3}{3} - \frac{c_{i,5}}{2t^2} + c_{i,7} \quad (2.7)$$

The resulting reaction entropy as a function of t is shown in Eq. 2.8.

$$\Delta S_r = c_{r,1} \ln(t) + c_{r,2} t + \frac{c_{r,3} t^2}{2} + \frac{c_{r,4} t^3}{3} - \frac{c_{r,5}}{2t^2} + c_{r,7} \quad (2.8)$$

The enthalpy and entropy changes for the reaction can be used to calculate the Gibbs energy change for it, which in turn, allows the determination of the equilibrium constant for the reaction at the reaction temperature as shown in Eq. 2.9. The relationship between the equilibrium constant and Gibbs free energy is given by Eq. 2.10 or its rearranged form, Eq. 2.11.

$$\Delta G = \Delta H - T\Delta S \quad (2.9)$$

$$\Delta G = -RT \ln K_{eq} \quad (2.10)$$

$$K_{eq} = e^{\left(\frac{-\Delta G}{RT}\right)} \quad (2.11)$$

The equilibrium constant for the reaction is expressed in terms of activities ( $a$ ) of the species involved in it:

$$K_{eq} = \frac{a_{H_2O} \cdot a_{CaO}}{a_{Ca(OH)_2}} \quad (2.12)$$

Activity of substances (solid or liquid) can be assumed as unity and activity for a gas is simply fugacity divided by reference fugacity. Fugacity is a measure of the tendency of a gas to escape or expand. The fugacity of a real gas is an effective partial pressure which replaces the mechanical partial pressure in an accurate determination of the chemical equilibrium. Thus, the  $K_{eq}$  can be further simplified to:

$$K_{eq} = a_{H_2O} = \frac{f}{\bar{f}} \quad (2.13)$$

We can conclude that  $K_{eq}$  is numerically equal to fugacity of water vapor, where  $f$  is the fugacity and  $\bar{f}$  is the reference fugacity at 1 bar.

$$K_{eq} = f \quad (2.14)$$

From Eq. 2.10 and 2.14, a relationship between fugacity and Gibbs free energy is obtained as shown in Eq. 2.15. Temperature dependence of the fugacity is obtained by differentiating Eq. 2.15 with temperature resulting in Eq. 2.17, which is similar to the traditional Clapeyron equation.

$$\ln(f) = \frac{-\Delta G}{RT} \quad (2.15)$$

$$\frac{d(\ln f)}{dT} = \frac{d}{dT} \left( \frac{-\Delta G}{RT} \right) \quad (2.16)$$

$$\frac{d(\ln f)}{dT} = \frac{\Delta H}{RT^2} \quad (2.17)$$

Integration of Eq. 2.17 yields a relationship between the fugacity and temperature.

*Case 1:* Assuming  $\Delta H$  to be constant (independent of temperature)

If the enthalpy change is assumed to be independent of temperature, an equation similar to the Clausius-Clapeyron equation is obtained as shown by Eq. 2.17, where  $\zeta_1$  is a constant, and  $f$  is in the units of bar.

$$\ln f = \frac{-\Delta H}{RT} + \zeta_1 \quad (2.18)$$

*Case 2: Incorporating effect of temperature on  $\Delta H$*

However, as discussed above,  $\Delta H_r$  is a function of temperature as derived in Eq. 2.4. The resulting differential and integrated forms of Eq. 2.18 incorporating this dependence are shown in Eq. 2.19 and 2.20, respectively,  $\zeta_2$  being the constant of integration.

$$\frac{d(\ln f)}{dT} = \frac{\left( \Delta H_{r,298.15}^0 + \frac{c_{r,1}T}{1000} + \frac{c_{r,2}T^2}{2 \cdot 10^6} + \frac{c_{r,3}T^3}{3 \cdot 10^9} + \frac{c_{r,4}T^4}{4 \cdot 10^{12}} - \frac{c_{r,5} \cdot 1000}{T} + c_{r,6} - c_{r,8} \right)}{RT^2} \quad (2.19)$$

$$\ln f = \frac{\left( -\Delta H_{r,298.15}^0 + \frac{c_{r,1}T \ln(T)}{1000} + \frac{c_{r,2}T^2}{2 \cdot 10^6} + \frac{c_{r,3}T^3}{6 \cdot 10^9} + \frac{c_{r,4}T^4}{12 \cdot 10^{12}} + \frac{1000 \cdot c_{r,5}}{2T} - c_{r,6} + c_{r,8} \right)}{RT} + \zeta_2 \quad (2.20)$$

### 2.2.2 Non-ideality in vapor phase

Obtaining equilibrium conditions requires determination of the fugacity as can be seen from the above discussion [6]. The fugacity of an ideal gas is equal to its pressure; however, real gases exhibit non-ideality in their behavior. For these substances, fugacity needs to be determined experimentally or estimated from an accurate equation of state (EOS) that describes their volumetric behavior.

The pressure and fugacity of a real gas are related through the dimensionless fugacity coefficient ( $\phi$ ) as shown by Eq. 2.21.

$$f_{H_2O} = \phi_{H_2O} \cdot P_{H_2O} \quad (2.21)$$

The fugacity coefficient of the water vapor is estimated by using the Soave-Redlich-Kwong (SRK) EOS which is given by Eq. 2.22 [6-7].

$$P = \frac{RT}{(V-b)} - \frac{a_{SRK}}{V(V+b)} \quad (2.22)$$

The resulting equation for the fugacity coefficient is shown in Eq. 2.23. The compressibility factor ( $Z$ ) and the parameter  $B$  required in this calculation are obtained using the relationships given by Eqs. 2.24 and 2.25, respectively [6-7].

$$\ln\phi = Z - 1 - \ln(Z - B) - \frac{a_{SRK}}{bRT} \ln\left(\frac{Z+B}{Z}\right) \quad (2.23)$$

$$Z = \frac{P*V}{R*T} \quad (2.24)$$

$$B = \frac{P*b}{R*T} \quad (2.25)$$

Molar volume ( $V$ ) at any given pressure ( $P$ ) and temperature ( $T$ ) required for calculating the compressibility factor is obtained by solving the SRK equation which is a cubic equation in  $V$  in its rearranged form as shown below in Eq. 2.26.

$$V^3 - \frac{RT}{P}V^2 - \left(b^2 + \frac{RT}{P} - \frac{a_{SRK}}{P}\right)V - \frac{a_{SRK}b}{P} = 0 \quad (2.26)$$

The molecular co-volume ( $b$ ) is calculated from critical temperature ( $T_c$ ) and pressure ( $P_c$ ) using Eq. 2.27.

$$b = \frac{0.08664*R*T_c}{P_c} \quad (2.27)$$

The energy parameter ( $a_{SRK}$ ) depends on critical temperature ( $T_c$ ), critical pressure ( $P_c$ ), reduced temperature ( $T_r$ ), and the acentric factor ( $\omega$ ), and is calculated using Eqs. 2.28-2.31.

$$a_{SRK} = \frac{0.42748*R^2*T_c^2*M}{P_c} \quad (2.28)$$

$$M = (1 + N * (1 - \sqrt{T_r}))^2 \quad (2.29)$$

$$N = 0.48 + 1.574 * \omega - 0.176 * \omega^2 \quad (2.30)$$

$$T_r = \frac{T}{T_c} \quad (2.31)$$

### 2.3 Results and Discussions

The values of the enthalpy change, entropy change, and the Gibbs energy change for the decomposition of  $\text{Ca(OH)}_2$ , calculated using Eqs. 2.4, 2.8 and 2.9 were found to be 106.28 kJ/mol, 136.16 J/mol K and 41.851 kJ/mol, respectively, at 473.15 K. The equilibrium constant

$K_{eq}$  is calculated using Eq. 2.11 and is  $\sim 2.392 \times 10^{-5}$ . From Eq. 2.12, we know that  $K_{eq}$  is equal to fugacity of water vapor so,  $f = 2.392 \times 10^{-5}$  bar.

### 2.3.1 Non-ideality in vapor phase

The constant of integration in Eq. 2.19, where the enthalpy change ( $\Delta H = 106.28$  kJ/mol) is assumed to be constant, was found to be 16.377, yielding an equation similar to the Clausius-Clapeyron equation where fugacity is in bar and temperature in kelvin:

$$\ln f = \frac{-106280}{RT} + 16.377 \quad (2.32)$$

When the temperature dependence of the enthalpy change is taken into account, the resulting equation is more complicated as shown below.

$$\ln f = \frac{\left( -109170 + \frac{c_{r,1}T \ln(T)}{1000} + \frac{c_{r,2}T^2}{2 \cdot 10^6} + \frac{c_{r,3}T^3}{6 \cdot 10^9} + \frac{c_{r,4}T^4}{12 \cdot 10^{12}} + \frac{1000 \cdot c_{r,5}}{2T} - c_{r,6} + c_{r,8} \right)}{RT} + 17.14 \quad (2.33)$$

It should be noted that the constants of integration in Eqs. 2.18 and 2.20 can be evaluated at any temperature. The reason these calculations were performed at  $T = 473.15$  K (200°C) rather than standard temperature 25°C (298.15 K) is that at the lower temperatures the fugacity values are 6 orders of magnitude lower ( $\sim 10^{-11}$  bar or lower), which tends to introduce round-off and computational errors due to the precision limitations of the computing machines.

The fugacity coefficients for water vapor were calculated between the temperature range of 723.15 – 823.15 K for various pressures. At any given pressure and temperature, molar volume of water vapor was obtained by solving the cubic equation in volume (Eq. 2.26) using the Newton-Raphson Method. Compressibility factor  $Z$  and the fugacity coefficient  $\phi$  were then calculated from Eq. 2.24 and Eq. 2.23, respectively. Parametric study between fugacity coefficient, fugacity and pressure at different temperatures shows that the fugacity coefficient starts deviating significantly from 1 at pressures greater than 2 MPa as shown in Figures 2.1 and 2.2. The value of the fugacity coefficient is approximately 1 at low and moderate pressures implying that the fugacity or the escaping tendency of water vapor is essentially same as its pressure at these conditions. At higher pressures, fugacity coefficient is less than 1, and starts decreasing rapidly above 10 MPa. The implication of these values is that the fugacity or the

escaping tendency of the water vapor is actually lower than what would be indicated by its partial pressure. At any given pressure, the fugacity coefficient is higher for higher temperatures and this difference starts becoming noticeable at pressures greater than 2 MPa.

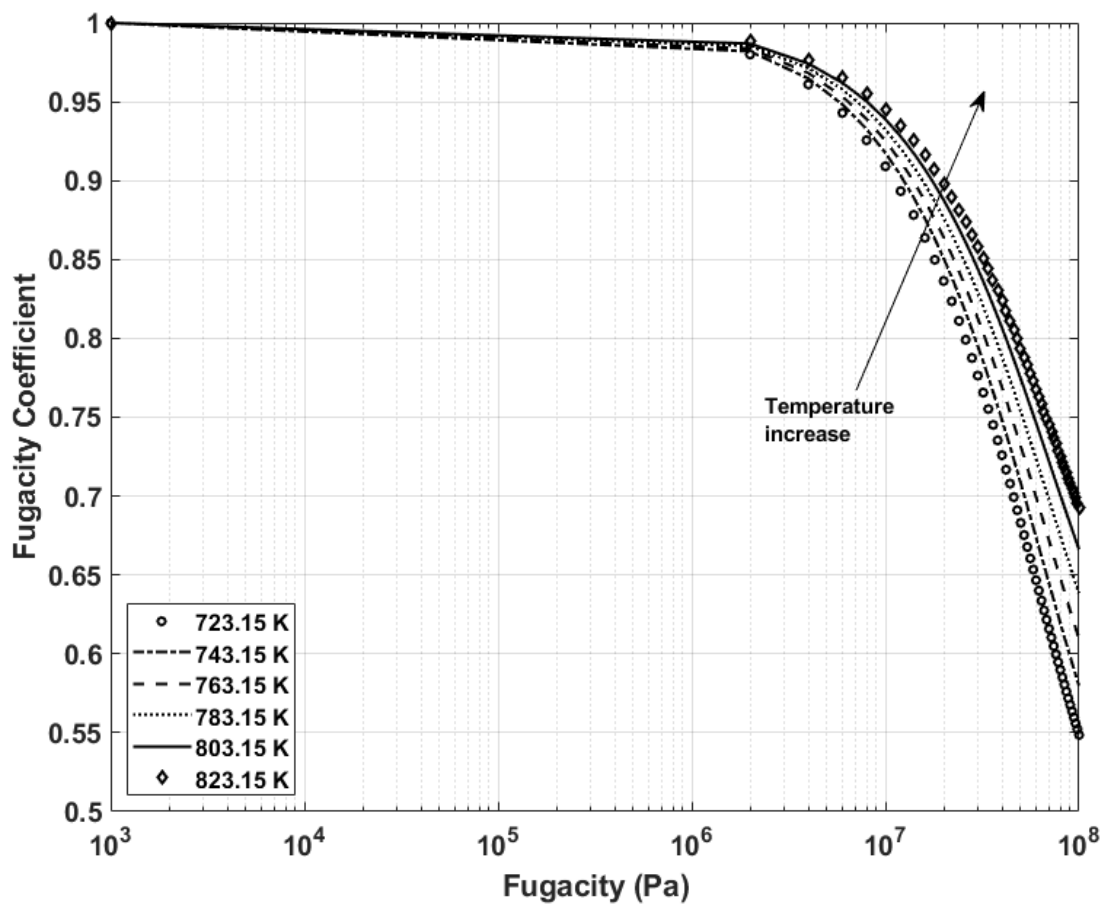


Figure 2.1 Fugacity coefficient as a function of fugacity at different temperatures

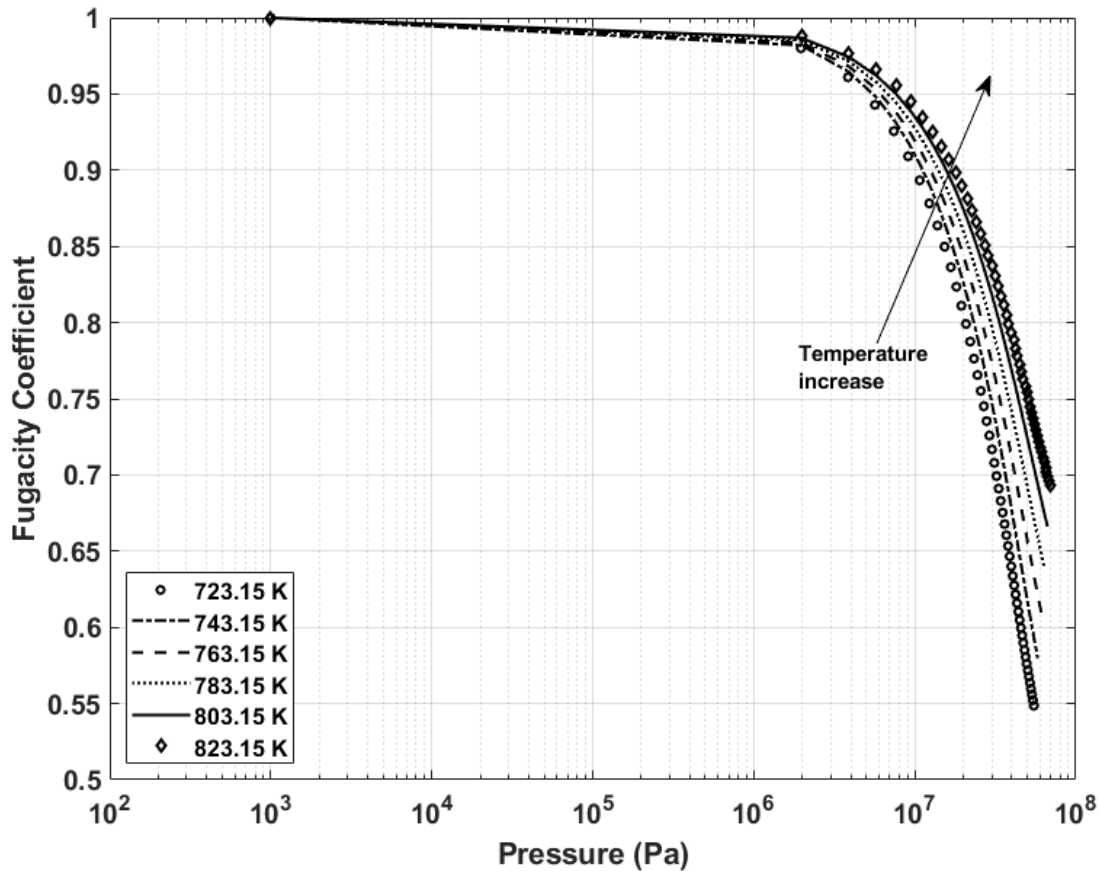


Figure 2.2 Fugacity coefficient as a function of pressure at different temperatures

Thus, the non-ideal behavior of water vapor begins to manifest itself at higher pressures, however, practical operating pressures for the ChHP of interest are much lower ( $< 0.5$  MPa), and for all practical purposes the fugacity coefficient can be assumed to be 1 under these conditions. So, the fugacity is essentially equal to pressure for  $\text{Ca}(\text{OH})_2/\text{CaO}$  system under practical operating conditions.

### 2.3.2 Incorporating temperature dependence on enthalpy

The Clausius-Clapeyron equation where enthalpy dependence on temperature is neglected is as shown below in Eq. 2.34.

$$\ln P = \frac{-106280}{RT} + 16.377 \quad (2.34)$$

On the other hand, accounting for the dependence of enthalpy on temperature leads to the following equation:

$$\ln P = \frac{\left(-109170 + \frac{c_{r,1}T \ln(T)}{1000} + \frac{c_{r,2}T^2}{2 \cdot 10^6} + \frac{c_{r,3}T^3}{6 \cdot 10^9} + \frac{c_{r,4}T^4}{12 \cdot 10^{12}} + \frac{1000 \cdot c_{r,5}}{2T} - c_{r,6} + c_{r,8}\right)}{RT} + 17.14 \quad (2.35)$$

The graphical representation of the two equations is shown in Figures 2.3 and 2.4. It can be clearly seen from the above-mentioned figures that there is a significant difference between the two derived equations, particularly at higher temperatures. The Eq. 2.35 predicts that at 600 K the pressure is only ~15% higher, but the departure increases significantly with the percentage change in pressure value of ~20% and ~35% at temperatures (~650 K) and (~823 K), respectively.

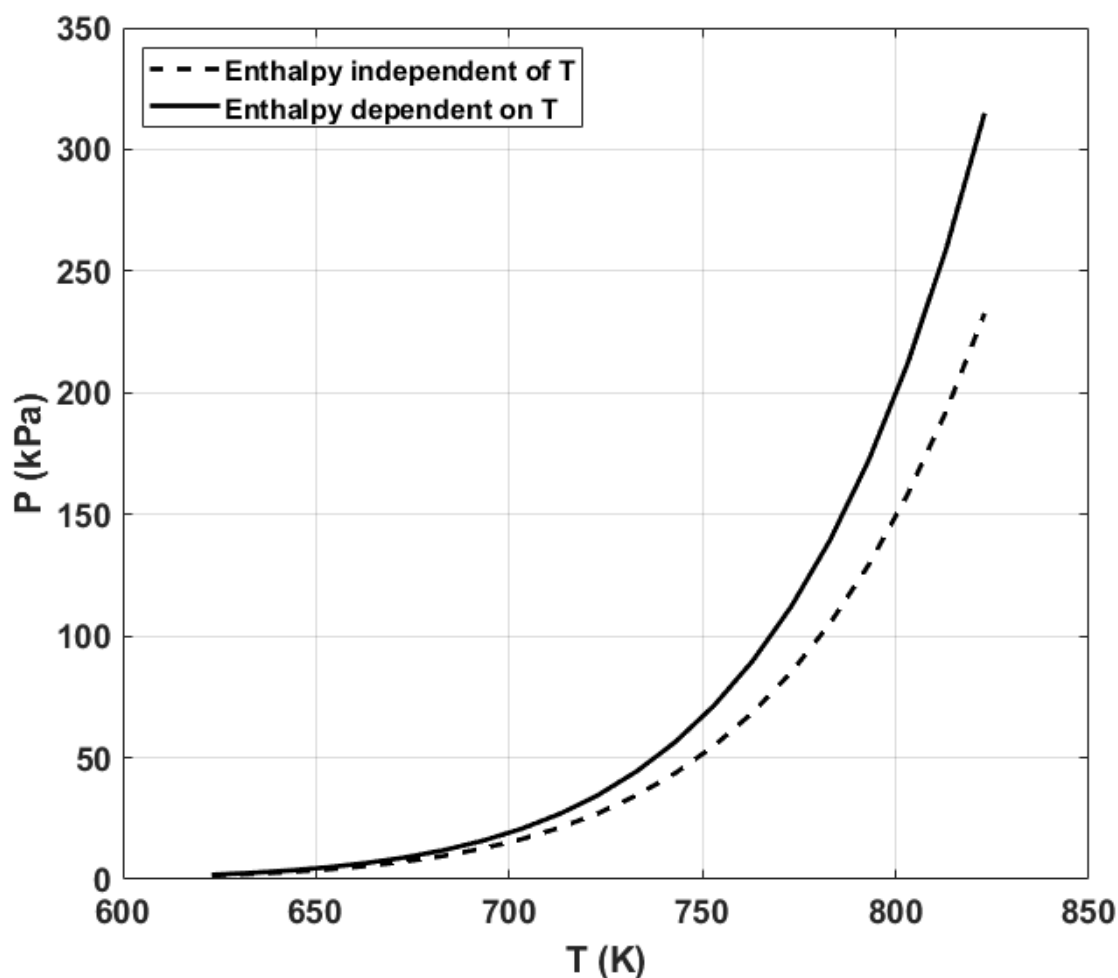


Figure 2.3 Reaction equilibrium for  $\text{Ca(OH)}_2/\text{CaO}$  system in (a) P vs T

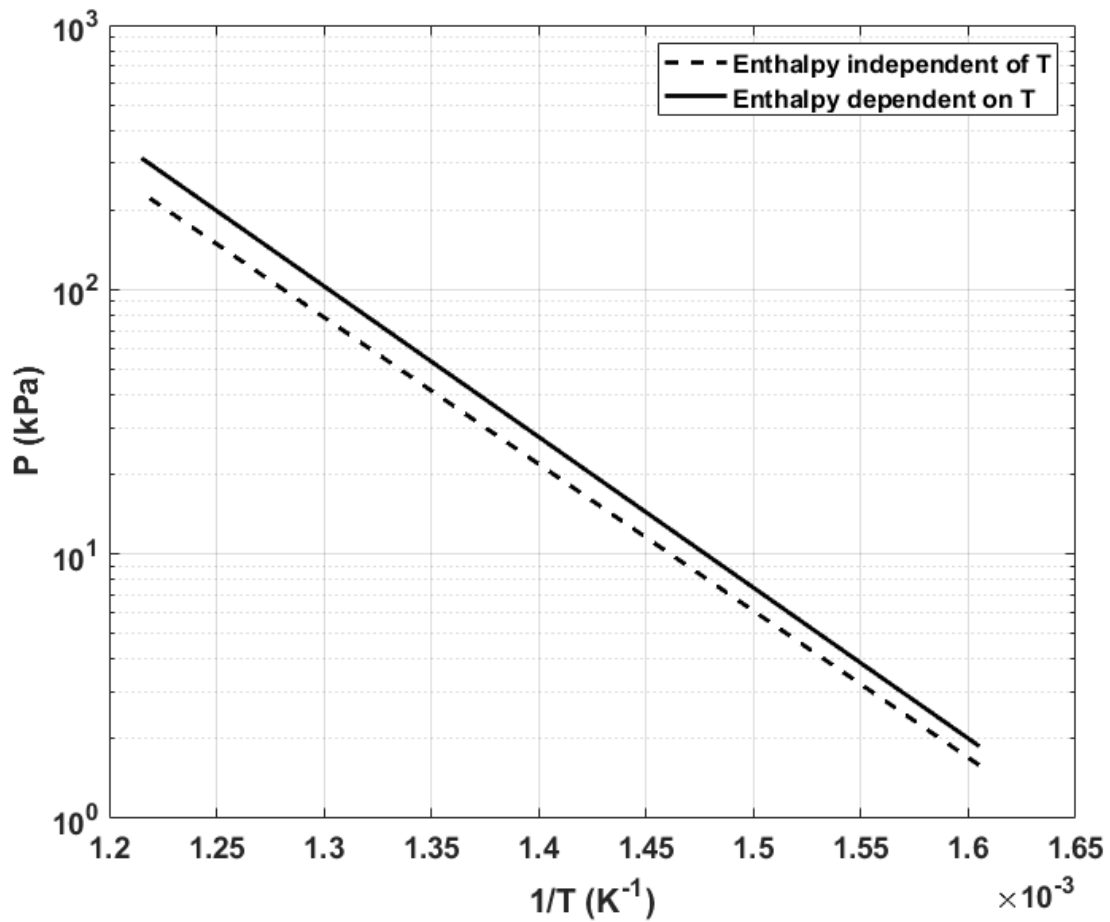


Figure 2.4 Reaction equilibrium for  $\text{Ca(OH)}_2/\text{CaO}$  system in  $\ln P$  vs  $1/T$

Accounting for the temperature dependency of enthalpy of reaction and non-ideality should result in a more accurate equilibrium relationship for the  $\text{Ca(OH)}_2/\text{CaO}$ . Figure 2.5 and Table 2.4 show the comparison between the reported equilibrium relations for  $\text{Ca(OH)}_2/\text{CaO}$  system mentioned in Table 2.1 and the developed equilibrium relation between  $P$  and  $T$  from Eqs. 2.34 and 2.35. Samms et al., [1] obtained the equilibrium relation experimentally which performed well at sub-atmospheric pressure conditions. However, the predictions of the equilibrium relationship did not match well with other reported data at higher pressures. The equilibrium relationship reported by Schaube et al. [8] was based on the experimental approximation and as stated by them, dependent upon the heating rates employed in the experiments. Variation in the heating rates (between 0.03 and 10 K/min) can cause temperature variations ranging from 7-50 K. The theoretical equilibrium relationship reported by [3] was based on thermochemical

values by [4]. The equilibrium relationship between  $P$  and  $T$  derived with the constant enthalpy assumption corresponds well with those presented by [1] and [8]. Accounting for the temperature dependence of reaction enthalpy leads to an equilibrium relationship that predicts higher pressures than those indicated by the other relationships, all of which assume a constant enthalpy change.

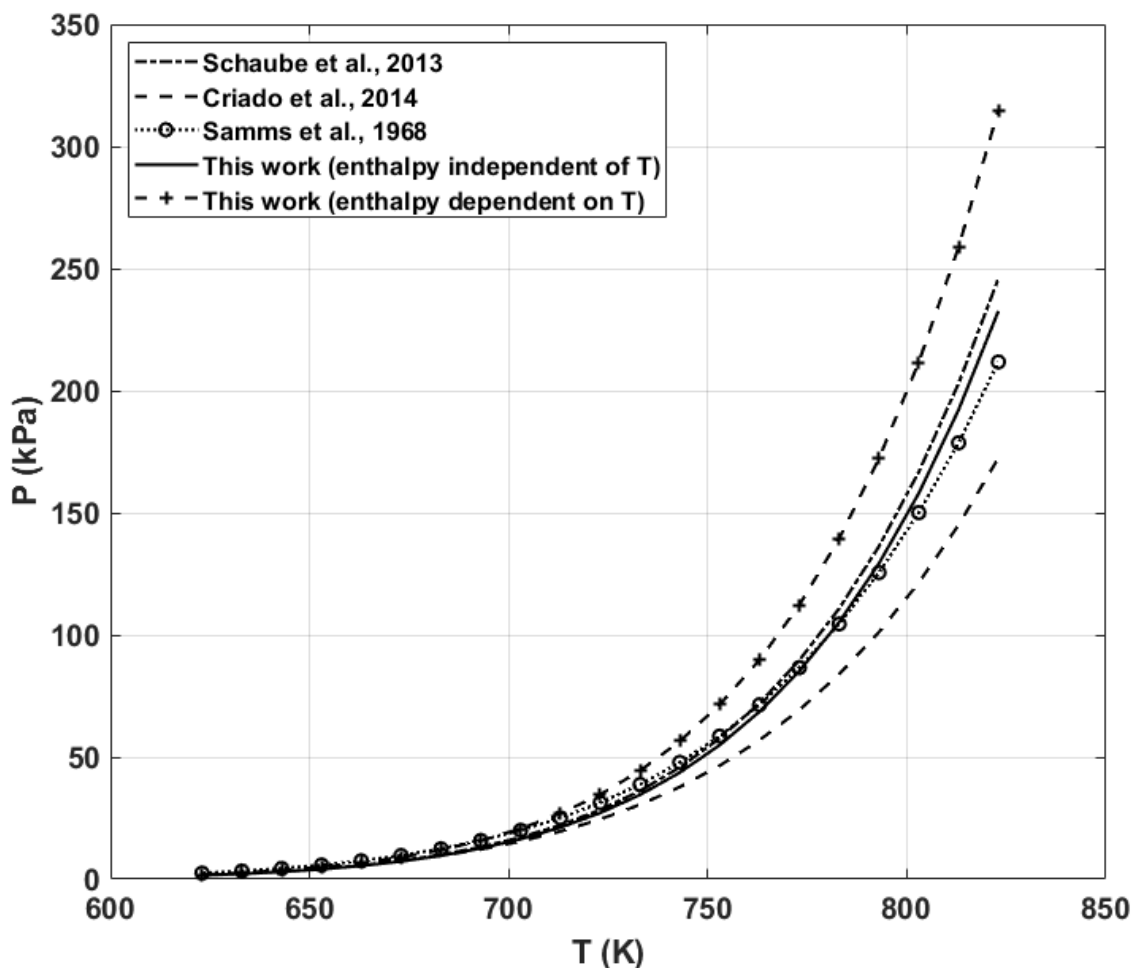


Figure 2.5 Comparison of different Clausius-Clapeyron equations for  $\text{Ca}(\text{OH})_2/\text{CaO}$  system

Figure 2.6 shows the comparison of the five equilibrium relationships with some additional experimental data including those reported by [9] who conducted high temperature hydration reaction. As can be seen, all equations perform reasonably similarly at lower temperatures, however, the variations are particularly apparent at temperatures above 750 K ( $1/T \sim 1.33 \times 10^{-4}$

3). The equilibrium relationship which incorporates the temperature dependence of reaction enthalpy, Eq. 2.35, seems to perform better at these conditions, as may be expected from theoretical considerations.

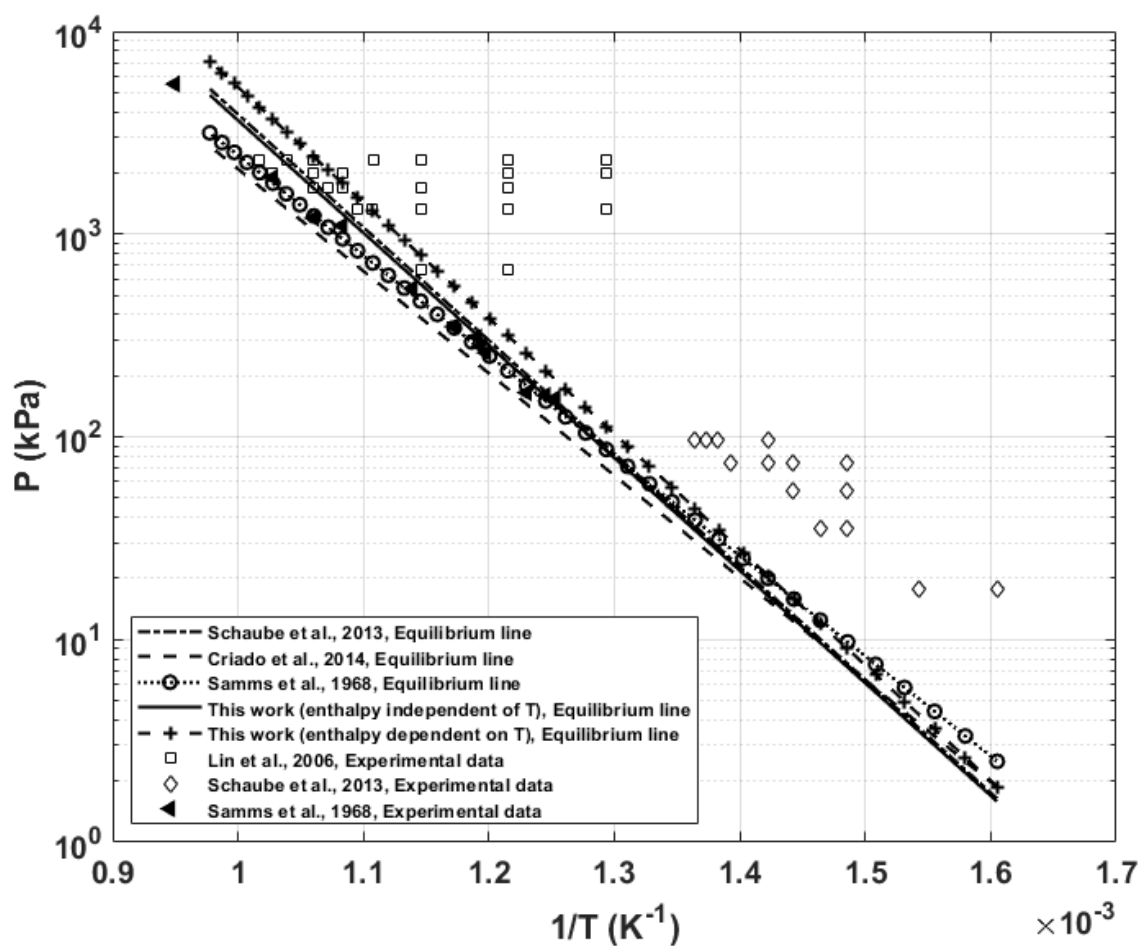


Figure 2.6 Comparison of different Clausius-Clapeyron equations for  $\text{Ca(OH)}_2/\text{CaO}$  with reported experimental data points

Table 2.4 Comparison of equilibrium pressure values at different temperatures

Equilibrium pressure (kPa)					
	Schaube	Criado et	Samms et	This	This
$T$ (K)	et al., [2]	al., [3]	al., [1]	work	work

				(Eq. 2.35)	(Eq. 2.36)
623.15	1.648	1.872	2.516	1.596	1.884
673.15	7.619	7.469	9.763	7.327	9.012
723.15	28.503	24.605	31.406	27.241	34.716
773.15	89.904	69.475	86.85	85.451	112.326
823.15	246.636	172.929	212.286	233.29	315.115

### 2.3.3 Implication of the Derived Clausius-Clapeyron Equilibrium on Ca(OH)<sub>2</sub>/CaO and ChHP System

ChHPs based on Ca(OH)<sub>2</sub>/CaO works on the principle of reversible chemical reaction where the cycling of water between the hydration/dehydration reaction of Ca(OH)<sub>2</sub>/CaO is accomplished by means of a condensation-evaporation cycle. Figure 2.7 shows the dehydration process in which Ca(OH)<sub>2</sub> reacts endothermically at a medium temperature  $T_M$  (300–650°C) and low-pressure  $P_L$  which is under atmospheric or sub-atmospheric pressure (1–100 kPa). The reaction produces CaO(s) and H<sub>2</sub>O vapor that is driven out of the chemical bed. The vapor can then be condensed by removing heat at a lower temperature  $T_L$ . In the hydration process, liquid water is then pumped to a high-pressure  $P_H$  (1–4000 kPa) and heated to the corresponding saturation temperature  $T_{sat}$ . The resulting H<sub>2</sub>O vapor is driven into the high-pressure chemical bed of CaO. This reacts exothermically, releasing heat at a high temperature  $T_H$  (350–800°C).

The operating conditions for the dehydration reaction are determined by specifying either  $T_M$ ,  $T_L$ , or  $P_L$ : 1) Specifying the temperature of the reactor  $T_M$  fixes the pressure  $P_L$  and hence the temperature  $T_L$  needed in the condenser as dictated by the water vapor-liquid equilibrium; 2) conversely, if the condenser temperature  $T_L$  is specified, then temperature  $T_M$  needed for dehydration is determined by the reaction equilibrium corresponding to pressure  $P_L$ ; 3) Finally, if the operating pressure  $P_L$  is specified, then both the dehydration reaction temperature  $T_M$  and the condensation temperature a  $T_L$  are fixed from the two equilibrium lines. The reaction equilibrium line corresponding to Eq. 2.35 where temperature dependence of reaction enthalpy

is accounted for lies to the right of the reaction equilibrium line corresponding to Eq. 2.34 where reaction enthalpy is assumed to be constant. For any operating pressure  $P_L$  (scenario 3 above), this leads to lower dehydration reaction temperature requirement according to Eq. 2.35 than Eq. 2.34. Similar lower reaction temperature requirement can be inferred for the situation where the condensation temperature  $T_L$  is fixed. On the other hand, if the reaction temperature  $T_M$  is fixed, then equilibrium pressure predicted by Eq. 2.35 and corresponding condensation temperature are both higher than those predicted by Eq. 2.34.  $T_L$  in almost all cases being sub-ambient, this results in less severe heat removal duties for the condenser operation.

Similar implications for the hydration process can be inferred by considering the relationship between  $P_H$ ,  $T_H$ , and  $T_{sat}$ . The ChHP is typically operated to boost the temperature to some desired temperature  $T_H$ . It can be seen that reaction equilibrium governed by Eq. 2.35 leads to a higher value of  $P_H$  than that governed by Eq. 2.34. Correspondingly, the saturation temperature  $T_{sat}$  is also higher when Eq. 2.35 is used for describing the hydration reaction equilibrium. This implies higher heat and pressurization duties for the water condensed during the dehydration process. Conversely, if  $T_{sat}$  (or  $P_H$ ) are fixed, then a lower temperature boost is predicted by Eq. 2.34 than that by Eq. 2.35.

Consideration of temperature dependence on enthalpy thus has significant implications for the design and operation of the  $\text{Ca(OH)}_2/\text{CaO}$  ChHP. The operating conditions for the dehydration step are likely to be less severe than those determined by ignoring the temperature dependence of the reaction enthalpy. Conversely, more severe operating conditions will be required to obtain any desired higher temperature or smaller temperature boost will be achieved at the same conditions when temperature dependence of enthalpy is taken into account. In any case, incorporating the temperature dependence of thermodynamic quantities will result in more accurate equilibrium relationships that governs the system behavior.

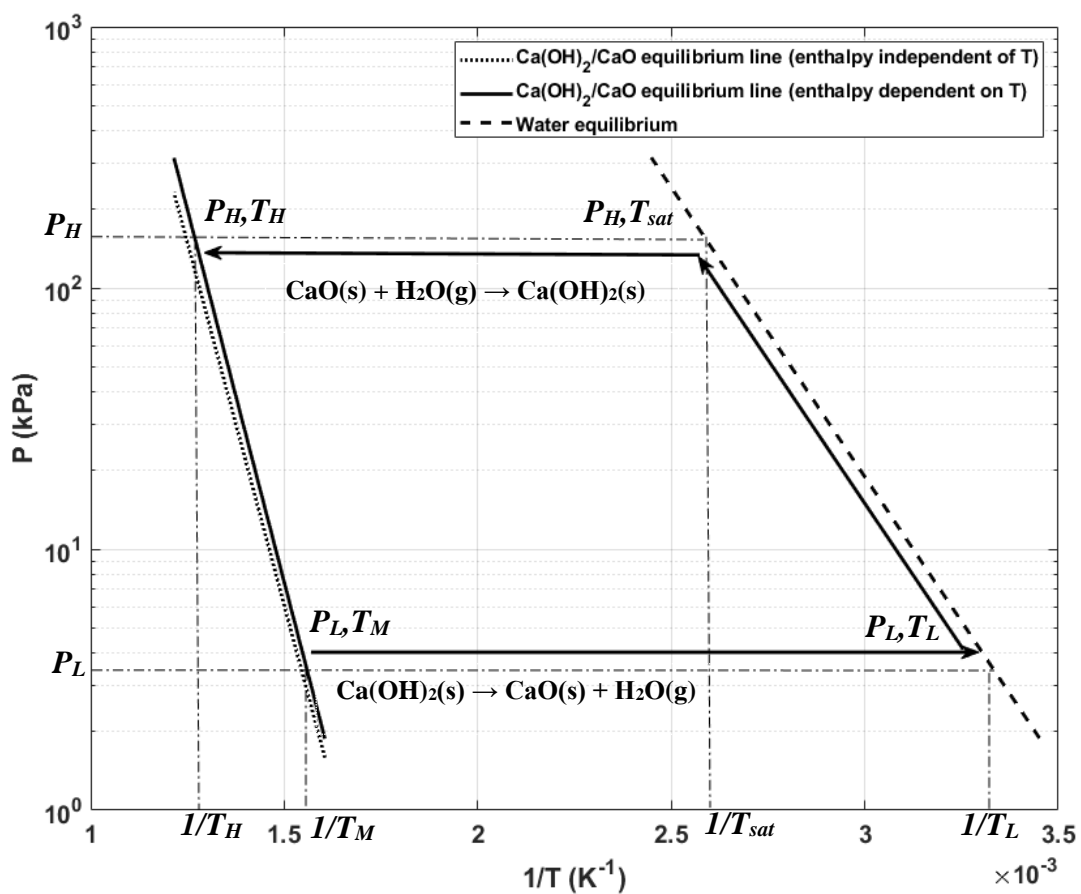


Figure 2.7 Derived Clausius-Clapeyron  $\text{Ca(OH)}_2/\text{CaO}$  equilibrium line and water equilibrium

## Nomenclature

### Abbreviations

ChHP	chemical heat pump
EOS	equation of state
SRK	Soave-Redlich-Kwong
TCS	thermochemical energy storage
TES	thermal energy storage

### Latin symbols

$a$	activity
-----	----------

$a_{SRK}$	energy parameter
$b$	molecular co-volume
$B$	parameter required for calculation in Eq. 25
$c$	parameter constant for enthalpy and entropy
$f$	fugacity
$G$	Gibbs free energy
$H$	enthalpy
$K$	equilibrium constant
$M$	parameter required for calculation in Eq. 29
$n_r$	number of species in reactant
$n_p$	number of species in product
$N$	parameter required for calculation in Eq. 30
$P$	pressure
$Q_{in}$	heat in
$Q_{out}$	heat out
$R$	gas constant
$S$	entropy
$T_r$	reduced temperature
$T$	temperature
$V$	molar volume
$Z$	compressibility factor

*Greek symbols*

$\Delta$	difference
$\zeta$	constant of integration
$\nu$	stoichiometric coefficient
$\varphi$	fugacity coefficient
$\omega$	acentric factor

*Subscript*

<i>eq</i>	equilibrium
<i>H</i>	high
<i>i</i>	species
<i>j</i>	range or indices
<i>L</i>	low
<i>M</i>	medium
<i>r</i>	reaction

## References

1. J. A. C. Samms, B.E. Evans, 1968. "Thermal Dissociation of  $\text{Ca(OH)}_2$  at Elevated Pressures." *Journal of Applied Chemistry* 18:5–8. <https://doi.org/10.1002/jctb.5010180102>.
2. F. Schaube, L. Koch, A. Wörner, and H. Müller-Steinhagen. 2012. "A thermodynamic and kinetic study of the de- and rehydration of  $\text{Ca(OH)}_2$  at high  $\text{H}_2\text{O}$  partial pressures for thermo-chemical heat storage," *Thermochimica Acta.* 538:9–20. <https://doi.org/10.1016/j.tca.2012.03.003>.
3. Y. A. Criado, M. Alonso, J. C. Abanades, and Z. Anxionnaz-Minvielle. 2014. "Kinetics of the  $\text{CaO/Ca(OH)}_2$  Hydration/Dehydration Reaction for Thermochemical Energy Storage Applications." *Industrial and Engineering Chemistry Research* 53:12594–12601. <https://doi.org/10.1021/ie404246p>.
4. I. Barin, G. Platzki, 1995. *Thermochemical Data of Pure Substances*, 3<sup>rd</sup> edition. Weinheim:New York, VCH.
5. M.W. Chase., 1998. *NIST-JANAF Thermochemical Tables*, 4<sup>th</sup> Edition. Journal of Physical and Chemical Reference Data. Monograph 9:1–1951.
6. J.M. Prausnitz, R.N. Lichtenthaler, E.G. de Azevedo, 1999. *Molecular Thermodynamics of Fluid-Phase Equilibria*, 3<sup>rd</sup> edition. New Jersey, Prentice Hall PTR.
7. J. Szarawara, A. Gawdzik, 1989. "Method of Calculation of Fugacity Coefficient from Cubic Equations of State." *Chemical Engineering Science* 44:1489–1494. [https://doi.org/10.1016/0009-2509\(89\)80025-9](https://doi.org/10.1016/0009-2509(89)80025-9).
8. F. Schaube, A. Kohzer, J. Schütz, A. Wörner, and H. Müller-Steinhagen. 2013. "De- and rehydration of  $\text{Ca(OH)}_2$  in a reactor with direct heat transfer for thermo-chemical heat storage. Part A: Experimental results," *Chemical Engineering Research and Design* 91:856–864. <https://doi.org/10.1016/j.cherd.2012.09.020>.
9. S. Lin, M. Harada, Y. Suzuki, H. Hatano, 2006. "CaO Hydration Rate at High Temperature (~1023 K)." *Energy Fuels* 20: 903–908. <https://doi.org/10.1021/ef050257o>.

## Chapter 3 Kinetic Modeling of $\text{Ca}(\text{OH})_2$ Decomposition

### 3.1 Objective

The kinetic analysis of  $\text{Ca}(\text{OH})_2/\text{CaO}$  is important in understanding the reaction and energy storage/discharge rates for designing the ChHP system. Several studies on the kinetics of  $\text{Ca}(\text{OH})_2$  decomposition have been carried out, with various researchers reporting different kinetic parameters and decomposition mechanisms [1-4]. The difference in the kinetic parameters can be attributed to variations in the raw material composition, particle size, alteration in experimental methods and instruments. Long et. al [5] studied the kinetic analysis of  $\text{Ca}(\text{OH})_2$  under non-isothermal decomposition at different heating rates using thermogravimetric analyzer. MacCallum and Tanner [6] conclude in their study that the activation energy and the formal reaction order must be determined only from the results of isothermal decomposition processes. Gorbachev and Logvineko [7] also observed discrepancies in the kinetics determination under isothermal and non-isothermal conditions and asserted the importance of isothermal kinetic study for the determination of kinetic parameters. So, it is necessary to obtain the corresponding activation energy, rate constant and pre-exponential factor under isothermal conditions for  $\text{Ca}(\text{OH})_2/\text{CaO}$  system. Further, it is also necessary to investigate whether the incorporation of an inert substance alters the kinetics of the process.

This chapter describes a better understanding of the  $\text{Ca}(\text{OH})_2$  decomposition kinetics under isothermal conditions and to examine the effect of an inert additive on the reaction rate. Kinetic analysis of pure  $\text{Ca}(\text{OH})_2$  decomposition at different temperatures was first conducted using a thermogravimetric analyzer (TGA) yielding estimates of the kinetic parameters - activation energy and Arrhenius constant. The second part of the study investigated and quantified the kinetics of the  $\text{Ca}(\text{OH})_2$  decomposition resulting from the incorporation of an additive material – inert calcium titanate ( $\text{CaTiO}_3$ ) – at different compositions.

### 3.2 Materials and Methods

#### 3.2.1 Reagents and apparatus

Calcium hydroxide powder ( $\text{Ca}(\text{OH})_2$ )  $\geq 97.9\%$  pure, was procured from J.T. Baker Chemicals, 98% purity,  $d_{50} = 5.5\mu\text{m}$ .  $\text{CaTiO}_3 \geq 99.0\%$  purity was obtained from Strem Chemicals. The

theoretical densities of  $\text{Ca(OH)}_2$  and  $\text{CaTiO}_3$  are  $2200 \text{ kg/m}^3$  and  $3980 \text{ kg/m}^3$ , respectively. Table 3.1 shows the chemical composition and characteristics of  $\text{Ca(OH)}_2$  and  $\text{CaTiO}_3$ .

Solid reactant was pelletized using pellet press (TPD 0 Desktop tablet press) resulting in pellets 3.2 mm diameter x 5.6 mm height. The mass of individual  $\text{Ca(OH)}_2$  pellets ranged from 70–80 mg while that of the composite pellets ranged from 100–110 mg. The thermal decomposition of  $\text{Ca(OH)}_2$  reaction kinetics for isothermal conditions was investigated on a TGA (TA Instruments – Q500) thermal analyzer.

Table 3.1 Chemical composition of  $\text{Ca(OH)}_2$  and  $\text{CaTiO}_3$

Materials		Composition	
$\text{Ca(OH)}_2$	$\text{Ca(OH)}_2 \geq 97.9\%$	Mg, alkali metal $\leq 0.6\%$	Sulfur compounds $\leq 0.03\%$
$\text{CaTiO}_3$	$\text{CaTiO}_3 \geq 99.0\%$	-	-

### 3.2.2 Experimental Procedure

In order to study the kinetics of  $\text{Ca(OH)}_2$  decomposition under isothermal conditions, mass loss from the pellets was monitored at five different temperatures - 400, 425, 450, 475 and  $500^\circ\text{C}$  - using the TGA. The pellet was heated to desired temperature at a heating rate of 15 K/min, and then maintained at that temperature for a maximum of 150 min. The experiments were conducted under pure  $\text{N}_2$  environment by flowing the gas at a flow rate of 20 mL/min. Fig. 1 shows the temperature profile for the decomposition temperature of  $400^\circ\text{C}$ . The mass loss up to the temperature of  $\sim 120^\circ\text{C}$  is attributable to the drying or removal of unbounded moisture present in the sample. Subsequent mass loss was attributed to the decomposition reaction, with the reaction during the heating period termed non-isothermal decomposition. Once the temperature reached to desired isothermal temperature, the conversion was attributed to isothermal conditions.

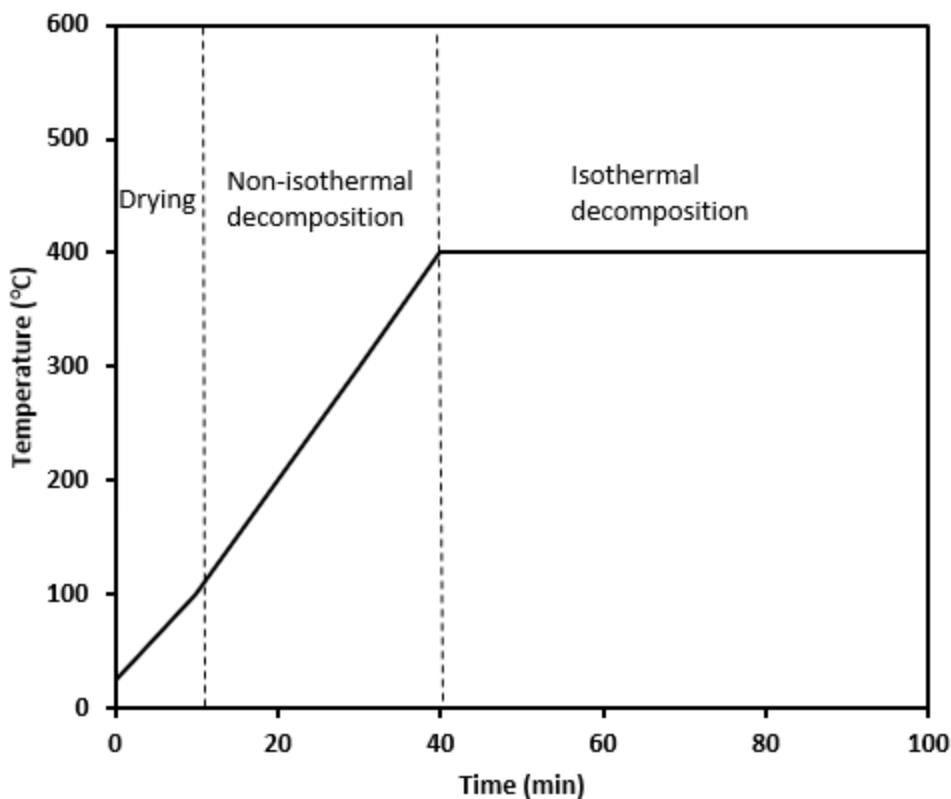


Figure 3.1 Temperature program for thermal decomposition of Ca(OH)<sub>2</sub>

### 3.2.3 Composite Material Synthesis

The Ca(OH)<sub>2</sub> and CaTiO<sub>3</sub> were blended in the lab-scale blender (Janke & Kunkel A10S2) 3 times for 20 mins each with the composition of 1:0.5 and 1:1 Ca(OH)<sub>2</sub>:CaTiO<sub>3</sub> by weight %, respectively. After the blending, the powder was dried in the furnace at 120°C for 5 hr. Once the powder was dried, the pellets were formulated as described above. The kinetics of the composite pellets was studied using the TGA following the same procedure mentioned in section 3.2.2.

### 3.2.4 Ca(OH)<sub>2</sub> Pellet Enhancement Concept

As Ca(OH)<sub>2</sub> decomposes into CaO there is a decrease in the volume and particle size with the liberation and removal of H<sub>2</sub>O. During the hydration process, the H<sub>2</sub>O reacts with CaO to form Ca(OH)<sub>2</sub> and thus the volume increases, increasing the particle size. Repeated dehydration/hydration cycles affect the structural integrity of the solid particles in the form of pellets because of vapor transport in and out during reactions.

When an inert agent such as  $\text{CaTiO}_3$  is incorporated with  $\text{Ca(OH)}_2$ , the variation in the pellet volume is reduced as the volume of the inert  $\text{CaTiO}_3$  does not change during forward or reverse reactions. The particles of inert  $\text{CaTiO}_3$  act as a scaffolding for  $\text{Ca(OH)}_2$  particles and help maintain the structural integrity of the pellet as shown in Fig. 3.2. The addition of  $\text{CaTiO}_3$  as inert agent helps increasing the reaction surface area which will be quite effective for increasing the rate of reaction.

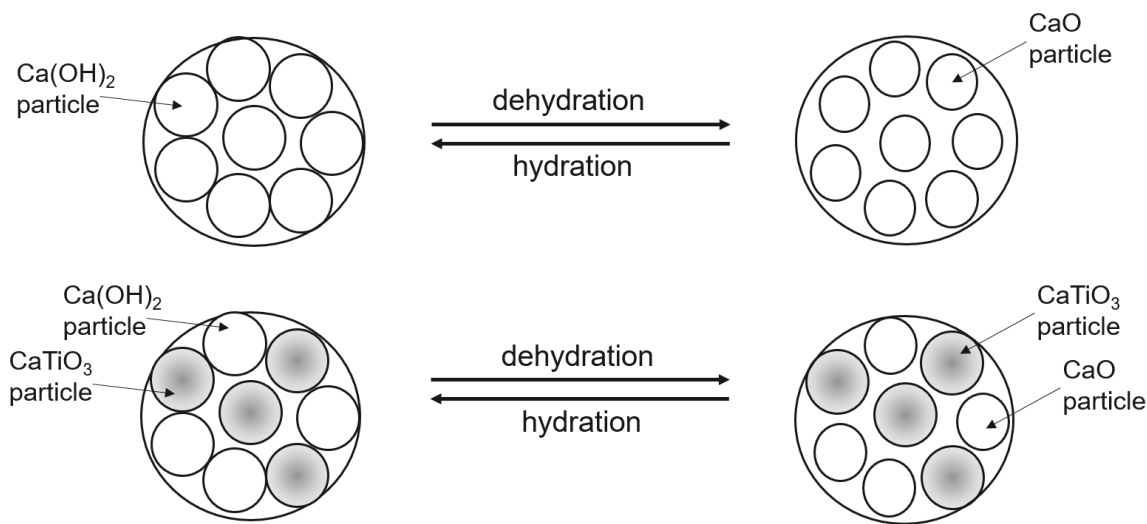


Figure 3.2 A schematic representation of pellet enhancement process

### 3.3 Results and Discussions

#### 3.3.1 Isothermal Decomposition of Pure $\text{Ca(OH)}_2$

Fig. 3.3 (a)-(e) shows the TGA curves of  $\text{Ca(OH)}_2$  decomposition where % mass change and temperature are plotted with respect to time at different maximum temperatures i.e., 400, 425, 450, 475, and 500°C, respectively. The mass loss in first 20 min is due to the loss of moisture or unbounded water present within the sample. Initiation of  $\text{Ca(OH)}_2$  decomposition was observed when the temperature reached  $\sim 370^\circ\text{C}$ . Table 3.2 shows the % mass change at different times for different maximum temperatures. The % mass change after the loss of unbound moisture but before reaching the maximum temperature is attributed to non-isothermal decomposition whereas % mass change after the temperature is kept constant once maximum temperature is reached is due to isothermal decomposition. It can be observed from the results that as the maximum temperature is increased the decomposition is faster, as can be expected from higher rate constants at higher temperatures. With increase in maximum

temperature, the % of mass change is contributed more by non-isothermal decomposition. Results showed that the % mass change due to non-isothermal decomposition were 2.23% and 14.15% for maximum temperatures of 400°C and, 500°C, respectively.

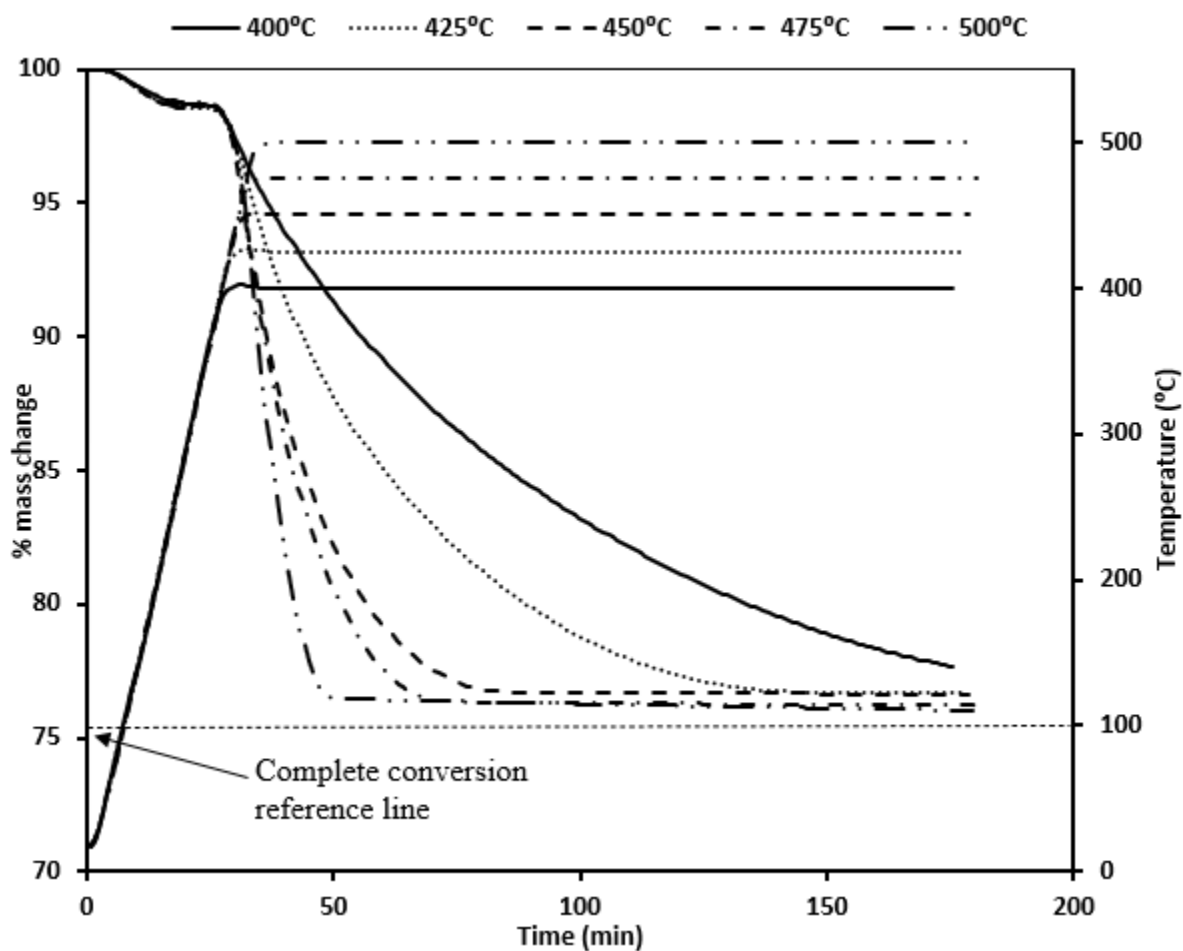


Figure 3.3 Percentage mass loss vs time at different maximum temperatures: a) 400°C; b) 425°C; c) 450°C; d) 475°C; e) 500°C

Table 3.2 Comparison of % mass change of pure  $\text{Ca}(\text{OH})_2$  at different decomposition temperature

Maximum Temperature (°C)	Initial % mass change at max. temperature	% mass change at max. temperature (time = 50 min)	% mass change at max. temperature (time = 80 min)	Final % mass change at max. temperature (time = 180 min)
400	2.23	8.87	14.34	22.33
425	2.95	12.35	18.83	23.34
450	6.59	17.78	23.13	23.35

475	10.77	19.59	23.65	23.70
500	14.15	23.52	23.67	23.80

The decomposition conversion ( $X$ ) of  $\text{Ca}(\text{OH})_2$  is calculated using Eq. 3.1 where  $m_t$  is the mass of pellet after time  $t$ ;  $m_i$  is the initial mass of the pellet;  $M_{\text{Ca}(\text{OH})_2}$  and  $M_{\text{CaO}}$  are the molar mass of calcium hydroxide and calcium oxide, respectively.

$$X = \frac{1 - \frac{m_t}{m_i}}{1 - \frac{M_{\text{CaO}}}{M_{\text{Ca}(\text{OH})_2}}} \quad (3.1)$$

Fig. 3.4 shows the conversion profiles with respect to time at different decomposition temperatures based on the above results. It can be found that the conversion is faster at higher decomposition temperatures as can be expected from the rate constant dependence on temperature. At  $500^\circ\text{C}$ , the conversion was 96.5% within 50 min. Corresponding conversions at the same time (50 min) for 475, 450, 435 and  $400^\circ\text{C}$  were 79.1%, 73.2%, 50.1% and 35.9%, respectively. The final conversion for 500, 475, 450, 435 and  $400^\circ\text{C}$  were 98.47%, 97.78%, 96.01%, 95.85%, and 91.74% respectively.

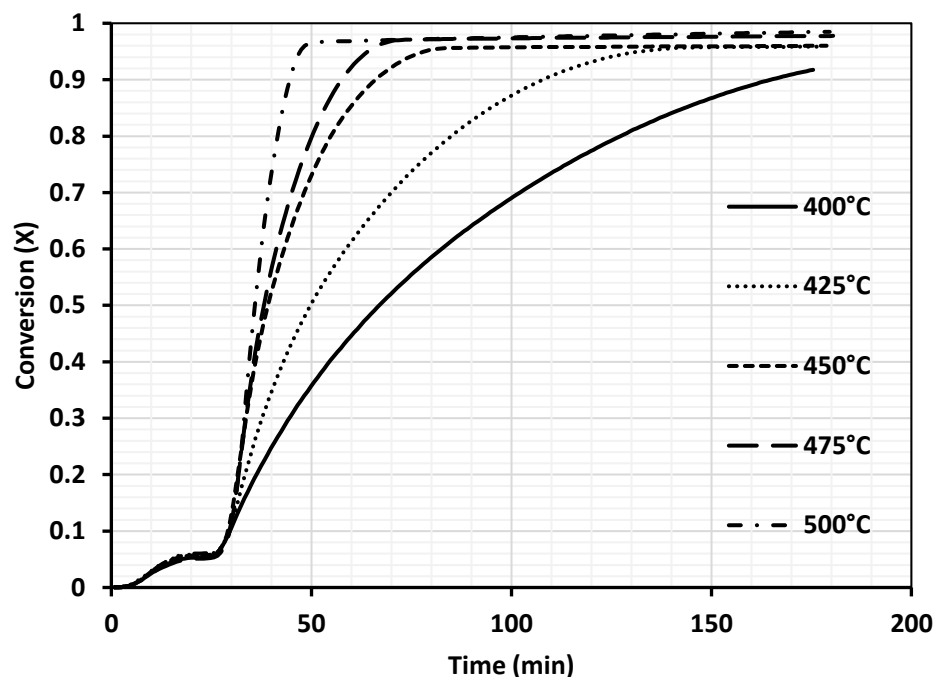


Figure 3.4 Conversion profile vs time at different isothermal temperature for decomposition of  $\text{Ca}(\text{OH})_2$

### 3.3.2 Kinetics of Decomposition of $\text{Ca}(\text{OH})_2$

The rate of dehydration process is parameterized by variables: temperature, conversion, and the mechanism function. Hence, the rate of conversion during decomposition process described by Eq. 3.2.

$$\frac{dX}{dt} = k(T)f(X) \quad (3.2)$$

Where  $X$  is conversion,  $k(T)$  represents the rate constant and  $f(X)$  is the mechanism function. The temperature dependence of the rate constant is shown in Eq. 3.3, where  $E$  and  $A$  are the activation energy and Arrhenius constant, respectively.

$$k(T) = A \exp\left(-\frac{E}{RT}\right) \quad (3.3)$$

For first order reaction, the  $f(X)$  is given by Eq. 3.4, and integral method is used to determine the rate constant  $k$ . In a more general case, the function  $f(X)$ , was assumed to be described by the power law, that is,  $(1-X)^n$ , as shown in Eq. 3.5.

$$f(X) = 1 - X \quad (3.4)$$

$$\frac{dX}{dt} = (1 - X)^n k(T) \quad (3.5)$$

A trial-and-error procedure was used to determine the reaction order with values of  $n$  being 0, 1, and 2 in the trials. Eq. 3.5 was integrated (assuming a constancy of the rate constant for isothermal decomposition) and the resulting equations subjected to a linear regression fit with the experimental data. The reaction was found to be first order ( $n=1$ ), with a linear relationship between  $\ln(1-X)$  and  $t$  exhibited by the experimental data as shown in Fig. 3.5 for the different isothermal temperatures i.e., 400, 425, 450, 475, and 500°C, respectively. The results of regression were not satisfactory with  $n = 0$  or 2, indicating that the decomposition kinetics was not zero and second order with respect to  $\text{Ca(OH)}_2$  concentration.

The rate constant values are obtained from the absolute value of the slope of the regression line. The rate constant values at the different temperatures with the respective correlation coefficients are presented in Table 3.3. The increase in rate constant values with temperature can be seen from the table.

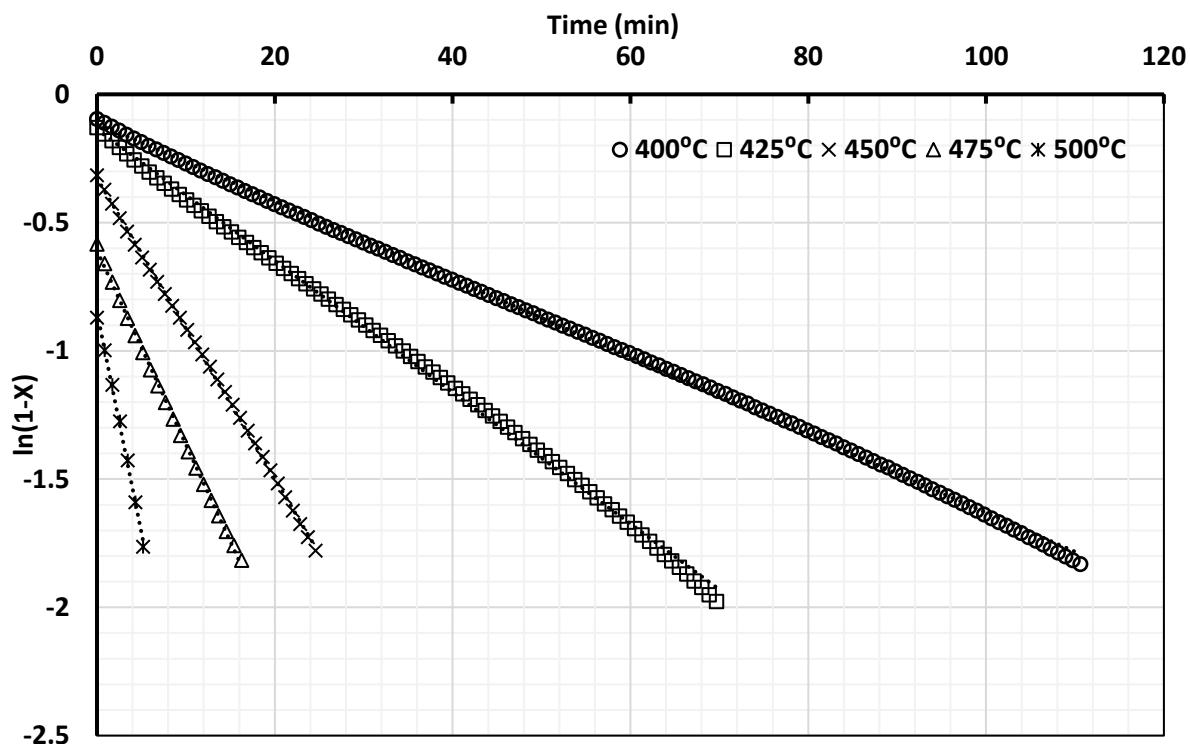


Figure 3.5 Linear regression results for rate constant estimation for decomposition of  $\text{Ca}(\text{OH})_2$  at isothermal temperatures: a) 400°C; b) 425°C; c) 450°C; d) 475°C; e) 500°C

Table 3.3 Rate constant for  $\text{Ca}(\text{OH})_2$  decomposition as a function of temperature

Isothermal temperature (°C)	Rate constant (k) ( $\text{min}^{-1}$ )	Linear Regression Equation	Correlation coefficient ( $R^2$ )
400	0.0152	$y = -0.0152x - 0.1126$	0.9993
425	0.0256	$y = -0.0256x - 0.1365$	0.9988
450	0.0585	$y = -0.0585x - 0.3273$	0.9997
475	0.0756	$y = -0.0756x - 0.6094$	0.9991
500	0.172	$y = -0.172x - 0.8486$	0.9970

Eq. 4 is linearized, as shown in Eq. 3.6, for obtaining the values of the activation energy  $E$  and the Arrhenius factor  $A$ . Fig. 3.6 shows the plot between  $\ln(k)$  vs  $1/T$ .

$$\ln k = \left(-\frac{E}{R}\right)\frac{1}{T} + \ln A \quad (3.6)$$

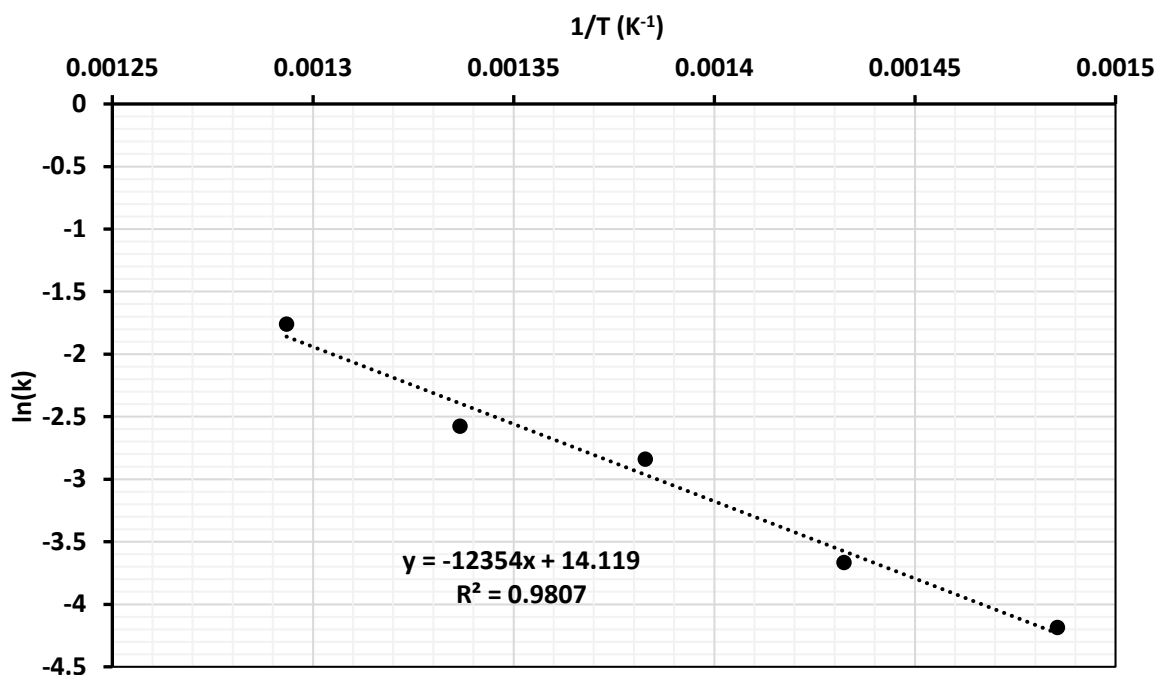


Figure 3.6 Linear regression curve between  $\ln(k)$  vs  $1/T$  for activation energy and Arrhenius constant estimation for decomposition of  $\text{Ca}(\text{OH})_2$

The correlation coefficient of the linear regression results is 0.9807 and the kinetic parameters obtained are -12354 which corresponds to  $-E/R$  value and  $\ln(A)$  is 14.119. Thus, the activation energy ( $E$ ) obtained was 102.71 kJ/mol and Arrhenius constant ( $A$ ) was  $1.35 \times 10^6 \text{ min}^{-1}$ .

The error analysis of TGA measurements can be evaluated as given by Eq. 3.7 [8].

$$u_s = \sqrt{\left(\frac{\partial f}{\partial T} u(T)\right)^2 + \left(\frac{\partial f}{\partial x} u(x)\right)^2} \quad (3.7)$$

Where  $u_s$  is the system error, the mass inaccuracy of the electronic balance is  $\pm 0.0001 \text{ mg}$  and the temperature inaccuracy of measurements is  $\pm 0.01^\circ\text{C}$ . The estimated error limit for TGA system is 2.26%.

The error for activation energy and natural logarithm of Arrhenius constant can be obtained by Eq. 3.8.

$$u_{E/\ln A} = \sqrt{u_s^2 + u_{fit}^2} \quad (3.8)$$

Where  $u_{fit}$  is the fitting error for activation energy and natural logarithm of Arrhenius constant. The analysis reveals the errors based on the linear regression value and TGA results for  $E$  to be ~8.4% and ~9.4% for  $\ln A$ .

Incorporating the temperature dependence of the rate constant from Eq. 3.6 for first order reaction leads to Eq. 3.9, and the obtained rate constant equation upon substitution of experimental estimates of  $A$  and  $E$  is shown in Eq. 3.10.

$$\frac{dX}{dt} = k(1 - X) \quad (3.9)$$

$$k = 1.35 \times 10^6 e^{\frac{-12354}{T}} \quad (3.10)$$

Integrating Eq. 3.9 yields the following conversion-time relationship for isothermal decomposition as shown in Eq. 3.11.

$$X_f = 1 - (1 - X_i)e^{-kt} \quad (3.11)$$

The conversions calculated using the above equation are compared to the thermogravimetric experimental data as shown in Fig. 3.7. The calculated and experimental values show good agreement with the relative mean errors between the derived equation and experimental data being 4.7%, 1.9%, 6.0%, 4.3% and 1.3% at 400, 425, 450, 475 and 500°C, respectively. The maximum errors obtained between the mathematically derived equation and reported experimental data are 10.6%, 6.4%, 8.1%, 5.9% and 3.4% at 400, 425, 450, 475 and 500°C, respectively.

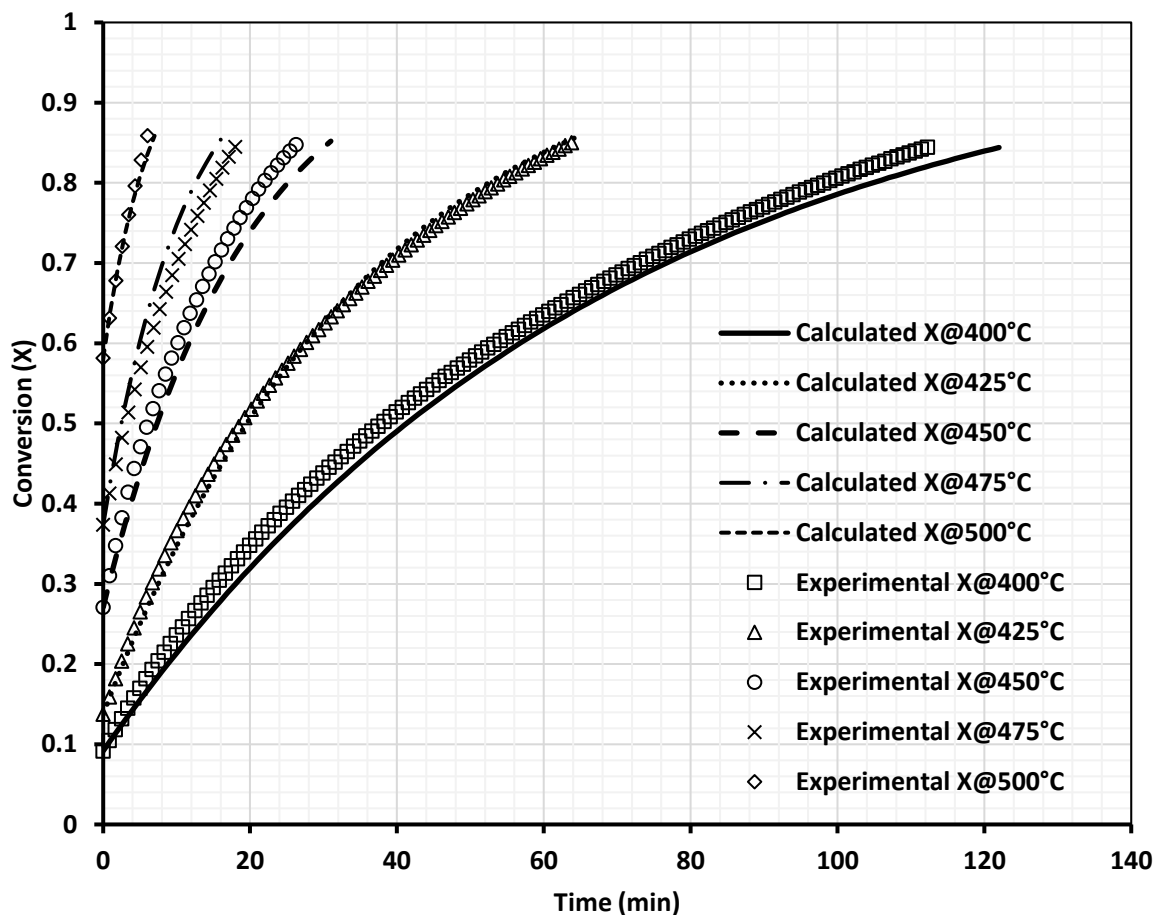


Figure 3.7 Comparison of isothermal derived equation with experimental data

The temperature during the non-isothermal phase of the experiment can be described by the equation  $T = T_o + \beta t$ , where,  $T_o$  is the initial temperature and  $\beta$  is the heating rate in K/min. Under these conditions, the conversion-time relationship can be described by the following Eq. 3.12, obtained by substituting the temperature-time relationship in Eq. 3.10.

$$\frac{dX}{dt} = 1.35 \times 10^6 e^{\frac{-12354}{T_o + \beta t}} (1 - X) \quad (3.12)$$

Eq. 3.12, obtained for non-isothermal condition is numerically integrated further and the comparison between the derived equation and experimental data is shown in Fig. 3.8. The comparison is conducted at 500°C due to availability of adequate experimental data during the non-isothermal period. The agreement between the calculated and experimental data indicates that the rate expression based on the kinetic parameters obtained from the isothermal study can accurately predict the conversion during the non-isothermal operation as well.

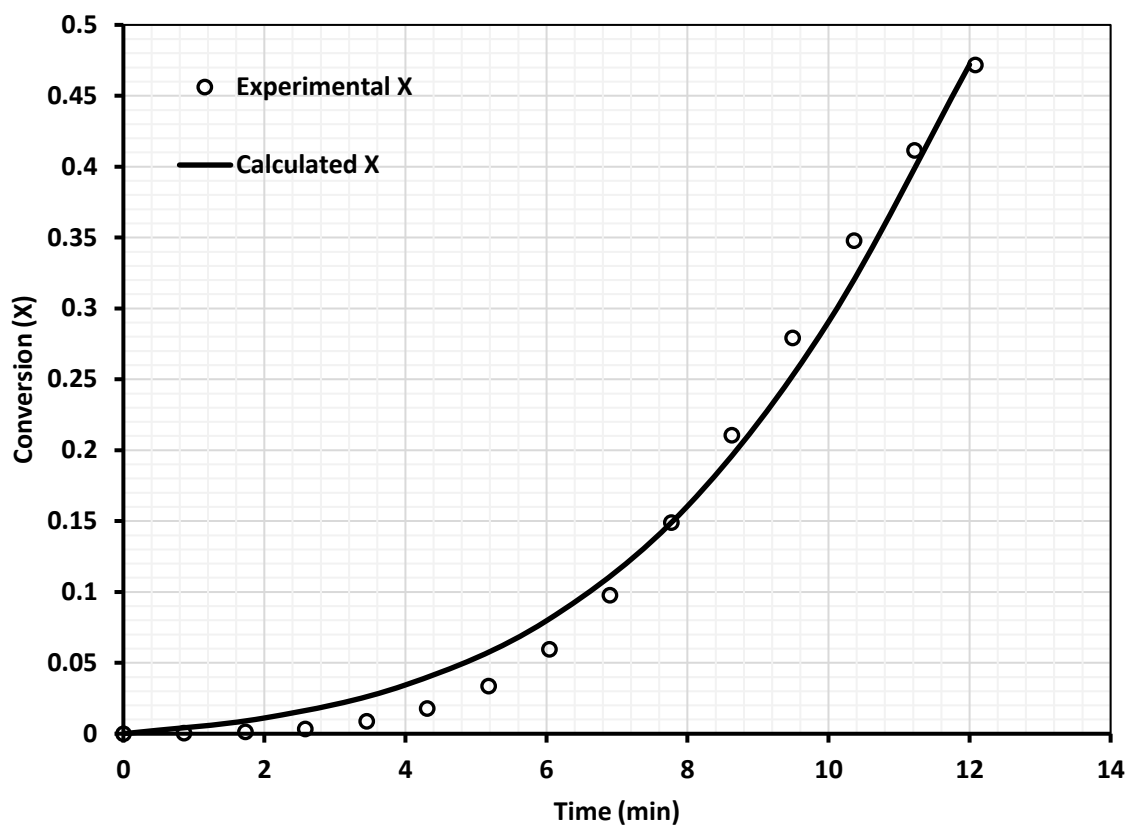


Figure 3.8 Comparison of non-isothermal derived equation with experimental data

### 3.3.3 Kinetic of Decomposition of $\text{Ca(OH)}_2$ in Composite $\text{Ca(OH)}_2:\text{CaTiO}_3$ Pellets

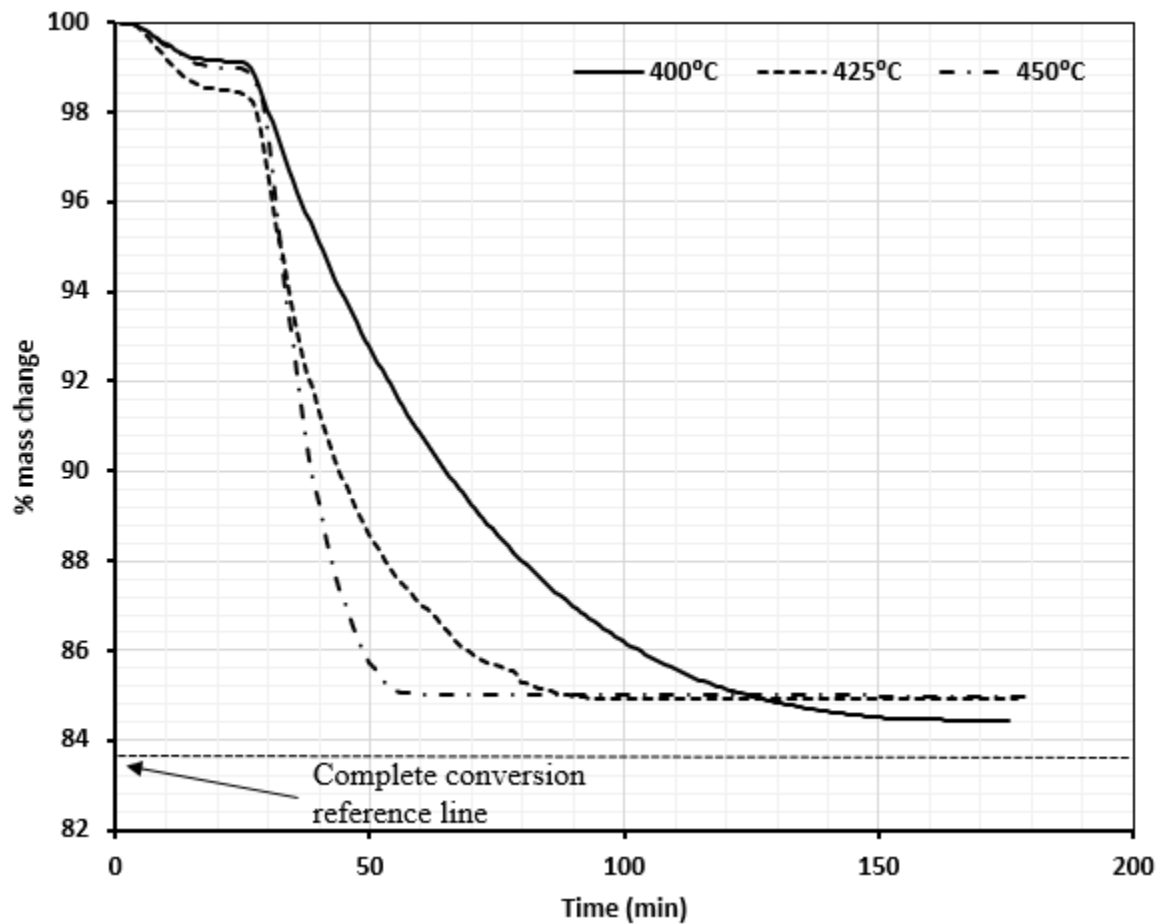


Figure 3.9 Percentage mass loss vs time at different maximum temperatures for 1:0.5  $\text{Ca(OH)}_2:\text{CaTiO}_3$  composite pellet: a) 400°C; b) 425°C; c) 450°C

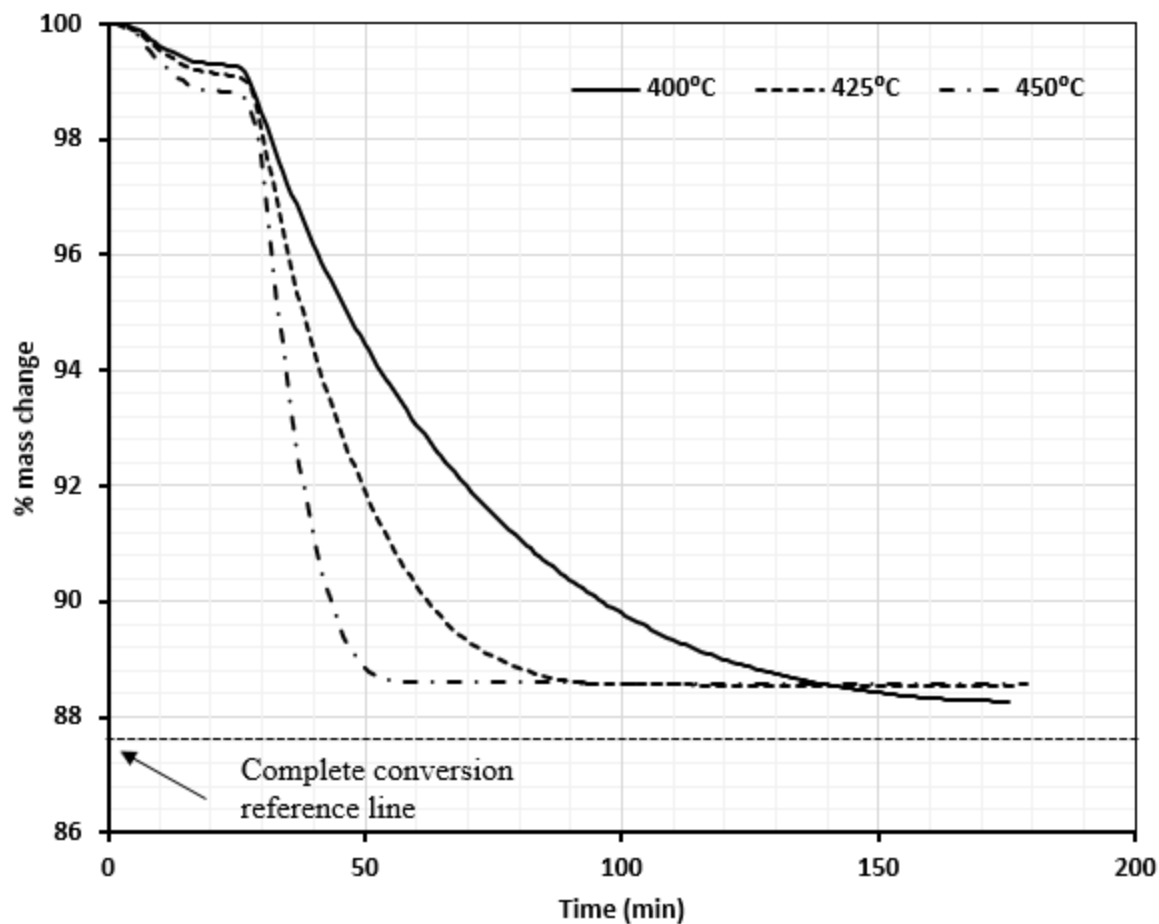


Figure 3.10 Percentage mass loss vs time at different maximum temperatures for 1:1 Ca(OH)<sub>2</sub>:CaTiO<sub>3</sub> composite pellet: a) 400°C; b) 425°C; c) 450°C

The kinetics of decomposition in the composite pellets with compositions of 1:0.5 and 1:1 Ca(OH)<sub>2</sub>:CaTiO<sub>3</sub> was also studied using the TGA instrument as shown in Figs 3.9 and 3.10. Figs. 3.11, 3.12 and 3.13 show the conversion plots with respect to time for pure Ca(OH)<sub>2</sub>, 1:0.5 and 1:1 Ca(OH)<sub>2</sub>:CaTiO<sub>3</sub> at 400, 425 and 450°C, respectively. It can be observed from these figures that the decomposition of Ca(OH)<sub>2</sub> to CaO is faster for the composite pellets than for pure Ca(OH)<sub>2</sub>. Table 4 shows the time required to reach 85% conversion for Ca(OH)<sub>2</sub> and composite pellets of different compositions. The conversion for composite pellets was much compared to Ca(OH)<sub>2</sub> at maximum temperature of 400°C. The difference in their respective times for 85% conversion was ~40 min. When the maximum temperature is increased, the difference in time between the pure Ca(OH)<sub>2</sub> pellets and Ca(OH)<sub>2</sub>-CaTiO<sub>3</sub> composite pellets for 85% conversion is reduced to 29 min at 425°C and ~12-15 min at 450°C as shown in Table

3.4. As the maximum temperature increases, significant conversion takes place during the non-isothermal stage. From the above results, it can also be clearly seen that  $\text{CaTiO}_3\text{-Ca(OH)}_2$  composite pellets exhibit higher decomposition rates compared to pure  $\text{Ca(OH)}_2$  pellets. One of the possible reasons is that  $\text{CaTiO}_3$  increases the surface area available for the reaction which effectively increases the rate of reaction.

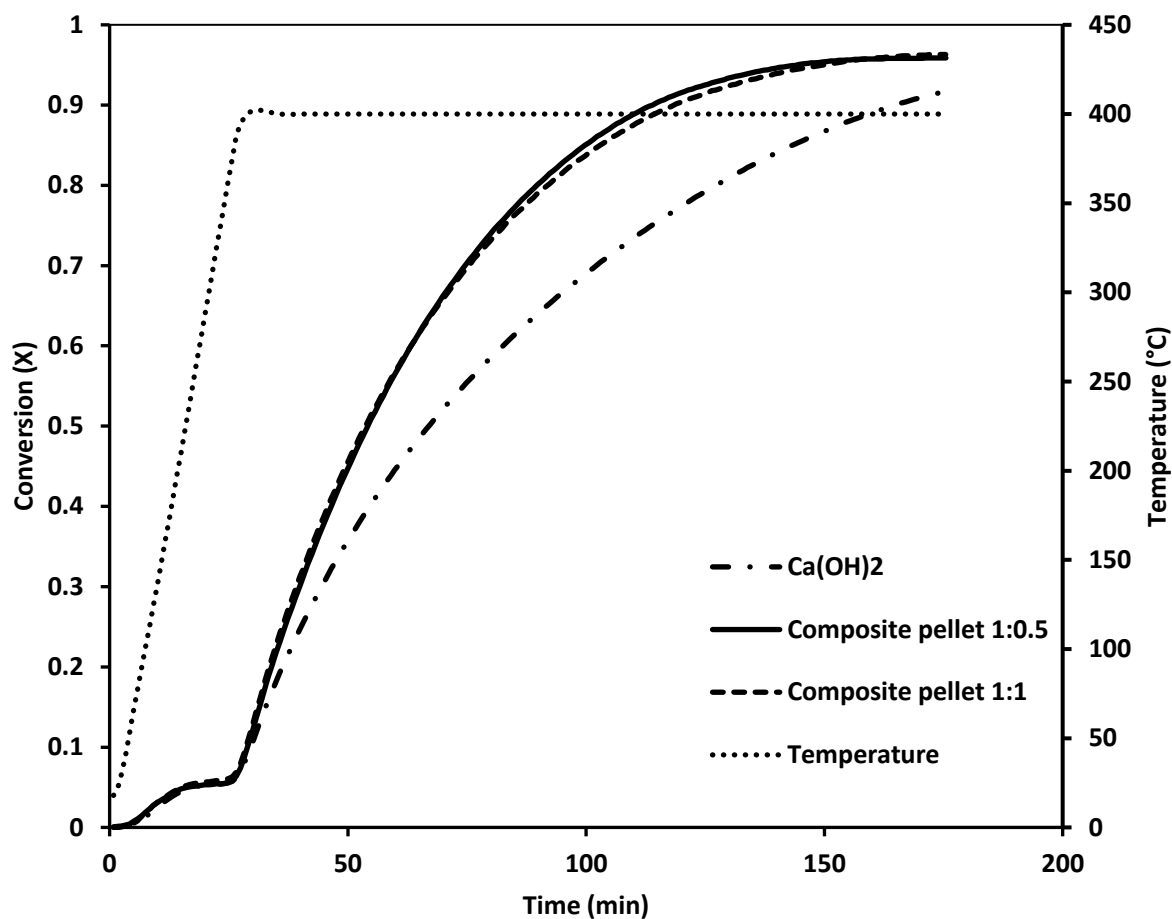


Figure 3.11 Conversion of inert modified  $\text{Ca(OH)}_2$  pellet at maximum temperature of  $400^\circ\text{C}$

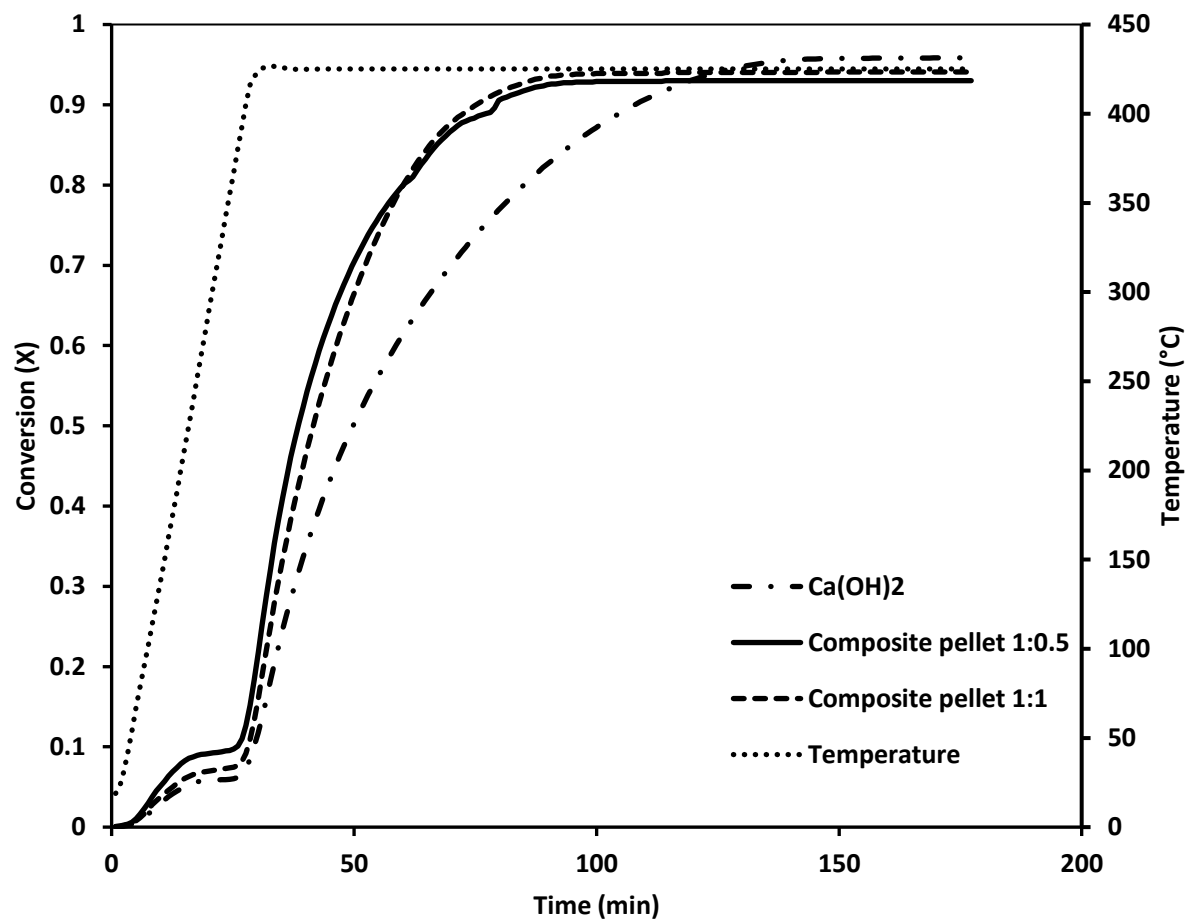


Figure 3.12 Conversion of inert modified  $\text{Ca(OH)}_2$  pellet at maximum temperature of  $425^\circ\text{C}$

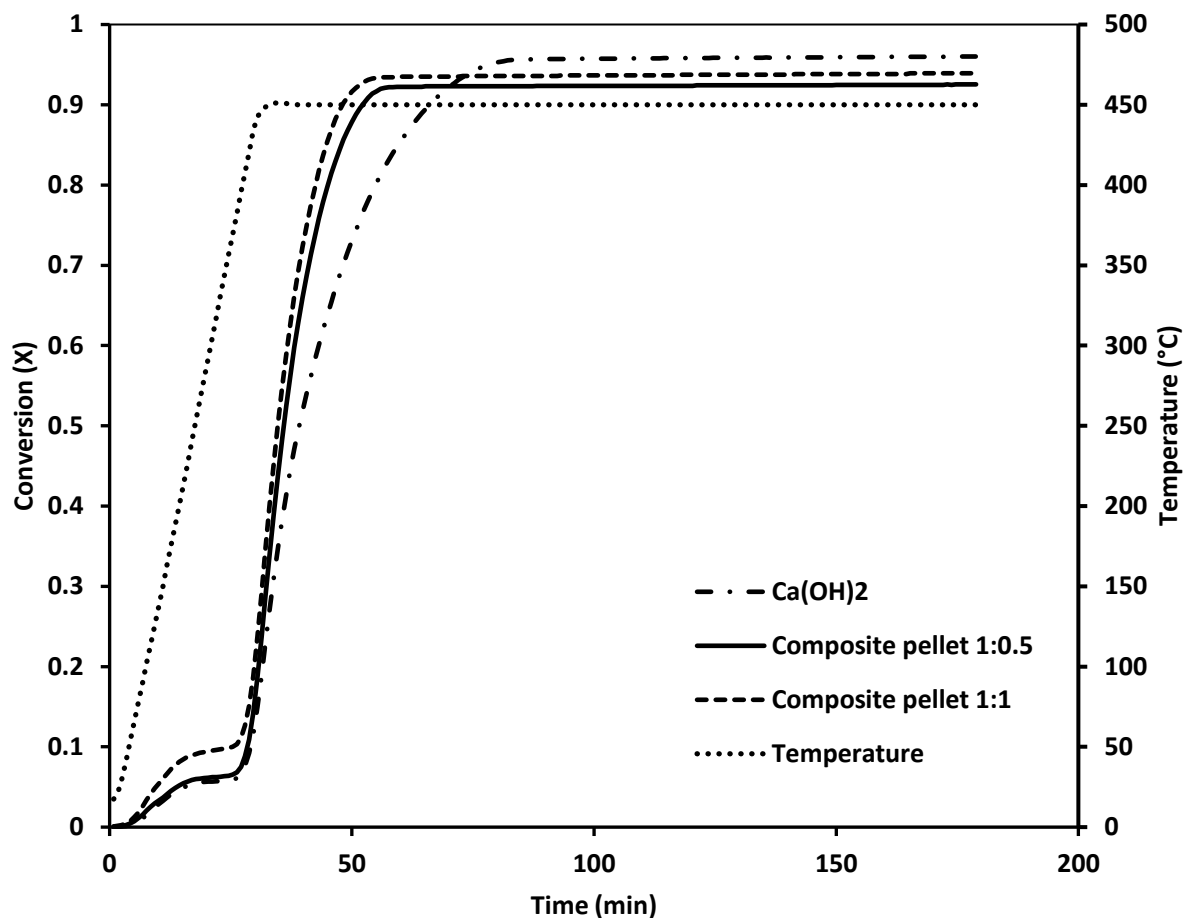


Figure 3.13 Conversion of inert modified  $\text{Ca(OH)}_2$  pellet at maximum temperature of  $450^\circ\text{C}$

Table 3.4 Comparison of time required to achieve respective conversion at different maximum temperature

Maximum Temperature ( $^\circ\text{C}$ )	Time taken for 85% conversion (min)		
	$\text{Ca(OH)}_2$	1:0.5 $\text{Ca(OH)}_2:\text{CaTiO}_3$	1:1 $\text{Ca(OH)}_2:\text{CaTiO}_3$
400	143	103	102
425	94	65	65
450	60	48	45

The X-Ray Diffraction (XRD) analysis shown in Fig. 3.14 is of 1:1 composite pellet before and after decomposition at  $450^\circ\text{C}$  with a conversion of 93.5% providing the qualitative information about the crystalline phases present in the composite pellet after and before decomposition. No new crystalline phases are detected, and all original crystalline phases are present showing the stability of the composite pellet. The CaO peaks intensity increased after

the decomposition, but presence of  $\text{Ca(OH)}_2$  also verify that the pellet did not achieve full conversion. The XRD results also showed that the presence of  $\text{CaTiO}_3$  acts as inert which does not react with  $\text{Ca(OH)}_2$  under the operating conditions which was also confirmed by Sakurai et al. [9].

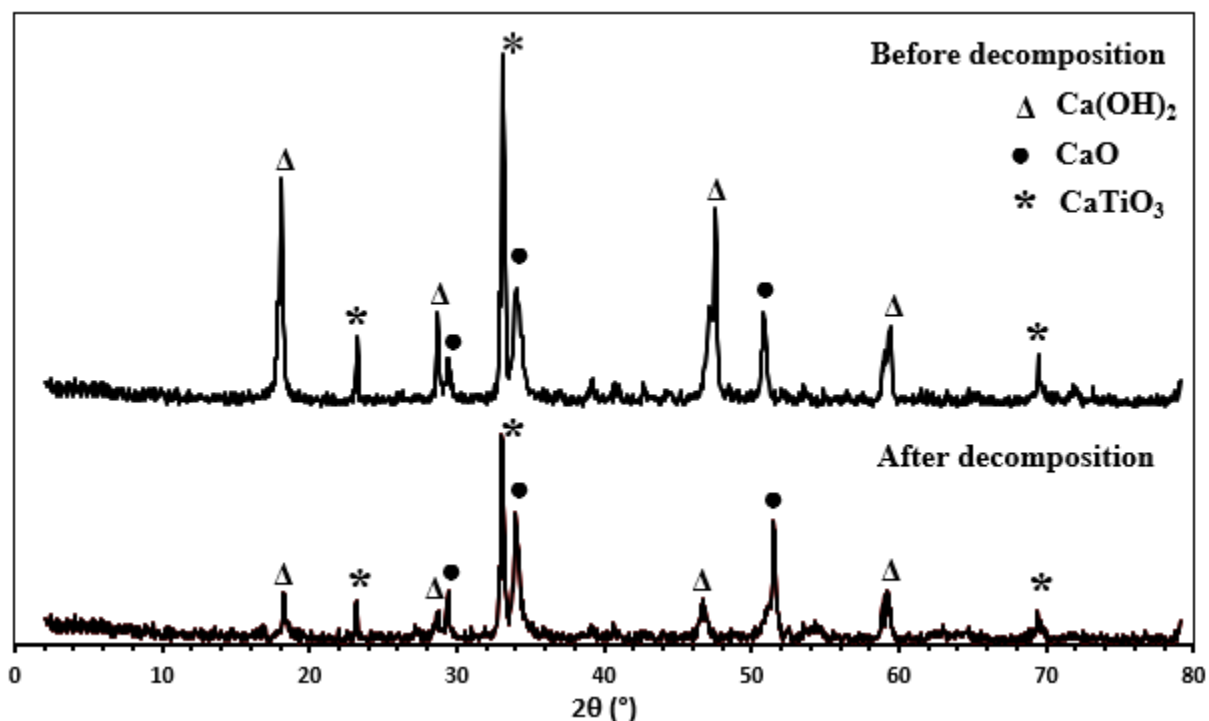


Figure 3.14 XRD diffraction patterns of composite pellet before and after decomposition

The kinetic parameters were estimated using similar approach as mentioned for kinetic analysis of pure  $\text{Ca(OH)}_2$ . Plotting the mechanism function  $\ln(1-X)$  vs  $t$  results in straight lines, with the slope of the line providing an estimate of the rate constant ( $k$ ). The mechanism function  $\ln(1-X)$  is used as it is assumed to be first order reaction and it is verified by the correlation coefficient of the fitted linear regression line. Fig 3.15 shows the linear regression results at temperatures of  $400^\circ\text{C}$ ,  $425^\circ\text{C}$  and  $450^\circ\text{C}$ , respectively for 1:0.5  $\text{Ca(OH)}_2$ : $\text{CaTiO}_3$ . Fig. 3.16 shows the regression results for temperatures of  $400^\circ\text{C}$ ,  $425^\circ\text{C}$  and  $450^\circ\text{C}$ , respectively for 1:1  $\text{Ca(OH)}_2$ : $\text{CaTiO}_3$ . The rate constants obtained at different isothermal temperature for 1:0.5 and 1:1  $\text{Ca(OH)}_2$ : $\text{CaTiO}_3$  composition are shown in Table 3.5. Correlation coefficient values showed that the reaction is still first order when  $\text{CaTiO}_3$  is added with  $\text{Ca(OH)}_2$  for decomposition process.

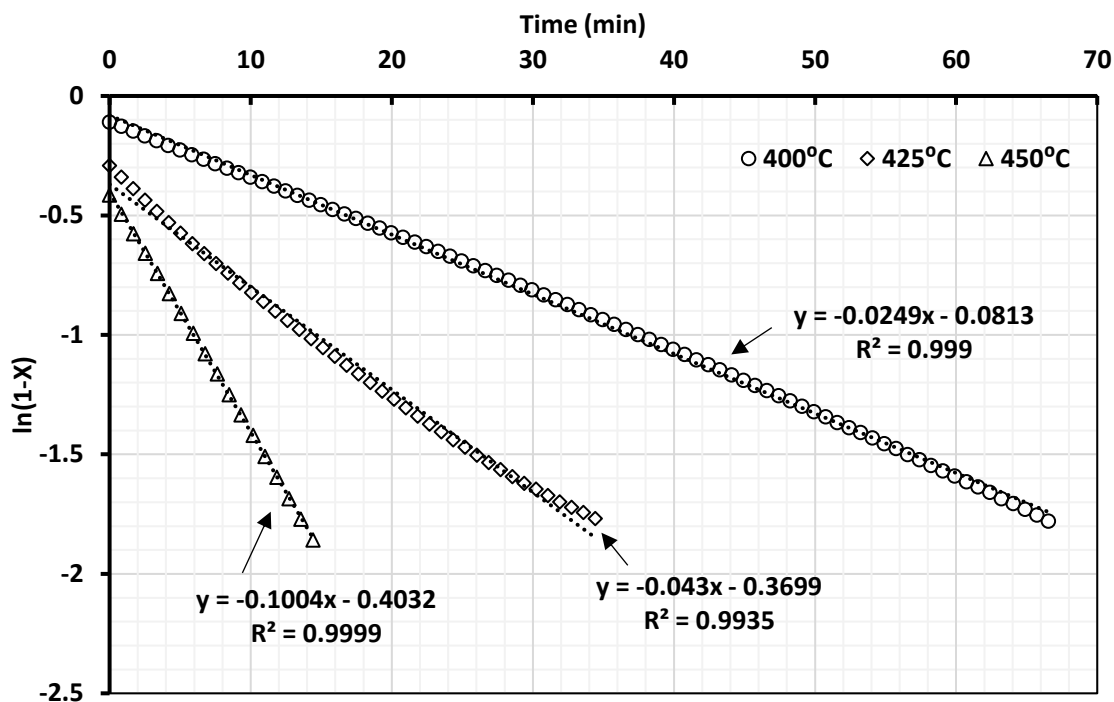


Figure 3.15 Linear regression results for rate constant estimation at 400°C, 425°C and 450°C isothermal temperatures for decomposition of 1:0.5  $\text{Ca}(\text{OH})_2:\text{CaTiO}_3$

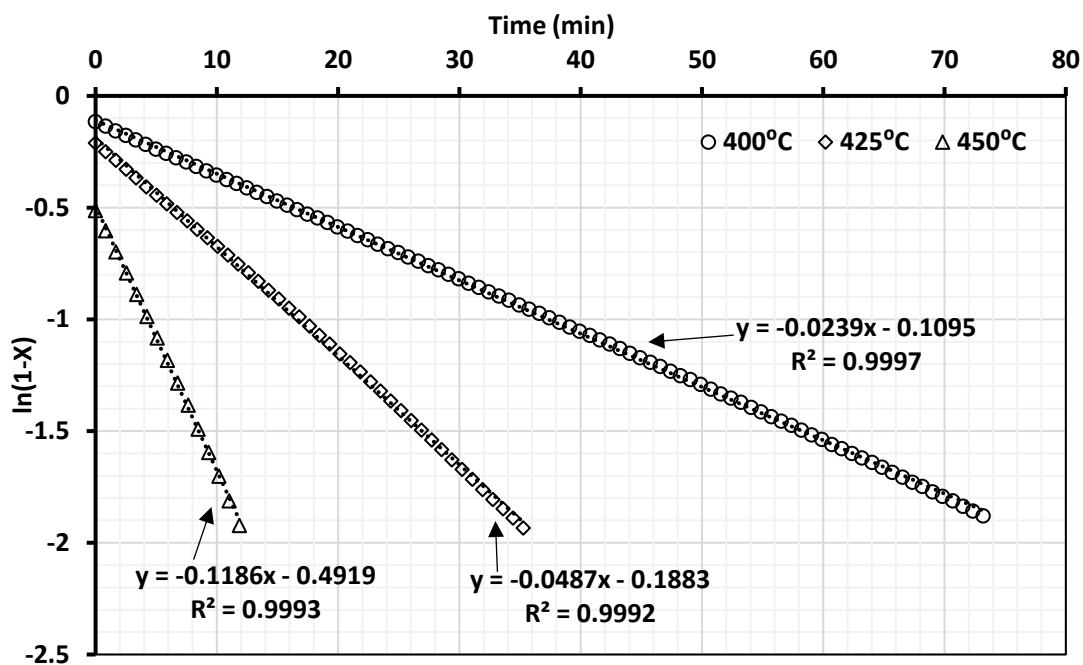


Figure 3.16 Linear regression results for rate constant estimation at 400°C, 425°C and 450°C isothermal temperatures for decomposition of 1:1  $\text{Ca}(\text{OH})_2:\text{CaTiO}_3$

Table 3.5 Rate constant for 1:0.5 and 1:1 Ca(OH)<sub>2</sub>:CaTiO<sub>3</sub> decomposition as a function of temperature

Isothermal temperature (°C)	1:0.5 Ca(OH) <sub>2</sub> :CaTiO <sub>3</sub>		1:1 Ca(OH) <sub>2</sub> :CaTiO <sub>3</sub>	
	Rate constant (k) (min <sup>-1</sup> )	Correlation coefficient (R <sup>2</sup> )	Rate constant (k) (min <sup>-1</sup> )	Correlation coefficient (R <sup>2</sup> )
400	0.0249	0.999	0.0239	0.9997
425	0.043	0.9935	0.0487	0.9992
450	0.1004	0.9999	0.1186	0.9993

The activation energy ( $E$ ) and Arrhenius constant ( $A$ ) for 1:0.5 and 1:1 Ca(OH)<sub>2</sub>:CaTiO<sub>3</sub> composition were estimated by plotting  $\ln(k)$  vs  $1/T$  as shown in Fig. 3.17. For 1:0.5 Ca(OH)<sub>2</sub>:CaTiO<sub>3</sub>, the slope of the line -13534 corresponds to  $-E/R$ , thus obtaining activation energy ( $E$ ) as 112.52 kJ/ mol. The constant obtained from linear regression fit 16.356 corresponds to  $\ln(A)$ . the error based on the linear regression value and TGA results for  $E$  is about 13.1% and for  $\ln(A)$  is 13.2%. For 1:1 Ca(OH)<sub>2</sub>:CaTiO<sub>3</sub>, the slope of the line -15568 corresponds to  $-E/R$ , yielding 129.43 kJ/mol as the activation energy ( $E$ ) and  $\ln(A)$  value is 19.356 which is estimated from the constant obtained from the linear regression. The error based on the linear regression value and TGA results for  $E$  is about 8.6% and for  $\ln(A)$  is 9.7%. It can be clearly observed from the obtained results that the addition of CaTiO<sub>3</sub> which acts as inert agent significantly increases the kinetic parameters – activation energy and Arrhenius constant – and consequently, the rate constant. When comparing 1:1 Ca(OH)<sub>2</sub>:CaTiO<sub>3</sub> to 1:0.5 Ca(OH)<sub>2</sub>:CaTiO<sub>3</sub>, the activation energy and  $\ln(A)$  are higher for the 1:1 mixture.

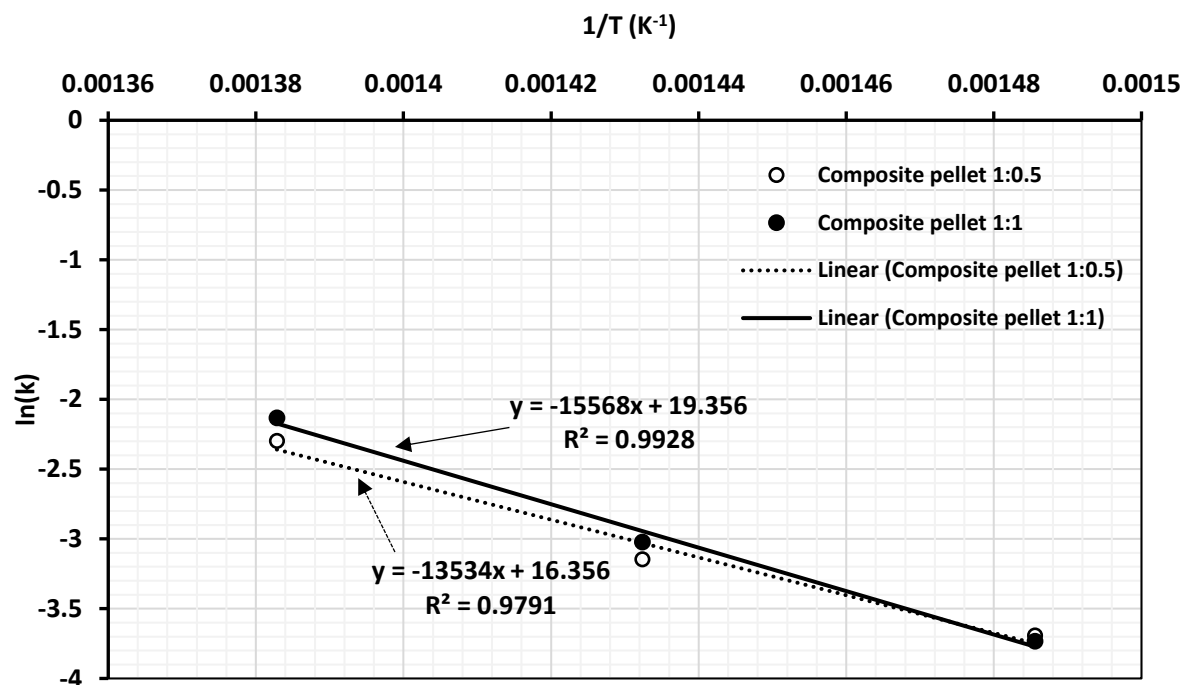


Figure 3.17 Linear regression curve between  $\ln(k)$  vs  $1/T$  for activation energy and Arrhenius constant estimation for decomposition of 1:0.5 and 1:1  $\text{Ca(OH)}_2:\text{CaTiO}_3$

### 3.3.4 Comparison of kinetic parameters for $\text{Ca(OH)}_2$ and composite pellet with reported data

Table 3.6 shows a comparison between the literature-reported rate parameters from non-isothermal kinetic studies and the parameters determined from isothermal experimentation in the present study.

Table 3.6 Comparison of kinetic parameters of pure  $\text{Ca(OH)}_2$  and composite pellet

Kinetic Parameters	Non-Isothermal (Long et. al [5])	Isothermal (This work)		
	$\text{Ca(OH)}_2$	$\text{Ca(OH)}_2$	1:0.5 $\text{Ca(OH)}_2:\text{CaTiO}_3$	1:1 $\text{Ca(OH)}_2:\text{CaTiO}_3$
$E$ (kJ/mol)	115-140	102.71	112.52	129.43
$\ln A$ ( $\text{min}^{-1}$ )	16-23	14.119	16.356	19.356

Minor discrepancy can be seen in the values of activation energy, but the natural logarithm of Arrhenius constant agrees well under non-isothermal and isothermal conditions for pure

$\text{Ca(OH)}_2$ . The study by Gorbachev and Logvineko [7] mathematically proved estimation of kinetic parameters must be determined from the results of the isothermal conditions of the decomposition processes. The other key reason for the discrepancy in activation energy is the transformation process for the same material which proceeds with different formal reaction order or mechanism function depending on the experimental conditions. The higher the reaction's formal order, the higher the activation energy's effective value [6]. Secondary explanation for the discrepancy in kinetic parameters is that there is a temperature gradient present within the sample during non-isothermal conditions, which can lead to the uncertainty associated with actual reaction temperature. Under isothermal condition, the kinetic parameters increases significantly when composite pellets are used compared to pure  $\text{Ca(OH)}_2$  as addition of  $\text{CaTiO}_3$  with  $\text{Ca(OH)}_2$  acts as scaffolding helping structural integrity, but it also increases the reaction surface area which directly helps in increasing the rate of the decomposition reaction.

### 3.3.5 Structure and Mechanical Compressive Strength Analysis



Figure 3.18 Pellet after the first decomposition of  $\text{Ca(OH)}_2$ : (a) pure  $\text{Ca(OH)}_2$ , (b) composite pellet

Pure  $\text{Ca(OH)}_2$  pellet after the decomposition developed some cracks but no cracks were observed on the composite pellet surface, as shown in Fig. 3.18 (a) and (b), respectively. It can be observed that composite pellet modified with  $\text{CaTiO}_3$  affects the kinetics of dehydration-hydration reaction significantly, but it decreases the quantity of reactant present in the pellet of same size. So, while designing the chemical reactor for  $\text{Ca(OH)}_2/\text{CaO}$  reaction, we need to account for this decrease in reactant quantity because of addition of inert agent. Table 3.7 shows the compressive strength (Satec T5000) of  $\text{Ca(OH)}_2$  and composite pellets before decomposition and results showed that addition of  $\text{CaTiO}_3$  increases the mechanical strength of the pellets by >55%.

Table 3.7 Compressive strength of  $\text{Ca}(\text{OH})_2$  and composite pellets before decomposition

Sample	Compressive strength ( $\text{kg}/\text{cm}^2$ )
Pure $\text{Ca}(\text{OH})_2$ pellet	104.1
Composite pellet (1:0.5)	161.8
Composite pellet (1:1)	168.7

## Nomenclature

### *Latin symbols*

$A$  Arrhenius constant, ( $\text{min}^{-1}$ )

$E$  Activation energy, ( $\text{J mol}^{-1}$ )

$k$  Rate constant, ( $\text{min}^{-1}$ )

$m$  Mass of pellet, (g)

$M$  Molecular mass, ( $\text{g mol}^{-1}$ )

$R$  Gas constant, ( $\text{J mol}^{-1} \text{K}^{-1}$ )

$t$  Time, (min)

$T$  Temperature, (K)

$u$  Error, (percentage)

$X$  Conversion, (dimensionless)

### *subscript*

$\text{Ca}(\text{OH})_2$  Calcium hydroxide

$CaO$	Calcium oxide
$f$	Final
$i$	Initial
$\ln A$	Natural logarithm of Arrhenius constant
$s$	System
$t$	Time

## References

1. D. Chen, X. Gao, D. Dollimore. 1993. "The application of non-isothermal methods of kinetic analysis to the decomposition of calcium hydroxide." *Thermochimica Acta* 215:65–82. [https://doi.org/10.1016/0040-6031\(93\)80082-L](https://doi.org/10.1016/0040-6031(93)80082-L).
2. S. Dutta, T. Shirai. 1974. "Kinetics of drying and decomposition of calcium hydroxide." *Chemical Engineering Science* 29:2000–2003. [https://doi.org/10.1016/0009-2509\(74\)85021-9](https://doi.org/10.1016/0009-2509(74)85021-9).
3. A. Irabien, J. R. Viguri, I. Ortiz. 1990. "Thermal dehydration of calcium hydroxide. 1. Kinetic model and parameters." *Industrial and Engineering Chemistry Research* 29:1599–1606. <https://doi.org/10.1021/ie00104a004>.
4. R. S. Mikhail, S. Brunauer, L.E. Copeland. 1966. "Kinetics of the thermal decomposition of calcium hydroxide." *Journal of Colloid and Interface Science* 21:394–404. [https://doi.org/10.1016/0095-8522\(66\)90005-5](https://doi.org/10.1016/0095-8522(66)90005-5).
5. X. F. Long, L. Dai, B. Lou, J. Wu. 2017. "The kinetics research of thermochemical energy storage system  $\text{Ca}(\text{OH})_2/\text{CaO}$ ." *International Journal of Energy Research* 41:1004–1013. <https://doi.org/10.1002/er.3688>.
6. J. R. Maccallum, J. Tanner. 1970. "Derivation of Rate Equations used in Thermogravimetry." *Nature* 225:1127–1128. <https://doi.org/10.1038/2251127b0>.
7. V. M. Gorbachev, V.A. Logvinenko. 2005. "The correlation between isothermal and non-isothermal kinetics in thermogravimetry." *Journal of Thermal Analysis and Calorimetry* 4: 475–477. <https://doi.org/10.1007/bf01913805>.
8. C. Huang, M. Xu, X. Huai. 2019. "Experimental investigation on thermodynamic and kinetic of calcium hydroxide dehydration with hexagonal boron nitride doping for thermochemical energy storage." *Chemical Engineering Science* 206:518-526 <https://doi.org/10.1016/J.CES.2019.06.002>.
9. M. Sakurai, N. Miyake, A. Tsutsumi, K. Yoshida. 1996. "Analysis of a reaction mechanism in the UT-3 thermochemical hydrogen production cycle." *International Journal of Hydrogen Energy* 21:871–875. [https://doi.org/10.1016/0360-3199\(96\)00029-8](https://doi.org/10.1016/0360-3199(96)00029-8).

## Chapter 4 Cyclability Study of Ca(OH)<sub>2</sub>/CaO Dehydration-Hydration Reaction at Bench-Scale

### 4.1 Objective

This chapter reports upon Ca(OH)<sub>2</sub>/CaO ChHP studies conducted at using both differential thermal analysis (DTA, consisting of thermogravimetry and differential scanning calorimetry), and a bench scale laboratory setup consisting of a chemical reactor system was designed to study the dehydration of Ca(OH)<sub>2</sub> at different decomposition temperatures and hydration of CaO under repeated cycles. Both the DTA and bench-scale experiments were conducted using pellets of Ca(OH)<sub>2</sub>/CaO. Repeated dehydration-hydration cycles of Ca(OH)<sub>2</sub>/CaO reaction were conducted in the bench-scale system to study the effect of the reaction temperature on the conversion, gross-energy and exergy flows. *Energy and exergy efficiencies were determined incorporating the effects of temperatures on thermodynamic properties for increased accuracy.* Structural morphology changes associated with the repeated cycles were also examined. Preliminary sets of experiments were performed with pure Ca(OH)<sub>2</sub> pellets for six repeated cycles. Final sets up experiments were preformed using composite pellets (1:0.5 Ca(OH)<sub>2</sub>:CaTiO<sub>3</sub> by wt%) for twenty repeated cycles. Compressive strength of the composite pellets after every cycle was also reported.

### 4.2 Experimental Investigation

Experimental setups and procedures for DTA and bench-scale systems are discussed under sections 4.2.1 and 4.2.2, respectively.

#### 4.2.1 Experimental Setup

The DTA experiments were conducted using a thermogravimetric analyzer-differential scanning calorimetric (TGA-DSC) thermal analyzer, while the bench-scale experiments were conducted in a custom chemical reactor. The capacities of the two setups are ~100 mg and ~300 g (of Ca(OH)<sub>2</sub>), respectively.

##### 4.2.1.1 TGA-DSC Instrument

The TGA-DSC experiments were performed in a Netzsch thermal analyzer (Netzsch TGA-DSC STA 409 PC), shown in Fig. 4.1. The Netzsch device is mainly composed of thermocouple, a reactor, a heating element, a sample carrier, and a cooling pipe. A calcium

hydroxide sample pellet is loaded into the alumina crucible and subjected to temperature program as described in section 4.2.2.1.



Figure 4.1 Netzsch TGA-DSC instrument

#### 4.2.1.2 Laboratory Bench-Scale Chemical Reactor

A schematic of the bench-scale experimental setup is shown in Fig. 4.2. It consists of a 2.5” diameter x 9” height SS 304 chemical reactor connected through a high temperature valve to a 4.4” diameter x 8” height aluminum vessel that functioned as both a condenser (during dehydration) and an evaporator (during hydration). Both the vessels had provision for electrical heating through band heaters (350W and 700W). The aluminum vessel also had a provision for cooling through an internal copper cooling coil which was connected to a refrigerated bath circulating water at sub-ambient temperature (5–10°C). A vacuum pump connected to the condenser/evaporator vessel used to manipulate the reaction pressure for sub-ambient operation. A high temperature valve allowed isolation of the reactor from the evaporator/condenser. Both the vessels were placed on electronic weighing scales (Uline Easy Count scale,  $60 \pm 0.002$  lbm/ $28000 \pm 1$  g) to measure mass gain/loss in them. Thermocouples (K-type, 12 in.,  $-226$ – $926^\circ\text{C}$ ) were installed in both vessels for temperature measurements, measuring the center temperature and inserted 3/4th of the vessel height from the top. Fig. 4.3 shows a photo of the experimental set up, without the insulation that covered the vessels and the piping during experimental runs.  $\text{Ca}(\text{OH})_2$  (J.T. Baker Chemicals, 97% purity, d50 =

5.5 $\mu\text{m}$ ) was formed into 8 mm diameter x 7 mm height pellets using pellet press (TPD 0 Desktop tablet press), and packed into the reactor for dehydration experiments.

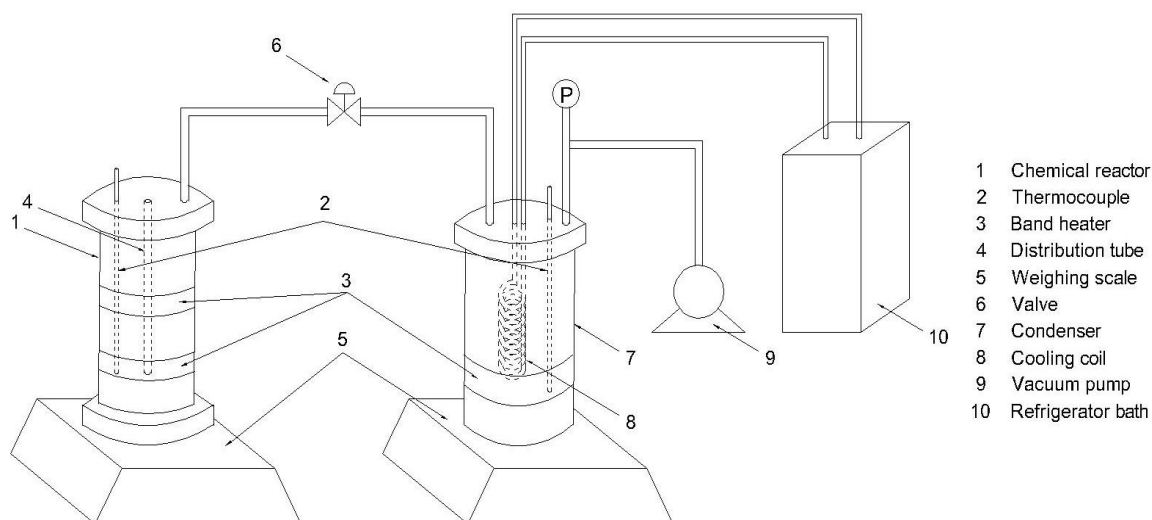


Figure 4.2 Schematic of the experimental setup



Figure 4.3 Lab scale experimental setup (left side: chemical reactor; right side: condenser/evaporator)

#### 4.2.2 Experimental Procedure

The experimental procedures for the TGA-DSC and bench-scale dehydration-hydration experiments are described in sections 4.2.2.1 and 4.2.2.2, respectively.

#### 4.2.2.1 TGA-DSC Analysis

In this experiment, a pellet of  $\text{Ca(OH)}_2$  with a mass of  $70 \pm 2$  mg and dimension 8 mm diameter x 7 mm height is placed in the alumina crucible, which in turn is placed in the sample chamber of the instrument. The experiment consists of raising the sample temperature from ambient conditions ( $\sim 20^\circ\text{C}$ ) at a specified heating rate (3 K/min - 10 K/min) to a final temperature of  $650^\circ\text{C}$ . Sample mass loss and calorimetric data are acquired and recorded automatically by the instrument.

#### 4.2.2.2 Bench-Scale Chemical Reactor

The  $\text{Ca(OH)}_2/\text{CaO}$  reactions takes place in two steps: (i) dehydration process, which is an energy charging step, and (ii) hydration process, which is an energy discharging step. The pellet density of  $\text{Ca(OH)}_2$  was  $1.36 \text{ g/cm}^3$  and the pellets were 62% dense as to keep water vapor transport in and out during the dehydration-hydration processes. The bulk packed density of the chemical bed was  $0.6 \text{ g/cm}^3$  and packed fraction of the chemical bed  $\sim 55\%$ . The detailed operating procedures are described below:

##### *Dehydration/Charging Process*

Approximately  $285 \pm 5$  g of  $\text{Ca(OH)}_2$  pellets are placed in the chemical reactor, and air is evacuated from the chemical reactor using the vacuum pump to achieve a pressure less than 1 torr. After evacuation, the valve between the reactor and the condenser is closed. Water is injected into the condenser, and the refrigerator bath is switched on, with the water bath temperature maintained at  $20^\circ\text{C}$  to maintain the pressure of 2.4 kPa in the condenser. Then the band heater on the chemical reactor is started and, once the chemical reactor temperature reaches  $200^\circ\text{C}$ , the valve is reopened and the chemical reactor is further heated to  $400\text{--}550^\circ\text{C}$ . Dehydration is carried out at a pressure of 2.4 kPa, corresponding to the water-bath temperature. Once the decomposition starts, the water vapor generated in the reactor flows into and is condensed within the condenser. The overall dehydration time varies from 180–200 min and the reaction are assumed to be complete when there is no change in the mass recorded as a function of time in the chemical bed. Two weighing balances - one on the chemical reactor side and other on condenser side, are used to verify that the amount of water vapor leaving the chemical reactor equals to the amount of water vapor condensed in the condenser. The loss of mass in chemical bed was observed to be equal to the gain in mass of water in condenser during

dehydration and vice versa during hydration process. No scattering of values was observed in the balance readings due to vibration or any thermal expansion effects.

#### *Hydration/Discharging Process*

In the hydration process, the chemical reactor bed contains CaO and the entire system is evacuated using the vacuum pump, following which the high temperature valve is closed. Water is injected in the evaporator, and the band heater on evaporator switched on. The evaporator is heated to 150°C. The hydration-process pressure is equivalent to the saturated vapor pressure of steam at 150°C, which is around 470 kPa ( $\approx$  68 psi). To maintain stable pressure of 470 kPa, evaporator temperature was kept constant at 150°C. The chemical reactor's side-band heater is also started, and the temperature inside the chemical reactor is brought up to 155–160°C (to avoid condensation of steam in the chemical reactor). Once the temperature inside the chemical reactor is stable, the high temperature valve is opened and the water vapor from the evaporator is introduced into the chemical reactor. Exothermic hydration reaction occurs between the water vapor and CaO pellets, as indicated by the increase in the reaction temperature and the hydration time varies from 170-200 min.

#### **4.2.3 Experimental Data Analysis**

In thermal charging and discharging, the chemical-bed mass is continuously changing with release or absorption of water vapor in the bed. The mole fraction  $x(t)$  of the reactant Ca(OH)<sub>2</sub> is calculated by Eq. 4.1 [1]:

$$x(t) = \frac{\frac{m(t)}{w_i} \frac{M_{CaO}}{M_{Ca(OH)_2}}}{1 - \frac{M_{CaO}}{M_{Ca(OH)_2}}} \quad (4.1)$$

where  $m(t)$  is the mass of the chemical bed during the reaction in grams,  $w_i$  is the initial mass of Ca(OH)<sub>2</sub> in grams,  $M_{Ca(OH)_2}$  and  $M_{CaO}$  are mole mass of calcium hydroxide and calcium oxide respectively in grams per mole.

Thermal energy input, output of the charging and discharging steps and energy efficiency can be calculated using the Eqs. 4.2, 4.3 and 4.4, respectively [2,3].

$$q_i = \frac{1}{M_{Ca(OH)_2}} \cdot (\Delta H_r(1 - x_d) + Q_s) \quad (4.2)$$

$$q_o = \frac{1}{M_{Ca(OH)_2}} \cdot (\Delta H_r(x_h - x_{d,end}) + Q_{cond}) \quad (4.3)$$

$$\eta_{er} = \frac{q_o}{q_i} \quad (4.4)$$

Exergy availability and output exergy of the system, and the exergy efficiency can be calculated using the Eqs. 4.5, 4.6 and 4.7, respectively. Exergy is a useful quantity that stems from the second law of thermodynamics and reflects the quality of energy [4].

$$E_{X,av} = \frac{1}{M_{Ca(OH)_2}} \cdot [\Delta H_r(1 - x_d) \left(1 - \frac{T_a}{T_r}\right) + Q_s \left(1 - \frac{T_a}{T_s}\right)] \quad (4.5)$$

$$E_{X,out} = \frac{1}{M_{Ca(OH)_2}} \cdot [\Delta H_r(x_h - x_{d,end}) \left(1 - \frac{T_a}{T_r}\right) + Q_{cond} \left(1 - \frac{T_a}{T_s}\right)] \quad (4.6)$$

$$\eta_{ex} = \frac{E_{x,o}}{E_{X,av}} = \frac{E_{X,av} - E_{X,l}}{E_{X,av}} \quad (4.7)$$

where  $q_i$  is the amount the thermal energy input per unit mass of  $Ca(OH)_2$ , kJ/kg;  $q_o$  is the gross heat output per unit mass of  $Ca(OH)_2$ , kJ/kg;  $\Delta H_r$  is calculated molar enthalpy of reaction kJ/mol;  $x_d$  is the mole fraction of reactant during dehydration process;  $Q_s$  is the sensible heat required to heat the chemical reactor and evaporator kJ/mol;  $x_h$  is the mole fraction of the reactant during the hydration process; and  $x_{d,end}$  is the reacted fraction of the previous dehydration process;  $Q_{cond}$  heat of condensation of the water vapor kJ/mol;  $E_{x,av}$  is the exergy available kJ/kg;  $E_{x,o}$  is the exergy output kJ/kg;  $T_a$  is the ambient or reference temperature;  $T_r$  and  $T_s$  are the reaction temperatures and sensible heating temperatures, respectively;  $\eta_{er}$  is the energy efficiency and  $\eta_{ex}$  is the exergetic efficiency.

### 4.3 Results and Discussion

#### 4.3.1 Thermal Gravimetric Analysis

TGA-DSC curves are shown in Figs. 4.4 and 4.5 for experiment conducted at the heating rates of 3, 5, 10, 15 and 20 K/min, respectively. The Fig. 4.4 shows the mass loss in thermogravimetric measurements with respect to the temperature profile at different heating rates, while the Fig. 4.5 shows the heat effects in calorimetric analysis with respect to temperature profile at different heating rates. Three distinct regions and mechanisms of mass loss can be identified from the thermogravimetric curves: (i) Mass loss  $m_1$  attributable to the

removal of unbound or absorbed moisture, (ii) Mass loss  $m_2$  attributable to  $\text{Ca(OH)}_2$  decomposition - the first decomposition, and (iii) Mass loss  $m_3$  attributable to decomposition of  $\text{CaCO}_3$  present in small quantity as an impurity - the second decomposition. The mass loss curves indicate that most of the loss occurred in the temperature range 400-600°C depending upon the heating rates, concomitant with the peak of the DSC curve, and was associated with the dehydration reaction of  $\text{Ca(OH)}_2$ . The gradual mass loss at temperatures lower than 200-250°C could be associated with physical drying of the solid (loss of unbound moisture). The percentage mass change ( $m_1$ ) because of physical drying of the reactant was 1.5±0.75%. The percentage mass loss because of decomposition ( $m_2$ ) were 20.4-22.8% at heating rates ranges from 3-20 K/min as shown in Table 4.1. The theoretical mass loss for complete dehydration of  $\text{Ca(OH)}_2$  is 24.3%, indicating the extent of conversion was 90±5% in the five sets of experiments. The onset temperature for the decomposition reaction varied with increasing heating rates as onset temperatures were 400, 420, 430, 440 and 450°C for 3, 5, 10, 15 and 20 K/min respectively. The conversion plateaued at temperature 550, 560, 590, 610 and 630°C for heating rate of 3, 5, 10, 15 and 20 K/min respectively. The decomposition temperature was found to increase with increasing the heating rates. The percentage mass loss ( $m_3$ ) for second decomposition was between 1.25±0.5% because of  $\text{CaCO}_3$  present in  $\text{Ca(OH)}_2$  samples getting decomposed at higher temperatures.

The area under the curve in Fig. 4.5 gives the reaction enthalpy associated with the decomposition of  $\text{Ca(OH)}_2$ . The reaction enthalpies associated with heating rates 3, 5, 10, 15 and 20 K/min are 570.31, 596.8, 640, 630.3 and 581.8 J/g respectively. The highest conversion was obtained while operating under 10 K/min heating rate. The conversion between 5 K/min and 15 K/min were almost equal but 15 K/min had higher reaction enthalpy associated with it. It can be concluded from the above results that the optimum heating rate for the decomposition of  $\text{Ca(OH)}_2$  ranges from 10-15 K/min. The reaction enthalpy reported is lower than the standard reaction enthalpy at 25°C because as the temperature increases the reaction enthalpy decreases. The influence on the carbonation of  $\text{CaCO}_3$  was not significant in the conversion and reaction enthalpy determination as the  $\text{CaCO}_3$  content in  $\text{Ca(OH)}_2$  pellet was comparatively small, i.e., ~1.5% as per the analysis supplied by the vendor as also confirmed by TGA and DSC curves. The pellets were handled such that exposure to atmosphere was minimized to prevent any carbonation. The area under the DSC curve which is the indicator of

the reaction enthalpy was unaffected by decomposition of carbonate, which takes place at higher temperatures as reported by Sun et al. [35]. The enthalpy of decomposition of  $\text{Ca}(\text{OH})_2$  increased with increase in heating rate, but excessive heating rate can lead to inadequate reaction thus decreasing the reaction enthalpy. The TG curve progressively moved to high temperature region as heating rate increased. The results reported are consistent with the observations of Long et al. who used powdered samples weighing  $\sim 7$  mg and reported reaction enthalpy ranging from 650-780 kJ/kg [5].

Table 4.1 Percentage mass loss and reaction enthalpy of  $\text{Ca}(\text{OH})_2$  at different heating rate

Heating Rate (K/min)	% Mass Change ( $m_1$ )	% Mass Change ( $m_2$ )	% Mass Change ( $m_3$ )	Reaction Enthalpy (kJ/kg)
3	2.10	20.45	1.44	570.1
5	1.19	22.42	1.10	596.8
10	0.96	22.74	1.04	640
15	0.63	22.57	0.96	630.3
20	1.45	21.16	0.96	581.8

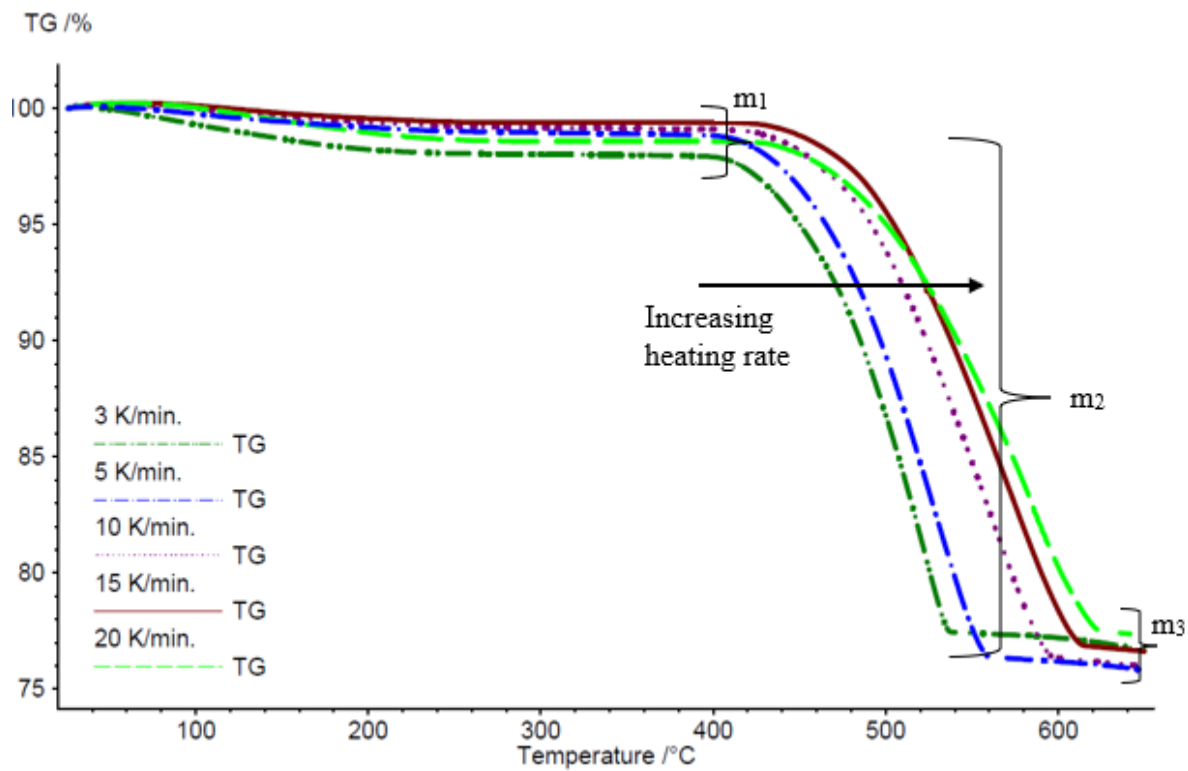


Figure 4.4 The TGA percentage mass loss vs temperature curve of Ca(OH)<sub>2</sub> decomposition at different heating rates

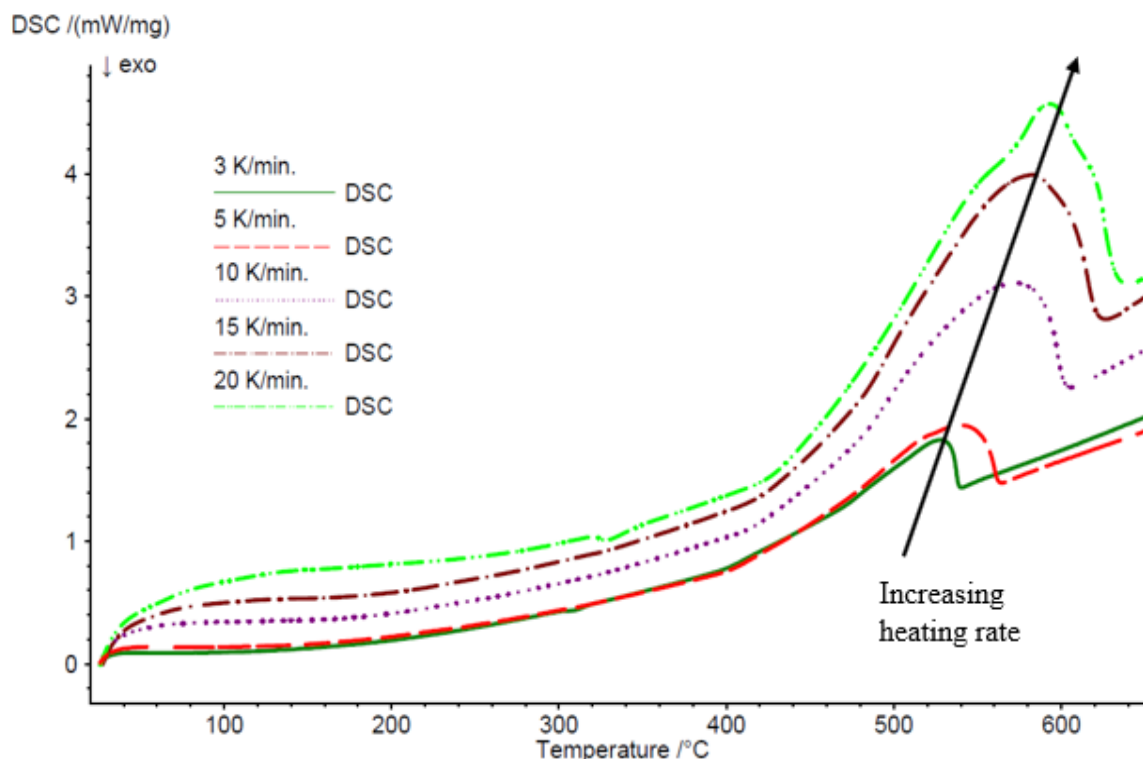


Figure 4.5 The DSC heat vs temperature curve of  $\text{Ca}(\text{OH})_2$  decomposition at different heating rates

### 4.3.2 Preliminary Experimental Results and Analysis of Pure $\text{Ca}(\text{OH})_2$ Pellets

#### 4.3.2.1 Dehydration/Charging Process

Dehydration of the  $\text{Ca}(\text{OH})_2$  charged into the reactor was accomplished by increasing the reactor temperature using electrical heating. Each dehydration was followed by the hydration reaction to reformulate the  $\text{Ca}(\text{OH})_2$  from the  $\text{CaO}$  formed at the end of the dehydration. Six dehydration-hydration cycles were conducted with the material charged initially in the reactor.

Fig. 4.6 shows the reactor center temperature and unreacted mole fraction of  $\text{Ca}(\text{OH})_2$  as a function of time for the six cycles. As mentioned above, the valve between the reactor and the condenser was kept closed at the beginning of each dehydration experiment. The valve was opened at around 45 min when the chemical reactor temperature was  $280^\circ\text{C}$  for all six cycles. The peak temperatures of Cycles 1 and 2 were  $540$  and  $535^\circ\text{C}$ , respectively. The peak temperature of the dehydration for this experiment depends upon when the heater was turned off. The peak temperatures of Cycles 3, 4, and 5 were  $475$ ,  $477$ , and  $480^\circ\text{C}$ , respectively. The peak temperature of Cycle 6 was  $570^\circ\text{C}$ , which was the highest among all temperatures. In the

initial 60 min, the reaction decomposition rate was slow at a temperature of 340°C, as shown in Fig. 4.6. Once the chemical reactor temperature reached 390°C, at around 70 min, dehydration rate started to surge gradually, and at temperatures higher than 410°C, the dehydration rates were quite high. In all six cycles, the majority of the decomposition took place between 70 and 125 min, and it can be observed that most of the conversion took place then. After 125 min, the decomposition rate was slow, and little change in the conversion can be seen in Fig. 4.6. The heater is turned off at 180 min when no significant change in the mass of the chemical bed was observed. The gradual decrease in the temperature curve in Fig. 4.6 between time intervals 60-120 min is due to the storage of thermal energy in chemical bonds via the endothermic reaction.

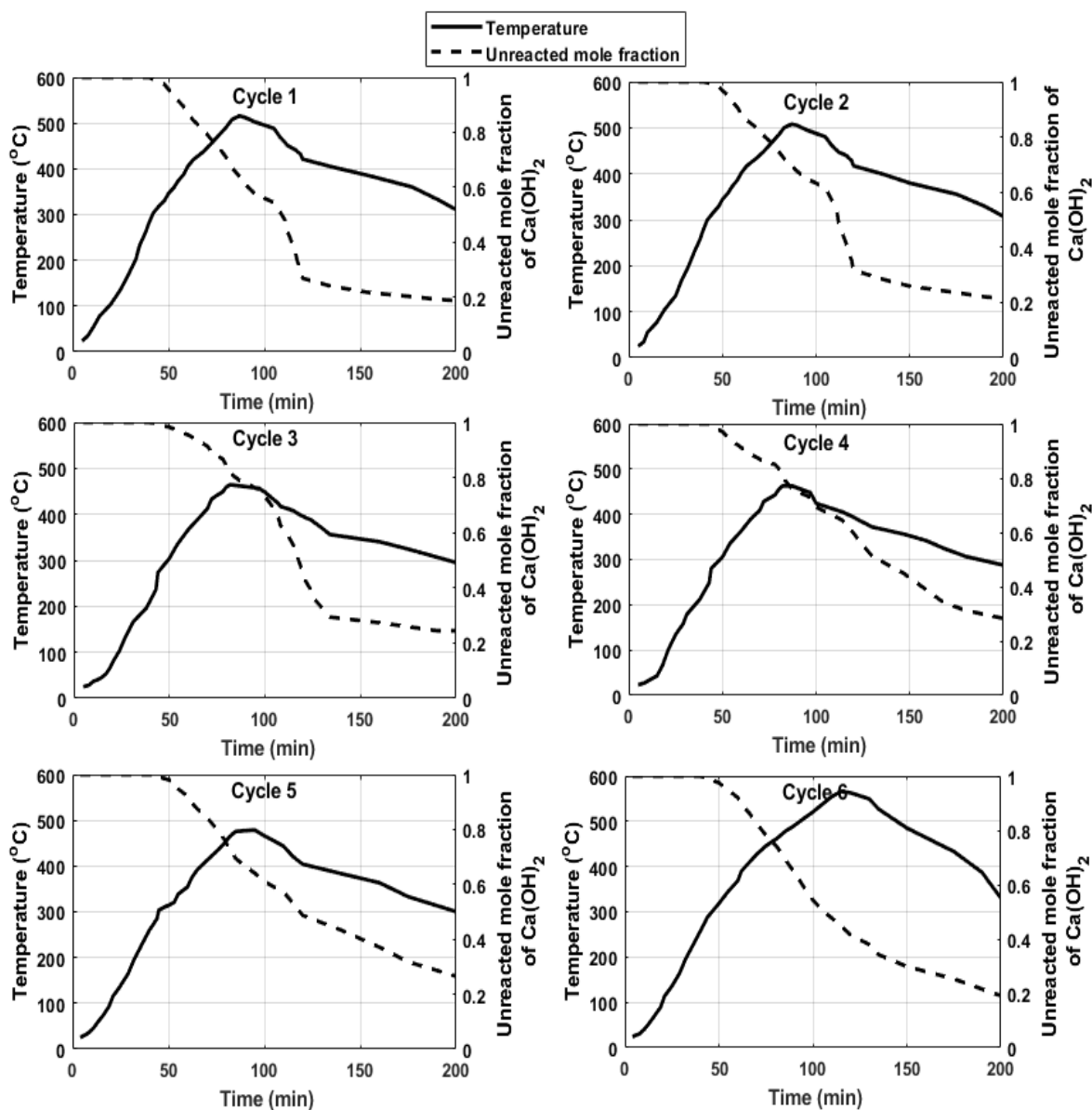


Figure 4.6 Chemical reactor center temperature and unreacted mole fraction vs time during dehydration reaction (Pressure  $\approx 2.4$  kPa)

In Cycle 1, the decomposition peak temperature was  $540^\circ\text{C}$ , and the unreacted mole fraction after 200 min decreased from 1 to 0.18. In Cycle 2, the decomposition peak temperature was  $535^\circ\text{C}$ , which was almost the same as Cycle 1, and the unreacted mole fraction after 200 min decreased to 0.21. In Cycles 3, 4 and 5, the decomposition peak temperatures were almost the same: 475, 477, and  $480^\circ\text{C}$ , respectively, and the unreacted mole fractions were 0.24, 0.28 and 0.27, respectively. In Cycle 6, the decomposition peak temperature was  $570^\circ\text{C}$ , and the unreacted mole fraction was 0.20. This shows that, at different dehydration temperatures,

decomposition reactivity also changes. At higher dehydration temperatures, the decomposition increases because of high reaction rate. Cycles 1 and 6 had higher conversion rates which is calculated from unreacted mole fraction of  $\text{Ca(OH)}_2$  because of the higher dehydration temperature which depends primarily on system pressure and heater power.

#### 4.3.2.2 Hydration/Discharging Process

Fig. 4.7 shows the reactor center temperature and mole fraction of  $\text{Ca(OH)}_2$  as a function of time under repeated cycles and pressure of 470 kPa. The chemical reactor center temperature was maintained at 155–160°C, and the evaporator temperature was maintained around 148–150°C, and corresponding steam pressure was around 470 kPa. After the valve was opened at around 50 min, steam entered the chemical reactor, and hydration of CaO took place, as shown in Fig. 4.7. The peak temperature of Cycles 1, 2, 3, 4, 5, and 6 were 348, 332, 273, 283, 325, and 345°C, respectively, at a pressure of 470 kPa. Cycles 1, 2, and 6 showed higher temperature increases than the other cycles; conversions in the preceding dehydration cycles corresponding to those temperature were 0.82, 0.79, and 0.80 respectively. Cycles 3, 4, and 5 showed a relatively low temperature rise compared to other cycles, with lower conversions in the dehydration steps preceding them: 0.76, 0.72, and 0.73, respectively. The hydration reached peak temperature at around 160 min, and then it started to decrease. The hydration rate was high—between 120 and 160 min—after which hydration rates slowed as calculated by the change in mass of the chemical bed.

Cycle 1 mole fraction of  $\text{Ca(OH)}_2$  increases from 0.18 to 0.98, for cycle 2 0.21 to 0.98, for cycle 3 0.24 to 0.97, for cycle 4 0.28 to 0.97, for cycle 5 0.27 to 0.98 and for cycle 6 0.2 to 0.98. The final mole fractions of  $\text{Ca(OH)}_2$  are close to complete conversion (nearly~1) but initial values depend upon the previous dehydration conversion rate. The smaller the conversion during dehydration, the lower the temperature lift and mole fraction reacted during hydration reaction. The maximum temperatures reached during the hydration experiments were slightly lower than the equilibrium temperature at 470 kPa as shown in the Clausius-Clapeyron diagram. The two major factors that are likely responsible for this discrepancy are: i) a fraction of the exothermic heat of reaction released from the chemical bed went into heating the SS reactor, and ii) ~6-7% of energy was lost by natural convection to the atmosphere despite the experimental setup being insulated.

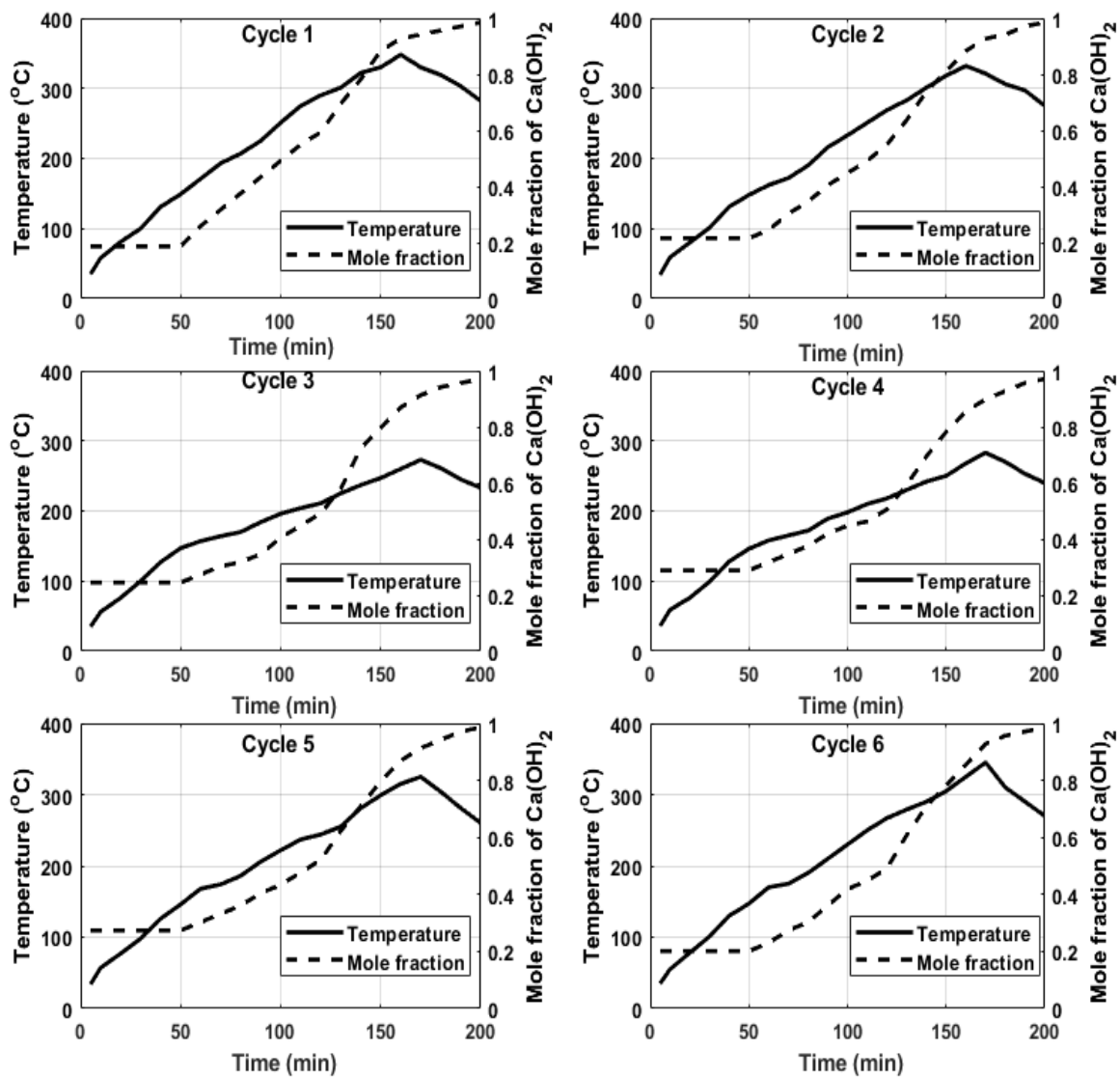


Figure 4.7 Chemical reactor center temperature and mole fraction of  $\text{Ca(OH)}_2$  vs time during the hydration reaction (Pressure  $\approx$  470 kPa)

### 4.3.2.3 Enthalpy Calculations

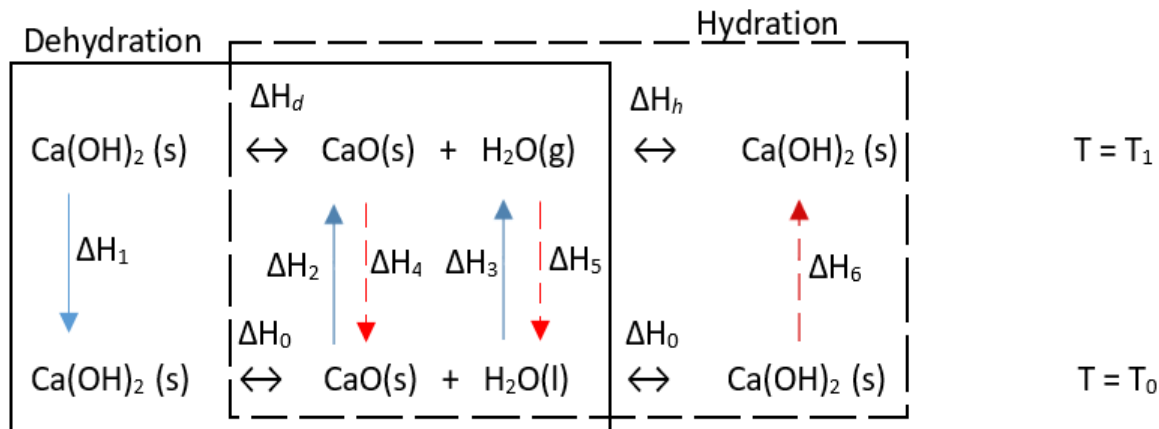


Figure 4.8 Energy storage/release process in a  $\text{Ca(OH)}_2/\text{CaO}$  system under different decomposition temperatures

The enthalpy of the reaction at different temperatures during dehydration and hydration is calculated using Hess's Law as shown in Fig. 4.8, where  $T_0 = 25^\circ\text{C}$  and  $T_1$  is the temperature at which dehydration and hydration is occurring. The black continuous lined box shown in Fig. 4.8 is the energy storage cycle or dehydration process while the dashed lined box shows the energy release cycle or hydration process. Thermal heat input and output to the system were calculated using these temperature-dependent enthalpies based on the average temperature between the times the valve is opened and is closed. Table 4.2 and Table 4.3 show the resulting reaction enthalpies at different average decomposition and hydration temperatures, respectively. It can be seen that the reaction enthalpy decreases with increase in decomposition temperature.

Table 4.2 Reaction enthalpies during dehydration at different decomposition temperatures for  $\text{Ca(OH)}_2/\text{CaO}$  system

Decomposition Temperature ( $^\circ\text{C}$ )	$\Delta H_0$ ( $\text{kJ mol}^{-1}$ )	$\Delta H_1$ ( $\text{kJ mol}^{-1}$ )	$\Delta H_2$ ( $\text{kJ mol}^{-1}$ )	$\Delta H_3$ ( $\text{kJ mol}^{-1}$ )	$\Delta H_d$ ( $\text{kJ mol}^{-1}$ )
390	63.6	-41.32	19.09	55.32	96.69
404	63.6	-42.91	19.82	55.84	96.35
408	63.6	-43.36	20.03	55.98	96.25
426	63.6	-45.40	20.97	56.67	95.84
431	63.6	-45.96	21.23	56.85	95.72
465	63.6	-49.81	23.01	58.13	94.93

Table 4.3 Reaction enthalpies at different hydration temperatures for Ca(OH)<sub>2</sub>/CaO system

Hydration Temperature (°C)	$\Delta H_0$ (kJ mol <sup>-1</sup> )	$\Delta H_4$ (kJ mol <sup>-1</sup> )	$\Delta H_5$ (kJ mol <sup>-1</sup> )	$\Delta H_6$ (kJ mol <sup>-1</sup> )	$\Delta H_h$ (kJ mol <sup>-1</sup> )
273	-63.6	-12.97	-54.04	28.08	-102.53
283	-63.6	-13.49	-51.39	29.21	-99.27
325	-63.6	-15.69	-52.93	33.97	-98.25
332	-63.6	-16.05	-53.18	34.76	-98.07
345	-63.6	-16.74	-53.67	36.23	-97.78
348	-63.6	-16.89	-53.77	36.57	-97.69

#### 4.3.2.4 Energy, Exergy and Efficiency Calculations

The calculated gross heat input-outputs at different temperatures under repeated cycles during dehydration-hydration are shown in Fig. 4.9. Gross heat calculations were made based on per kg of Ca(OH)<sub>2</sub>. Specific heat capacities of Ca(OH)<sub>2</sub> and CaO used for the calculations were 1530 and 934 J/kg K, respectively [6]. The processes considered for calculating gross heat input and available exergy included: (i) heating of the chemical bed to the corresponding peak temperature for different cycles for dehydration, (ii) reaction enthalpy during dehydration, (iii) heating of the chemical bed to 150°C during hydration, and (iv) heating the water and generating vapor in evaporator at 150°C during hydration. The processes considered for gross heat and exergy output calculations: (i) the heat of condensation of water vapor from the corresponding peak temperature from dehydration, and (ii) the reaction enthalpy during hydration. Gross heat input is the function of the unreacted mole fraction, which is itself a function of dehydration temperature. Cycles 1, 2, and 6 showed the highest gross-heat input 2419, 2386.5, and 2439.7 kJ/kg, respectively. Cycles 3, 4, and 5 showed gross heat input of 2303.8, 2246.4, and 2222.30 kJ/kg respectively which is on the lower side compared to cycles 1,2, and 6 because of low dehydration temperatures and low unreacted-mole fractions. Expressed on a volumetric basis, the gross heat inputs for cycles 1-6 were 1451.40, 1431.90, 1382.28, 1347.84, 1333.38 and 1463.82 MJ/m<sup>3</sup>, respectively. Gross output depends on both the mole fraction that reacts during hydration as well as the unconverted mole fraction of Ca(OH)<sub>2</sub> during the dehydration process. Cycles 1, 2, and 6 showed the highest thermal output: 1878.7, 1848.6, and 1876.9 kJ/kg, respectively. Cycles 3, 4, and 5 showed thermal heat output of 1797.2, 1707.7, and 1738.3 kJ/kg, respectively, because of the low extent of reaction from the dehydration process. On a volumetric basis, the gross heat output values for cycles 1-6

were 1127.22, 1109.16, 1078.32, 1024.62, 1042.98 and 1126.14 MJ/m<sup>3</sup>, respectively. The gross input energy is comprised of sensible heating and energy due to chemical reaction and gross heat output due to condensation of water vapor and energy due to chemical reaction are shown in Table 4.4. Above calculations do not include the sensible heat needed to heat up the SS reactor and aluminum vessel used as evaporator. Table 4.4 shows that the system accumulates heats sensibly more than chemically. This is a consequence of the procedure used in conducting the experiments where the system was cooled down to ambient conditions after each reaction step, so a sample of pellet could be withdrawn for examination of structural integrity. Consequently, both the reactor vessel and reactants needed to heat back to ~150°C for the hydration step. This was accomplished by electrical heating. Subsequent exothermic hydration step resulted in the increase in the temperatures of the reactor bed and vessel. As a portion of the reaction enthalpy got used in raising the vessel temperature, the reactor bed temperature did not reach the equilibrium temperature expected from the Clausius-Clapeyron diagram. In the practical operation, the system will not be cooled down after the dehydration step, and minimal energy will be diverted to heating of the reactor vessel, enabling the bed to reach the expected high temperatures.

Table 4.4 Gross heat input-output at different repeated cycles for Ca(OH)<sub>2</sub>/CaO system\*

Cycle No.	Gross energy input (kJ/kg)			Gross energy output (kJ/kg)		
	Sensible heat	Chemical reaction	Total gross energy input	Condensation	Chemical reaction	Total gross energy output
1	1366.70	1052.30	2419	824.60	1054.10	1878.7
2	1370.50	1016	2386.5	822	1026.60	1846.6
3	1320.25	983.50	2303.8	790.80	1006.60	1797.2
4	1316.32	930	2246.4	791.80	915.90	1707.7
5	1277.60	944.70	2222.3	793.24	945	1738.3
6	1414.70	1025	2439.7	840.40	1036.50	1876.9

\*The energy input-output values on a gravimetric basis (kJ/kg) are converted to volumetric basis by multiplying with the packed density of 600 kg/m<sup>3</sup>

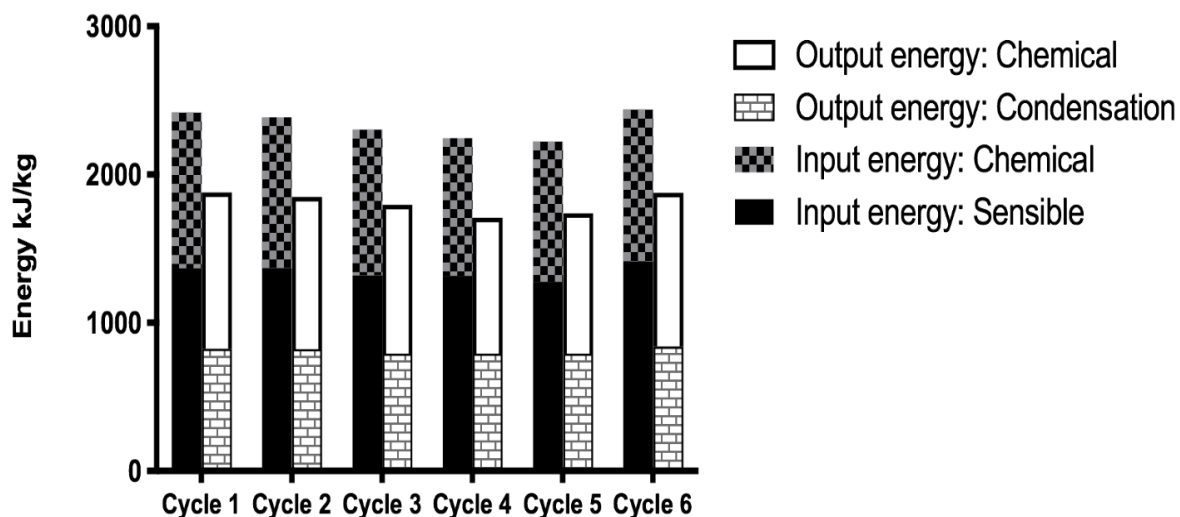


Figure 4.9 Gross heat energy after repeated dehydration-hydration process

The calculated exergy available-output at different temperatures under repeated cycles during dehydration-hydration are shown in Fig. 4.10. In Cycles 1, 2, and 6 showed the highest exergy available: 1185.26, 1158.49, and 1231.48 kJ/kg, respectively. Cycles 3, 4, and 5 showed exergy available of 1093.97, 1043.69, and 1069.15 kJ/kg respectively which is on the lower side compared to cycles 1,2, and 6 because of low dehydration temperatures and low unreacted-mole fractions. Expressed on a volumetric basis, the exergy available for cycles 1-6 was 711.15, 696.09, 656.38, 626.21, 641.49 and 738.88 MJ/m<sup>3</sup>, respectively. Exergy output depends on both the mole fraction that reacts during hydration as well as the unconverted mole fraction during the dehydration process. Cycles 1, 2, and 6 showed the highest exergy output: 1070.94, 1036.62, and 1079.95 kJ/kg, respectively. Cycles 3, 4, and 5 showed exergy output of 932.85, 902.16, and 953.43 kJ/kg, respectively, because of the low extent of reaction from the dehydration process. The volumetric exergy output in for cycles 1-6 was 642.56, 621.97, 559.71, 541.29, 572.07 and 647.97 MJ/m<sup>3</sup>, respectively. The exergy available is comprised of sensible heating and energy due to chemical reaction and exergy output due to condensation of water vapor and energy due to chemical reaction are shown in Table 4.5.

Table 4.5 Exergy available-output at different repeated cycles for Ca(OH)<sub>2</sub>/CaO system

Cycle No.	Exergy available (kJ/kg)			Exergy output (kJ/kg)		
	Sensible heat	Chemical reaction	Total exergy available	Condensation	Chemical reaction	Total exergy output

1	578.51	606.75	1185.26	522.34	548.60	1070.94
2	575.66	582.83	1158.49	518.85	517.77	1036.62
3	543.37	550.60	1093.97	475.75	457.10	932.85
4	531.37	512.32	1043.69	477.16	425	902.16
5	537.83	531.32	1069.15	479.31	474.12	953.43
6	620.40	611.08	1231.48	543.24	536.71	1079.95

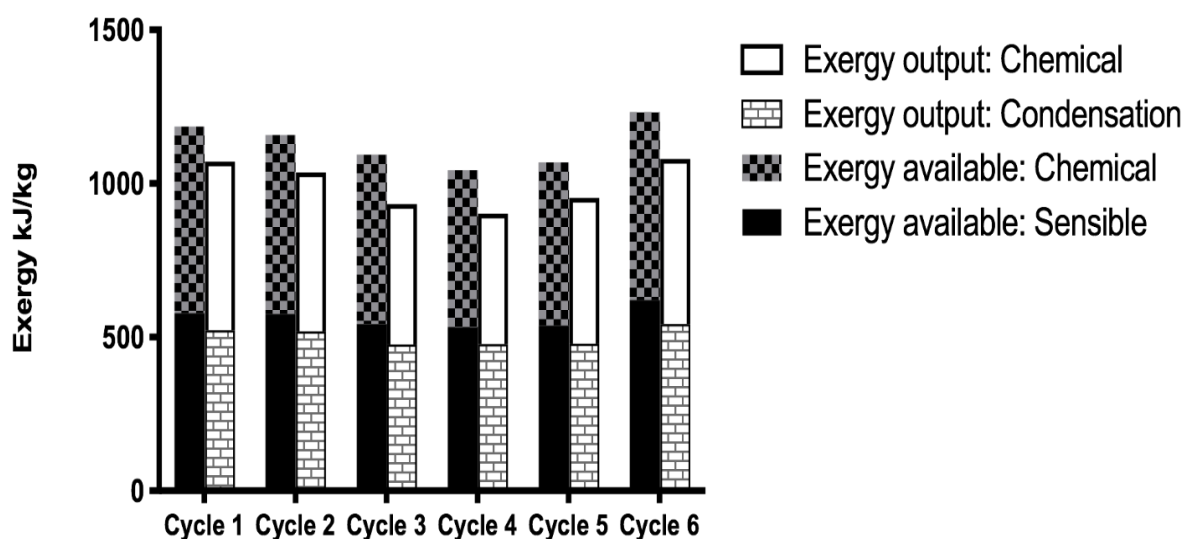


Figure 4.10 Exergy after repeated dehydration-hydration process

The Fig. 4.11 shows the energy and exergy efficiencies under repeated dehydration-hydration cycles. The energy and exergy efficiency ranges from 76 to 79% and 85 to 91%, respectively. One of the other factors gross energy and exergy available depend upon the enthalpy of reaction as it is dependent on temperature as shown by Hess Law. The efficiency calculations reflect the operational mode of the system that involves a complete cool-down of the reactor to ambient temperature between the dehydration and hydration reactions. The overall system efficiency can be increased by maintaining the system at the elevated temperature between the two steps, which will be more reflective of the operation of a practical system. Maintaining the reactor at the initial hydration temperature (which is 150°C in this case) after dehydration will obviate the need to supply additional energy to heat the reactor from the ambient temperature to the initial hydration temperature. The energy and exergy efficiencies can be increased by 2-3% by operating in this mode.

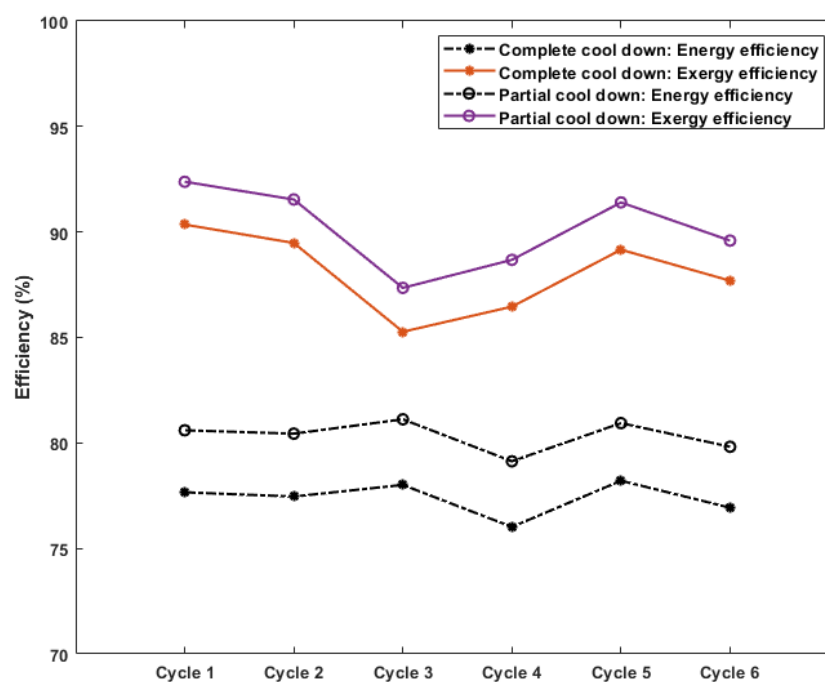


Figure 4.11 Energy and exergy efficiencies after repeated dehydration-hydration process

#### 4.3.2.5 Morphology and Structural Integrity of $\text{Ca}(\text{OH})_2$ Pellets

The  $\text{Ca}(\text{OH})_2$  and  $\text{CaO}$  pellets were subjected to scanning electron microscopy (SUPRA 35 VP). Up to two pellets were taken out from top of the reactor after each reaction through a  $\frac{1}{2}$ " nozzle provided for such withdrawal without disturbing the chemical bed to avoid changing the characteristics of the bed. Fig. 4.12 and Fig. 4.13 show the SEM images of fresh and post 1<sup>st</sup> dehydration cycle of  $\text{Ca}(\text{OH})_2$ , respectively. Initiation of a few cracks and roughening of the surface started due to the surge in the number of pores can be noticed. Fig. 4.14 shows SEM images after the 1<sup>st</sup> hydration, and it is observed that the surface roughness and pores increased, most likely due to transport of water vapor in and out during the reactions. Fig. 4.15 shows SEM images post the 6<sup>th</sup> dehydration cycle and increases in the crack width and number of pores can be clearly seen. Fig. 4.16 shows SEM images after the 6<sup>th</sup> hydration cycle at different magnifications, and it is observed that the crack width from Fig. 4.15 had shrunk slightly, as shown in Fig. 4.16. This is possibly due to the increase in the volume of the  $\text{Ca}(\text{OH})_2$  pellet after hydration reaction. There was no significant influence on the reaction rate or conversion after six repeated cycles.

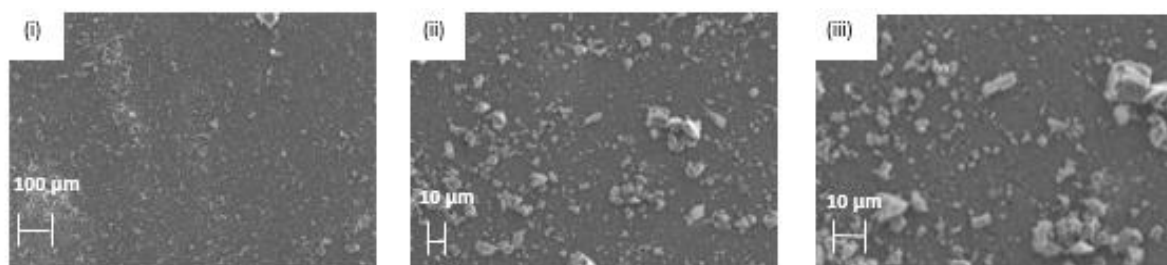


Figure 4.12 SEM images of fresh  $\text{Ca}(\text{OH})_2$  pellet at magnification (i) 100 X (ii) 500 X (iii) 1000 X



Figure 4.13 SEM images after 1<sup>st</sup> dehydration reaction at magnification (i) 100 X (ii) 500 X (iii) 1000 X

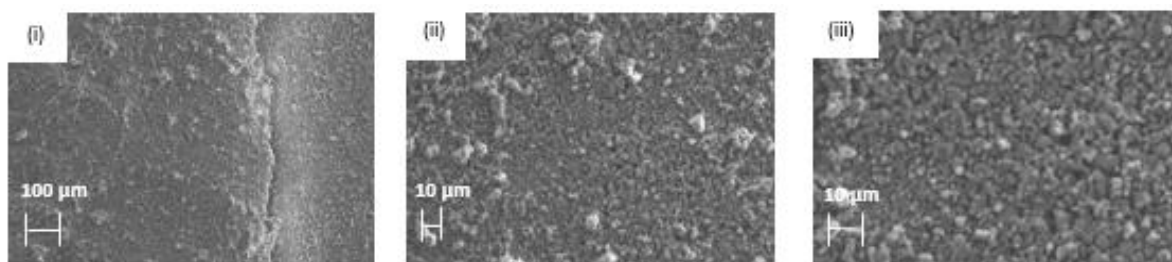


Figure 4.14 SEM images after 1<sup>st</sup> hydration reaction at magnification (i) 100 X (ii) 500 X (iii) 1000 X

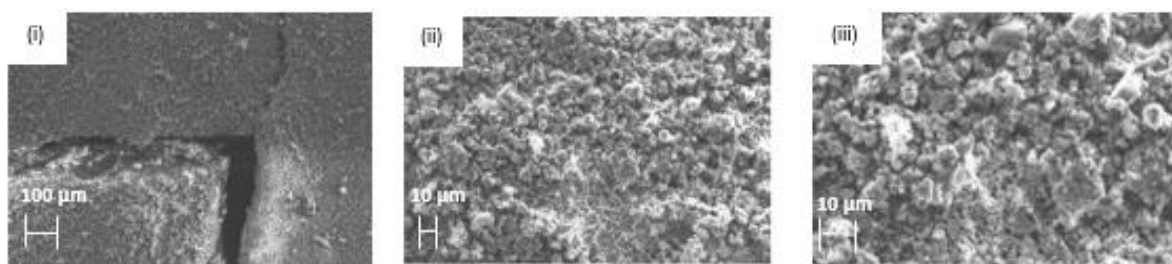


Figure 4.15 SEM images after 6<sup>th</sup> dehydration reaction at magnification (i) 100 X (ii) 500 X (iii) 1000 X

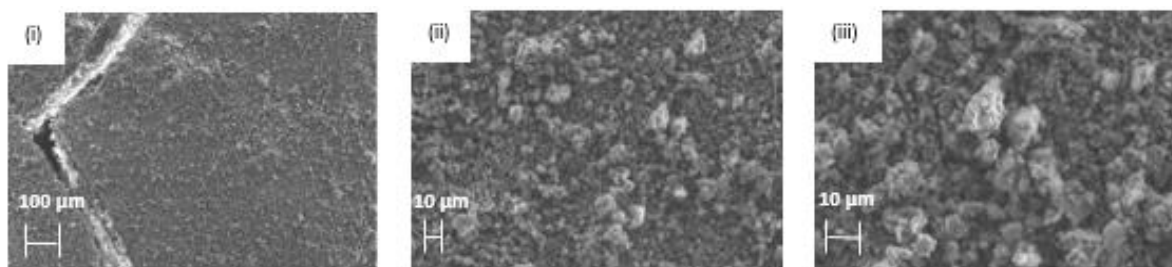


Figure 4.16 SEM images after 6<sup>th</sup> hydration reaction at magnification (i) 100 X (ii) 500 X (iii)

### 4.3.3 Pure Ca(OH)<sub>2</sub> Pellet vs Powder Comparison

#### 4.3.3.1 Dehydration Results

The aim of the study was to compare the results of Ca(OH)<sub>2</sub>/CaO dehydration-hydration reaction using pellets and powder as solid reactant. The pellet dimensions were: 8 mm diameter X 7 mm height, and the powder used with particle size 5.5μm. One cycle of dehydration-hydration was performed with both pellets and powder. A repeated cycle with powder was conducted just to check the reproducibility of the results. The operating conditions for both the experiments (pellets and powder) are listed below in Table 4.6.

Table 4.6 Operating conditions for the experiments

Operating Conditions	Pellets	Powder
Mass of Ca(OH) <sub>2</sub> (g)	303	305
Dehydration Pressure (kPa)	2.5-3	101.325
Hydration Pressure (kPa)	470	470

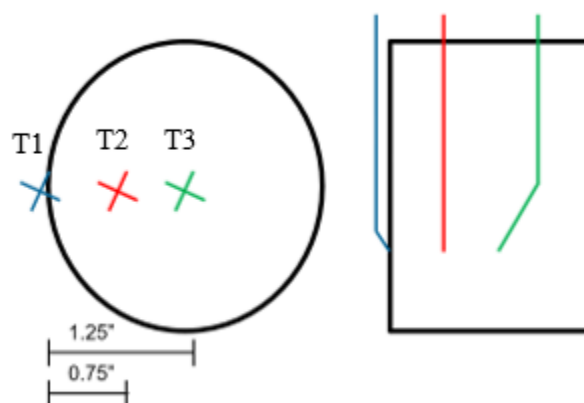


Figure 4.17 Thermocouples position in chemical reactor

Fig. 4.17 shows the chemical reactor outer temperature with time, which is denoted by T1, the temperature of chemical bed at 0.75' distance from the outer thermocouple and is denoted by T2, and the center temperature which is at 1.25' from the outside thermocouple and denoted by T3.

During dehydration with pellets, the dehydration pressure was in between 2.5 – 3 kPa which was corresponding to the water temperature inside the condenser at 20°C. Before starting the experiment, air is evacuated from system by using the vacuum pump. But when conducting the experiments with powder, the dehydration pressure was maintained at 101.325 kPa or atmospheric pressure because if we use the vacuum pump then there was chance of powder getting pulled out with air. The results of dehydration-hydration experiments are discussed below in details.

#### *Dehydration Process with pellets*

Approximately 303 g of  $\text{Ca}(\text{OH})_2$  pellets are placed in the chemical reactor, and air is evacuated using the vacuum pump. After the air has been evacuated, the valve is closed, and water is injected into the condenser. The water temperature inside the condenser was maintained at 20°C through refrigerator bath. The band heater is started on the chemical reactor and once the temperature inside the reactor reaches 200°C at 80 min the high temperature valve is opened.

#### *Dehydration process with powder*

Approximately 305 g of  $\text{Ca}(\text{OH})_2$  powder is placed in the chemical reactor and water is injected into the condenser keeping valve closed. The water temperature inside the condenser was maintained at 20°C through refrigerator bath. The band heater is started on the chemical reactor and the high temperature valve is opened at 80 min.

#### *Results comparison*

Figs. 4.18, 4.19 and 4.20 shows the temperature plot with respect to time. Black vertical line shows the time when the high temperature valve was opened. It was observed from the above-mentioned graphs that the powder was taking longer time to heat, or transfer heat compared to pellets at constant power input from the band heater. There was almost 50 min of lag time

between both the temperatures (pellets and powder) to reach the peak temperature as pellets reach the peak temperature 50 min earlier.

Fig. 4.21 shows the unreacted mole fraction with respect to time, and it can be clearly observed that the decomposition had a delayed start with powder as compared with pellets because of slow heat transfer inside the chemical bed. So, using powder as a solid reactant we are transferring more heat to the chemical bed to reach the peak temperature compared to pellets. The pellets porosity in chemical bed is less as compared to powdered chemical bed because of its compactly packed which is the reason of its high heat transfer. But the conversion is slightly higher when using powder than pellet because of high surface area or reaction front available to heat transfer which directly increases the reactant conversion to product. One of the reasons using pellets have high heat transfer because with pellets we have voids inside the chemical reactor and once the decomposition starts these voids gets filled up with water vapor which give rise to convective heat transfer.

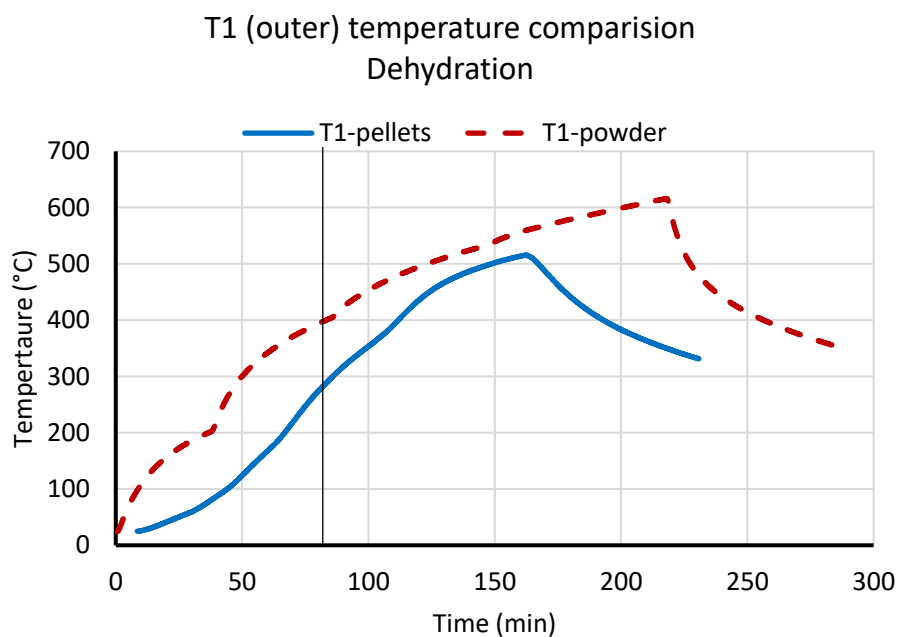


Figure 4.18 Temperature (outer) vs time plot during dehydration with pellet and powder

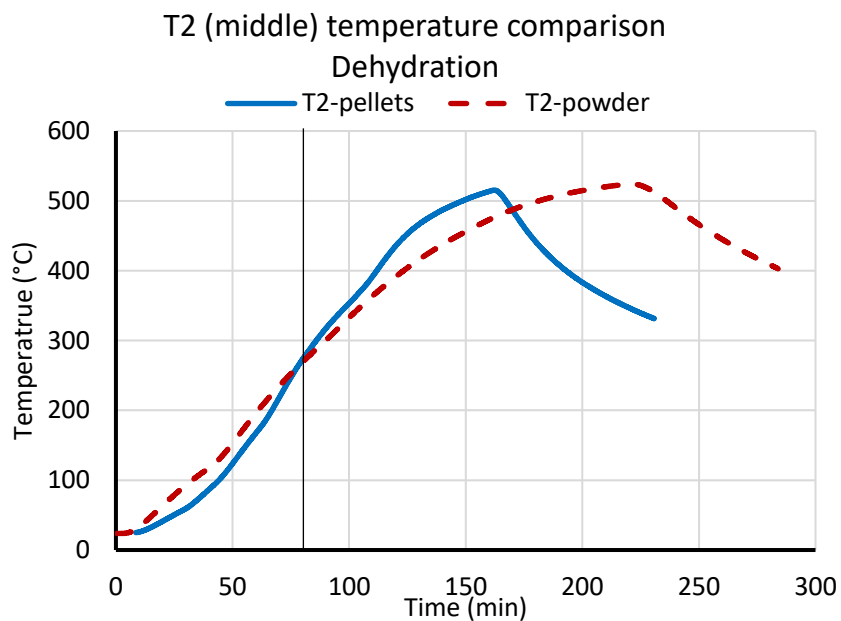


Figure 4.19 Temperature (middle) vs time plot during dehydration with pellet and powder

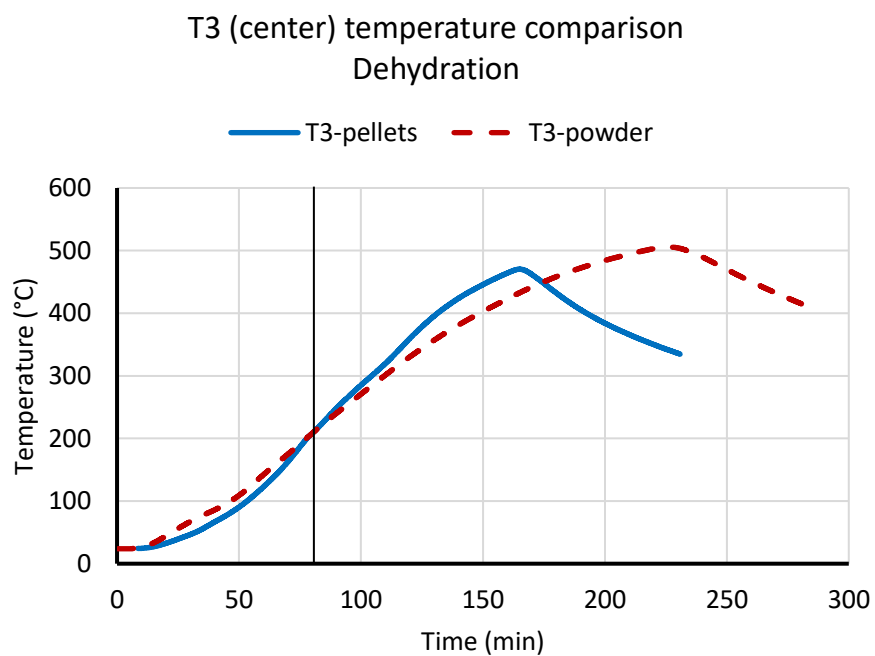


Figure 4.20 Temperature (center) vs time plot during dehydration with pellet and powder

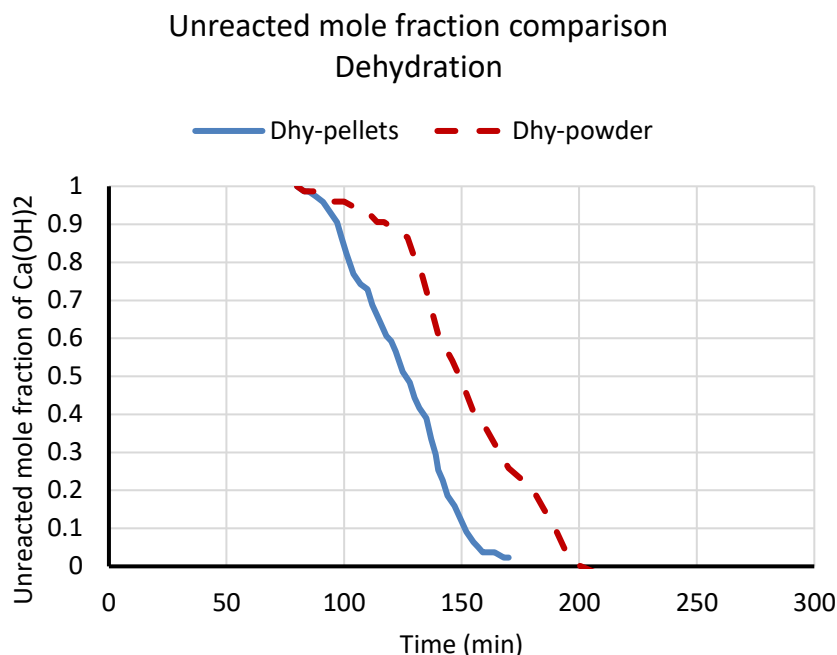


Figure 4.21 Unreacted mole fraction of reactant during dehydration with pellets and powder

### 4.3.3.2 Hydration Results

#### *Hydration reaction with pellets*

After the dehydration with pellets, now we have CaO pellets inside the chemical reactor. Before starting the hydration reaction, the air is evacuated using the vacuum pump, following which the high temperature valve is closed. Then the water is injected in the evaporator and band heater is turned on both evaporator and chemical reactor. The evaporator is heated to 150°C, and saturation pressure of steam corresponding to that is around 470 kPa. The chemical reactor is heated to maintain a temperature slightly greater (10-20°C) than that of saturation temperature of steam and once the evaporator reaches to its saturation temperature, the high temperature valve is opened at 90 min and the high-pressure water vapor allowed to flow through chemical bed.

#### *Hydration reaction with powder*

The only difference in the experimental procedure while doing hydration with powder is that the air is not evacuated from the reactor, or vacuum pump is not used because it might take the

powder with air while evacuating the air. The rest of the procedure is similar to hydration with pellets and high temperature valve is opened at 90 min as well.

### *Results comparison*

Figs. 4.22, 4.23 and 4.24 shows the temperature plot with respect to time during hydration. Black vertical line shows the time when the high temperature valve was opened. Once the high temperature valve was opened around 90 mins, there was an exothermic reaction taking place and temperature inside the chemical bed reduced to saturation temperature of steam and then it started to increase. From the above-mentioned figures, it can be observed that with pellets the peak temperature was around 370°C and with powder it was around 400°C. One of the main reasons of higher temperature peak when using powder was that the water vapor has more surface area available to react with CaO whereas with pellets the water vapor has to penetrate inside the pellet. Fig. 4.25 shows the mole fraction of Ca(OH)<sub>2</sub> with respect to time and the rate of conversion of powder during hydration was slightly higher than the pellets.

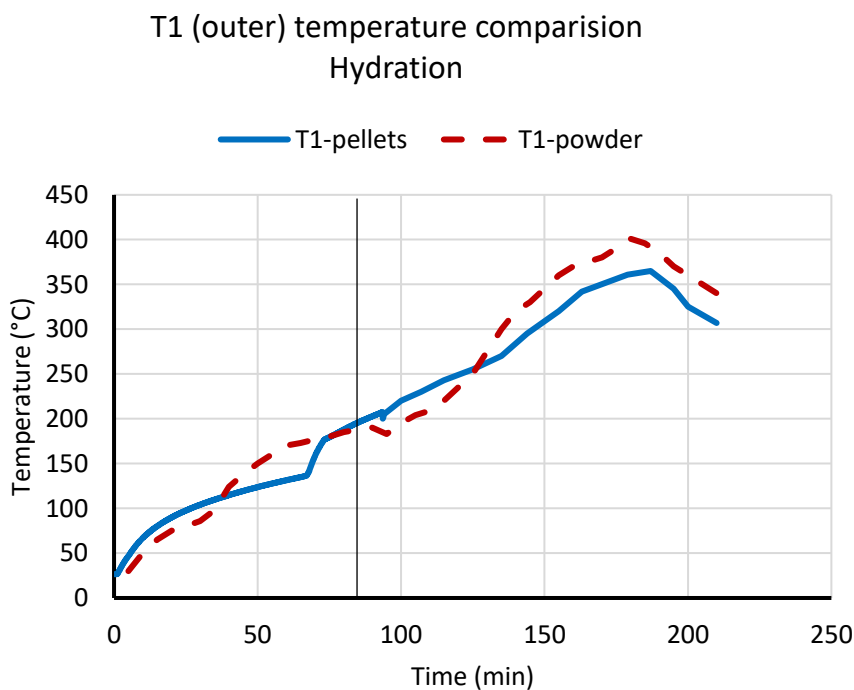


Figure 4.22 Temperature (outer) vs time plot during hydration with pellet and powder

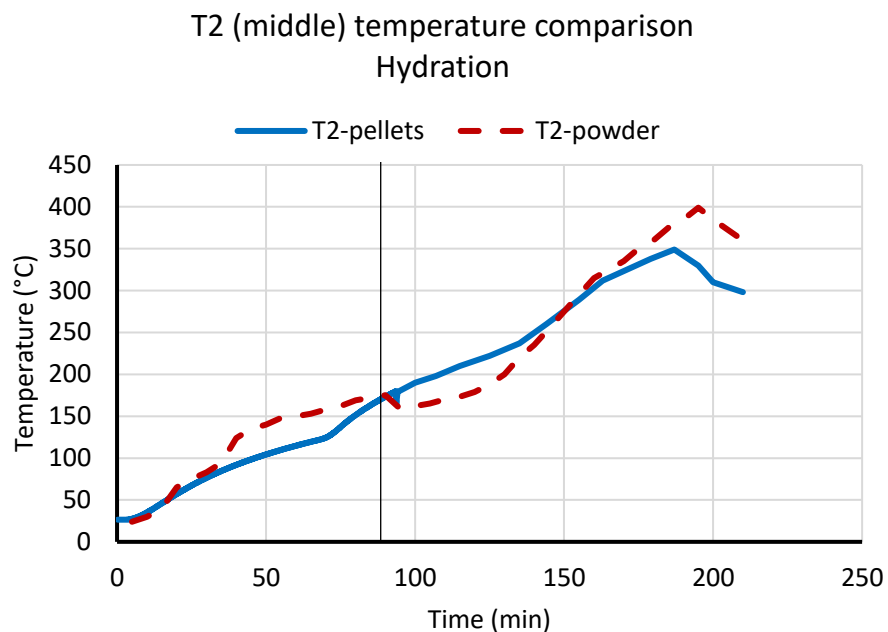


Figure 4.23 Temperature (middle) vs time plot during hydration with pellet and powder

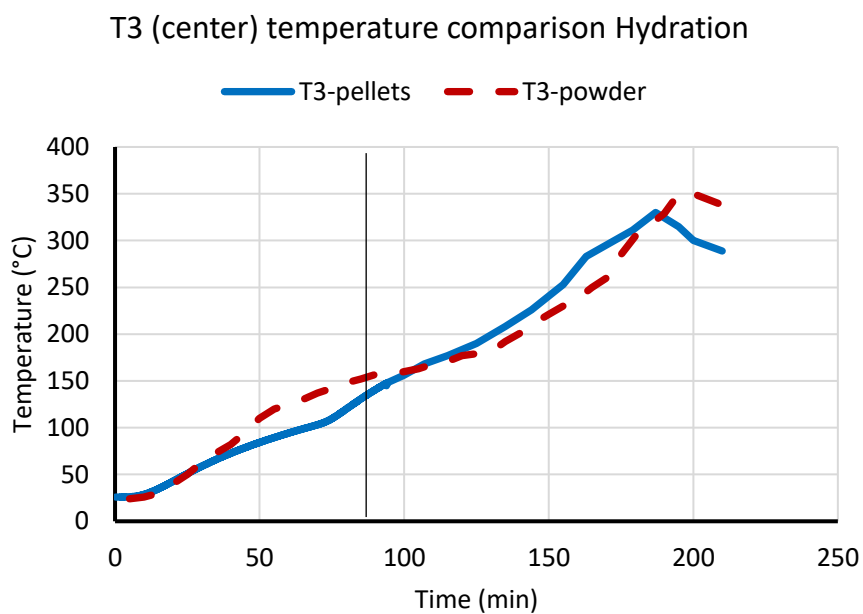


Figure 4.24 Temperature (center) vs time plot during hydration with pellet and powder

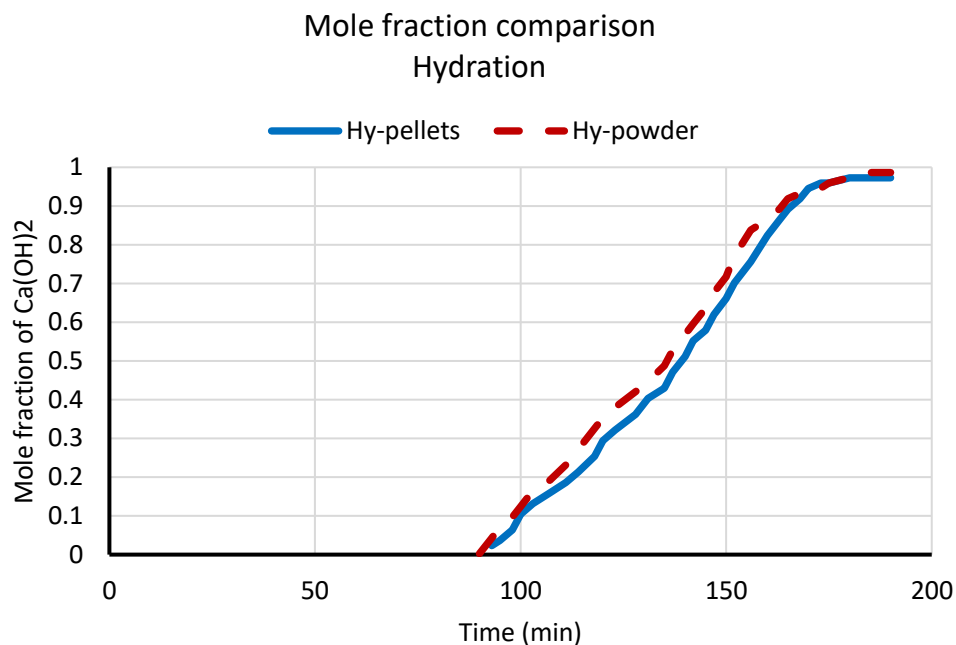


Figure 4.25 Mole fraction of  $\text{Ca}(\text{OH})_2$  during hydration with pellets and powder

#### 4.3.3.3 Experimental Issues with Powdered $\text{Ca}(\text{OH})_2$

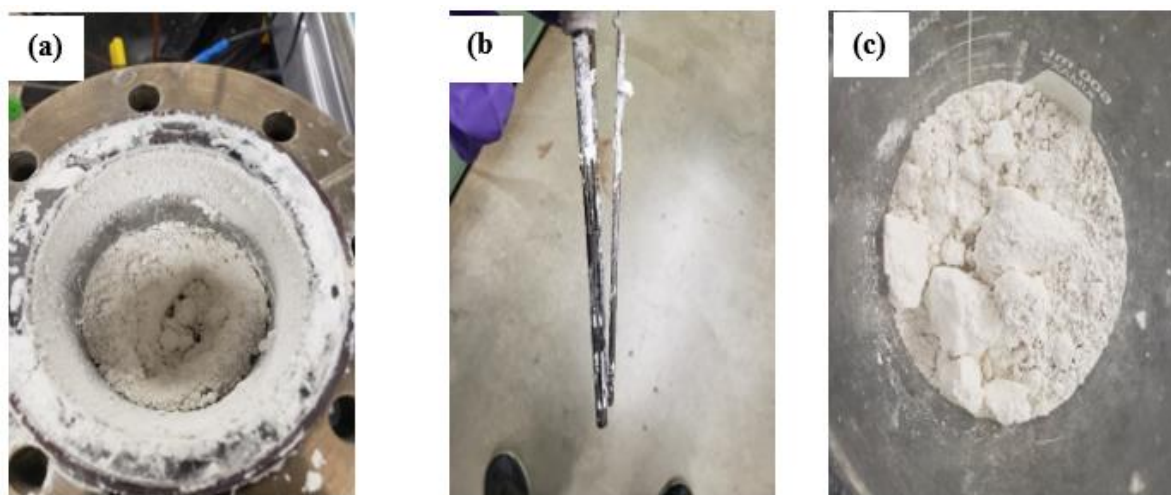


Figure 4.26 Powder condition after completing 2nd cycle

During hydration, pressure was being released from the reactor top after valve was open and it kept releasing for at least 10 min. It was being released from the fittings on the top of the chemical reactor. Because of this issue, there was a decrease in system pressure hence, directly impacting the hydration reaction. Powder got filled in the water vapor distribution tube (on lower end) as seen in Fig. 4.26 b. Agglomeration of powder after 2 complete cycle was

observed, clumps of  $\text{Ca(OH)}_2$  were formed inside the chemical reactor as seen in Figs. 4.26 a and c.

#### **4.3.4 Experimental Results on Composite Pellet (1:0.5 :: $\text{Ca(OH)}_2$ : $\text{CaTiO}_3$ )**

##### **4.3.4.1 Result on Subsequent Dehydration-Hydration Cycles**

Fig. 4.27 shows the results of the first dehydration-hydration cycle. The dehydration reaction starts at 65 min when high temperature valve was opened and is completed around ~205 min. T1 and T2 are the temperatures at a location 0.75-in from the wall and at center, respectively. No change in mass of chemical bed after 205 min indicated that dehydration was complete, and the condenser pressure was maintained at 2.4 kPa during reaction. After the dehydration process, the chemical bed is cooled down to 300°C and water was heated to 150°C raising the pressure in the evaporator to 470 kPa. Once the chemical bed temperature was reached to 300°C the high temperature valve was opened to allow the water vapor to flow into the chemical bed at ~300 min to initiate hydration., T1 and T2 reached to ~480°C and ~425°C, respectively, during the hydration process. The hydration was completed in ~100 min and no further mass change was observed in chemical bed. Temperature amplification of 180°C (300-480°C) was achieved.

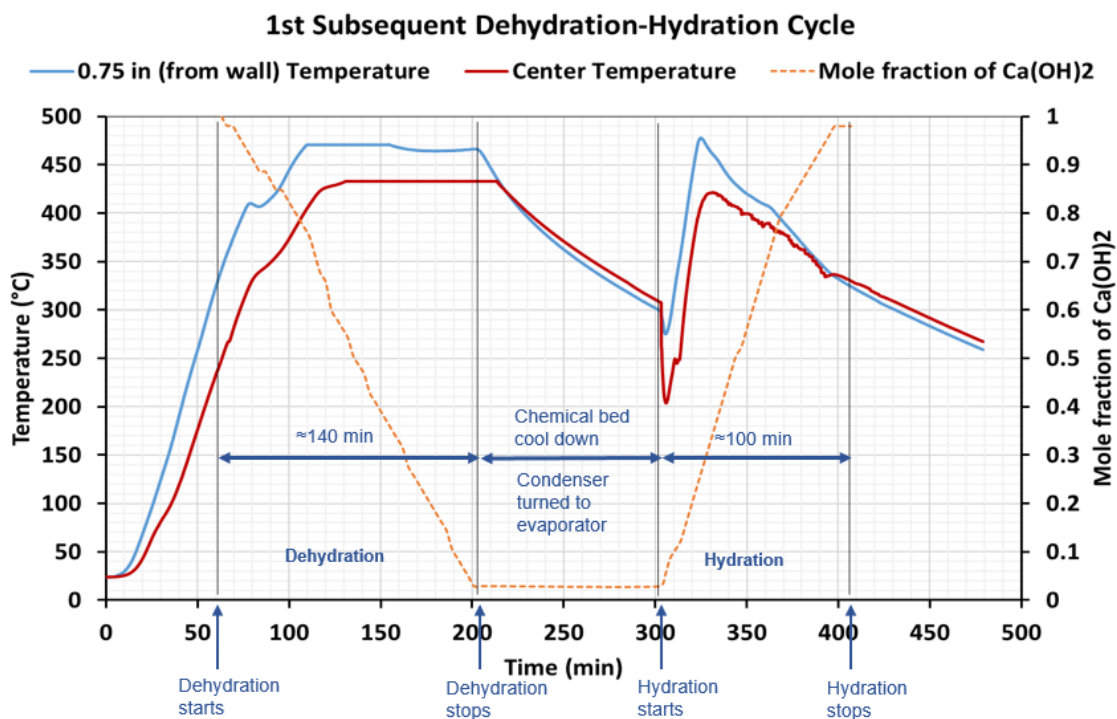


Figure 4.27 Temperature and mole fraction of  $\text{Ca(OH)}_2$  for 1<sup>st</sup> repeated dehydration-hydration cycle

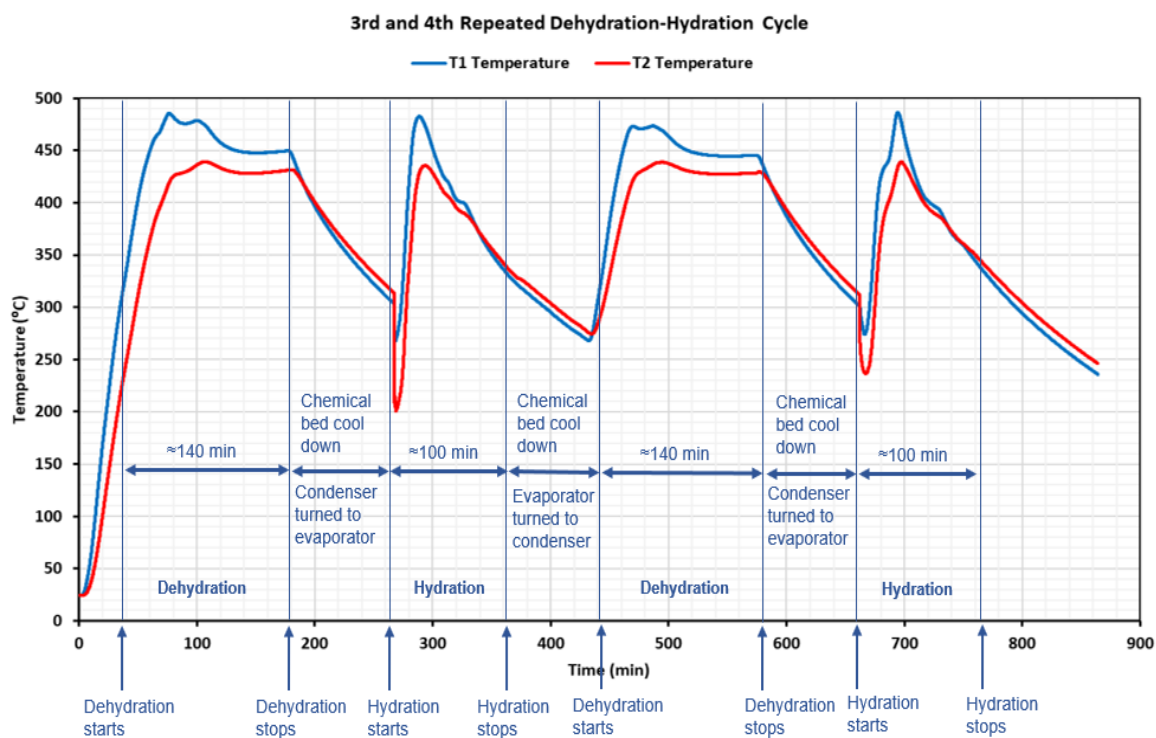


Figure 4.28 Temperature of  $\text{Ca(OH)}_2$  for 3<sup>rd</sup> and 4<sup>th</sup> continuous dehydration-hydration cycle

Fig. 4.28 shows the results of two continuous (one dehydration-hydration cycle followed by other) dehydration-hydration cycles which was conducted to study how results will behave in a continuous process and the challenges associated with it. The two continuous cycle runs were successfully conducted and were repeated for 20 cycles (2 cycles each time). Dehydration reaction time was ~140 min whereas hydration took ~100 min to finish. The continuous cycle experiment took around 750 mins to completed. Structural integrity of the pellet after each cycle was also monitored. The mole fraction of  $\text{Ca}(\text{OH})_2$  was decreased from 1 to 0.923 at the end of 20 cycles as shown in Fig. 4.29. Table 4.7 shows the dehydration and hydration temperatures of the 20 cycles.

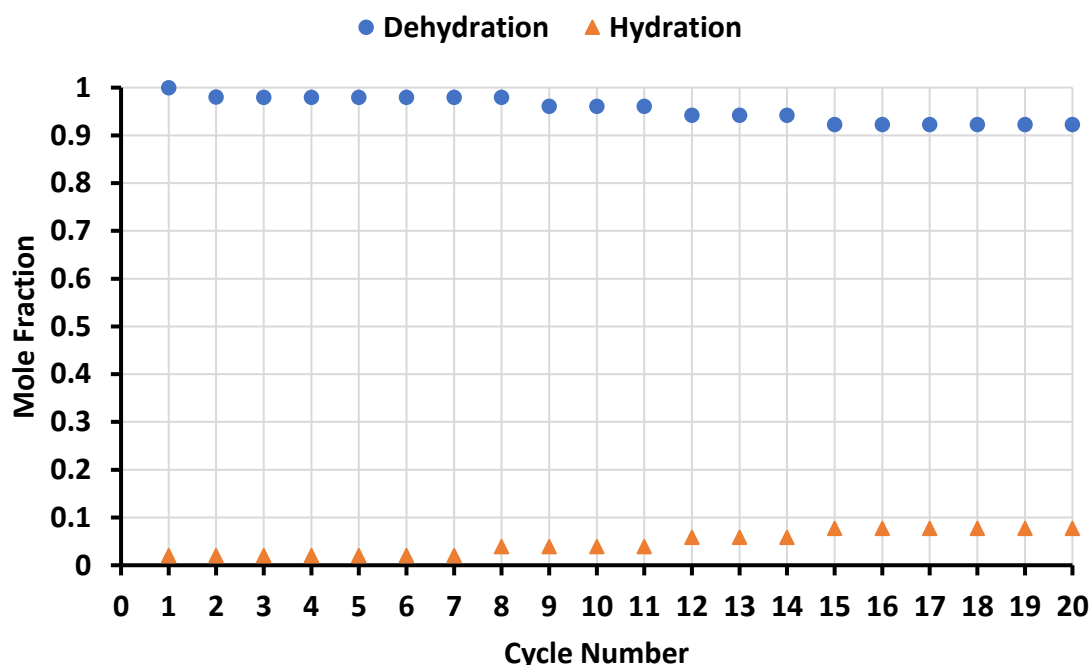


Figure 4.29 Mole fraction of  $\text{Ca}(\text{OH})_2$  for 20 dehydration-hydration cycles

Table 4.7 Dehydration-hydration peak temperatures for different cycles

CYCLE NUMBER	DEHYDRATION TEMPERATURE ( $^{\circ}\text{C}$ )		HYDRATION TEMPERATURE ( $^{\circ}\text{C}$ )	
	T1	T2	T1	T2
1	464	434	478	422
2	455	434	481	427
3	448	428	482	435
4	445	427	486	439
5	447	428	483	432
6	460	435	479	431

7	440	424	476	435
8	443	427	473	431
9	448	431	495	443
10	447	430	485	437
11	450	434	486	435
12	447	432	474	437
13	446	429	485	439
14	444	426	475	434
15	449	431	480	436
16	444	430	473	433
17	448	431	482	437
18	445	429	472	435
19	448	430	476	435
20	444	428	470	434

#### 4.3.4.2 Structural Strength and Morphology of Composite Pellet



Figure 4.30 Pellet after the first decomposition of  $\text{Ca(OH)}_2$ : (a) pure  $\text{Ca(OH)}_2$ , (b) composite pellet and c) after 20 cycles

Pure  $\text{Ca(OH)}_2$  pellet after the decomposition developed some cracks but no cracks were observed on the composite pellet surface even after 20 cycles, as shown in Fig. 4.30 (a), (b) and (c), respectively. It can be observed that composite pellet modified with  $\text{CaTiO}_3$  affects the kinetics of dehydration-hydration reaction significantly, but it decreases the quantity of reactant present in the pellet of same size. So, while designing the chemical reactor for  $\text{Ca(OH)}_2/\text{CaO}$  reaction, we need to account for this decrease in reactant quantity because of addition of inert agent. Fig. 4.31 shows the compressive strength (Satec T5000) of  $\text{Ca(OH)}_2$  and composite pellets before decomposition and results showed that addition of  $\text{CaTiO}_3$  increases the mechanical strength of the pellets by >55%. The compressive strength decreased by 6.7% after 20th cycle for composite pellet. The compressive strength of composite pellet was still 45% higher after 20<sup>th</sup> cycle when compared to pure  $\text{Ca(OH)}_2$  pellet. Figs 4.32, 4.33 and 4.34 shows the SEM images at 50 X and 100 X magnifications after 1<sup>st</sup>, 10<sup>th</sup> and 20<sup>th</sup> cycle, respectively. The images showed that there were no cracks developed after 20<sup>th</sup> cycle.

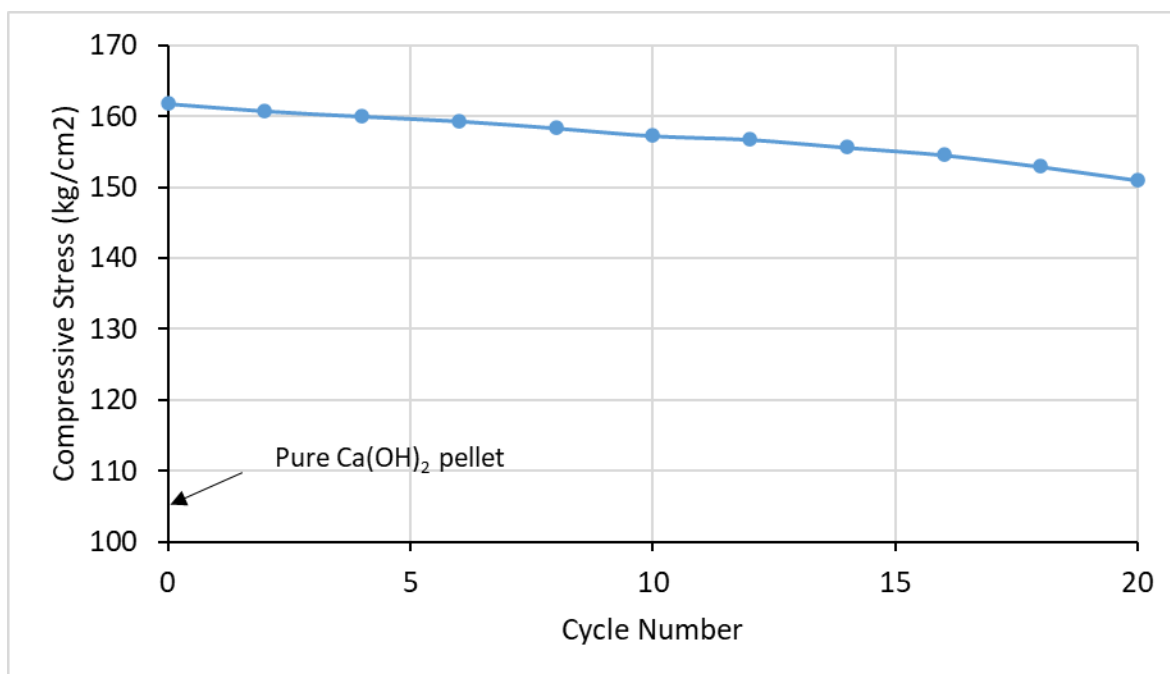


Figure 4.31 Compressive strength of composite pellet at different cycles

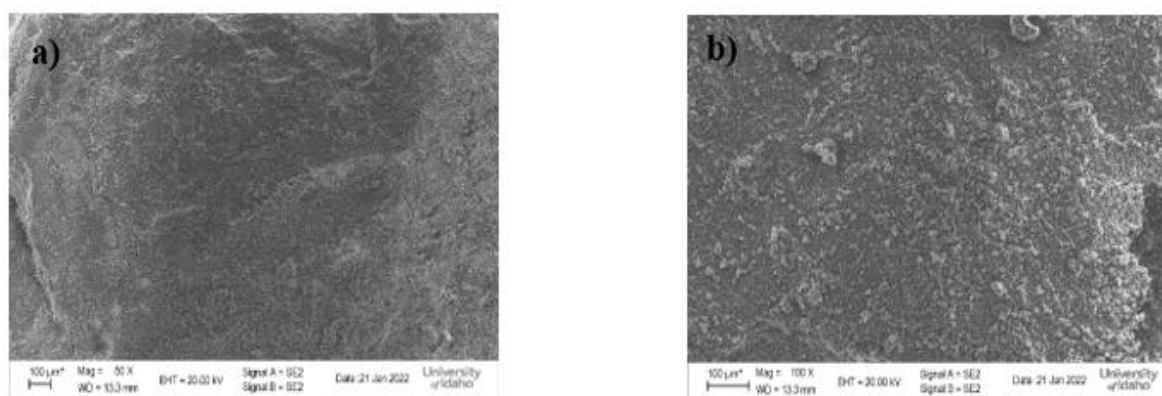


Figure 4.32 SEM images of composite pellets after 1<sup>st</sup> cycle a) 50 X and b) 100 X

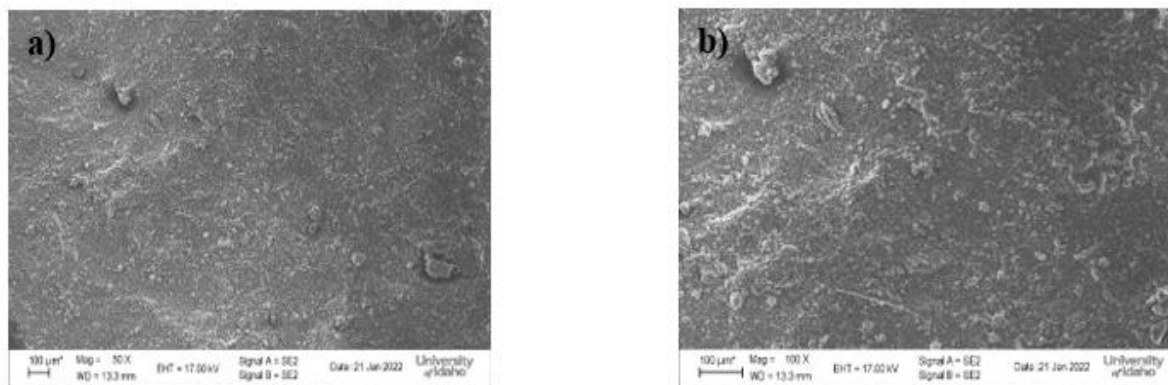


Figure 4.33 SEM images of composite pellets after 10<sup>th</sup> cycle a) 50 X and b) 100 X

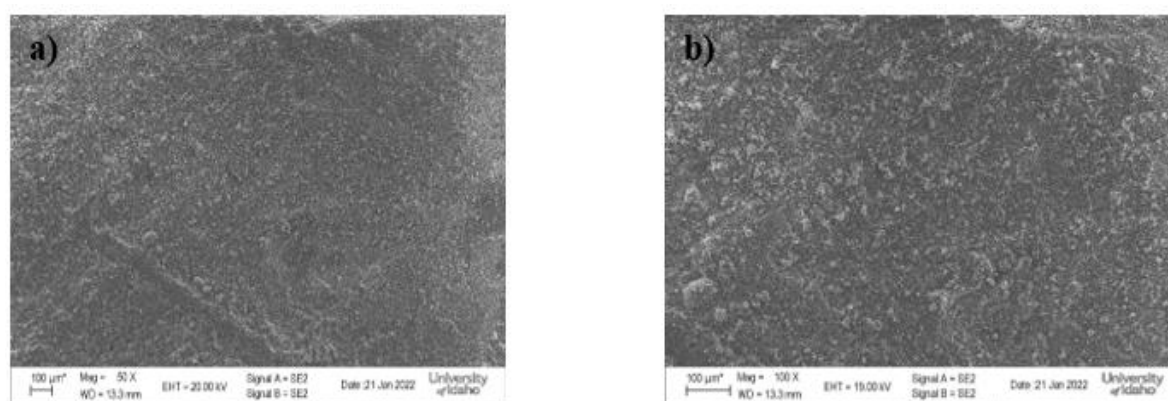


Figure 4.34 SEM images of composite pellets after 20<sup>th</sup> cycle a) 50 X and b) 100 X

Pure  $\text{Ca(OH)}_2$  pellets developed cracks after 6 cycles, whereas composite pellet comprising 1:0.5 ::  $\text{Ca(OH)}_2$ : $\text{CaTiO}_3$  by wt.% did not develop any cracks and maintained the structural integrity after 20 cycles.

Repeated dehydration – hydration cycles conducted on a laboratory scale showed cracks on the  $\text{Ca(OH)}_2$  pellets after 6 repeated cycles, but no cracks were observed on composite pellets after 20 cycles. Temperature amplification of  $\sim 180$ - $190^\circ\text{C}$  was achieved in the bench-scale experiment during hydration reaction with composite pellets (1:0.5 ::  $\text{Ca(OH)}_2$ : $\text{CaTiO}_3$ )

## References

1. Y. Kato, N. Yamashita, K. Kobayashi, Y. Yoshizawa. 1996. “Kinetic study of the hydration of magnesium oxide for a chemical heat pump.” *Applied Thermal Engineering* 16:853–862. [https://doi.org/10.1016/1359-4311\(96\)00009-9](https://doi.org/10.1016/1359-4311(96)00009-9).
2. M. Zamengo, J. Ryu, Y. Kato. 2013. “Magnesium hydroxide – expanded graphite composite pellets for a packed bed reactor chemical heat pump.” *Applied Thermal Engineering* 61:853–858. <https://doi.org/10.1016/j.applthermaleng.2013.04.045>.
3. M. Zamengo, J. Ryu, Y. Kato. 2014. “Thermochemical performance of magnesium hydroxide–expanded graphite pellets for chemical heat pump.” *Applied Thermal Engineering* 64:339–347. <https://doi.org/10.1016/j.applthermaleng.2013.12.036>.
4. M. Arjmand, L. Liu, I. Neretnieks. 2013. “Exergetic efficiency of high-temperature-lift chemical heat pump (CHP) based on CaO/CO<sub>2</sub> and CaO/H<sub>2</sub>O working pairs.” *International Journal of Energy Research* 37:1122–1131. <https://doi.org/10.1002/er.2918>.
5. X.F. Long, L. Dai, B. Lou, J. Wu. 2017. The kinetics research of thermochemical energy storage system Ca(OH)<sub>2</sub>/CaO.” *International Journal of Energy Research* 41:1004–1013. <https://doi.org/10.1002/er.3688>.
6. W. Wang, O. Kolditz, T. Nagel. 2017. “Parallel finite element modelling of multi-physical processes in thermochemical energy storage devices.” *Applied Energy* 185:1954–1964. <https://doi.org/10.1016/j.apenergy.2016.03.053>.

## **Chapter 5 Preliminary Pilot-Scale Study and Techno-Economic Analysis of Chemical Heat Pump**

### **5.1 Objective**

There have been very few studies focusing on the economic feasibility of ChHPs because of low technology readiness level (TRL) of the system. The development of a SMR involves significantly less upfront money, resulting in lower financial risks and making it a viable alternative to large nuclear reactors (1 GW). An SMR can also combine with an integrated energy system to manage fluctuations in intermittent renewable energy generation while also storing energy or providing electricity/heat. The environmental benefits of SMR-heat pump systems over using fossil fuels for process heating are readily apparent. However, the economics of the system needs to be assessed in order to decide whether the system is a viable investment. The two main objective of this study were: the pilot-scale study for 25-,100, and 1000- kW ChHP and techno-economic analysis of a coupled SMR-ChHP system. This study focuses on economic feasibility of an SMR by selling electricity and nuclear hybrid energy system (NHES) i.e., SMR coupled with ChHP system by selling a combination of heat and electricity. For the techno-economic analysis, the average selling price of electricity and natural gas (for heat) for six different U.S regions are used. The ChHP specific capital cost was calculated using steady state thermodynamic model as there are no studies presently available which reported the specific cost of  $\text{Ca(OH)}_2/\text{CaO}$  ChHP. The economic viability was compared by estimating the economic indicators such as net present value (NPV), payback period (PBP), discounted cash flow rate of return (DCFR) and levelized cost of energy (LCOE) for SMR and NHES systems.

### **5.2 Scalability Study of Chemical Heat Pump**

Temperature amplification applications of ChHP coupled with nuclear reactor have not been investigated or published at pilot scale in the literature. Furthermore, the coupling of ChHP using different reaction system provides a compelling alternative for achieving the temperature mismatch between nuclear reactor and heat required for industrial applications. The pilot-scale study will yield valuable information on Integrated Nuclear Hybrid Energy Systems consisting of advanced reactors coupled to ChHP, which will be useful in defining the role of the nuclear

energy in future energy systems. Research at the University of Idaho has successfully demonstrated the feasibility of the multiple cycles of  $\text{Ca(OH)}_2/\text{CaO}$  ChHP. Results from the bench-scale experiments will be used for detailed design of pilot-scale setup, which will accurately model the full-scale process. Current challenges will be addressed that include poor heat transfer inside the chemical bed, mitigating any performance degradation by addition of inert in solid reactant, and measuring the flow rate of water vapor accurately as it is much easier to measure the flow in pilot scale, as compared with bench scale because of low volume of reactant, which will give us a better understanding of kinetics of the reaction. Experimental and theoretical results at pilot scale will yield valuable information for commercial scale Integrated Nuclear Hybrid Energy Systems, thus supporting missions in enhancing the energy security, and increase the role of nuclear energy in nation's energy system.

### 5.2.1 Literature Review of Pilot-Scale Study

Few studies have been conducted for thermochemical energy storage aspect of the  $\text{Ca(OH)}_2/\text{CaO}$  reaction but not specifically for chemical heat pump by delivering the thermal heat in a continuous operation. Following are the studies focusing on the pilot-scale model for thermochemical energy storage.

#### 5.2.1.1 10 kW Pilot-Scale Reactor

Schmidt et al. [1] focused on hydration-dehydration cycles of indirectly operated reactor in pilot scale (20 kg of powdered  $\text{CaO}$ , particle size  $d_{50} = 5\mu\text{m}$ ). The heat transfer fluid (HTF) used was air and HTF was heated up to  $700^\circ\text{C}$  via electric heaters. The specifications of the reactor are mentioned in Table 5.1.

Table 5.1 Specifications of the reactor

Material (Reactor and Thermoshelves)	1.4404 – X2CrNiMo 17-12-2
Metal weight	145 kg
Reaction bed dimensions	45 L ( $\approx 25$ kg powdered $\text{Ca(OH)}_2$ ) 20 × 200 × 800 mm (10 channels)
Max. permissible temperature	$600^\circ\text{C}$
Max. permissible pressure	Reaction gas side: 0.1–2.5 bar HTF side: 0–5.0 bar
Thermoshelves dimensions	250 × 850 mm (10 channels)

	4.25 m <sup>2</sup> total heat transfer area
Power	P <sub>Nominal</sub> = 5 kW P <sub>max</sub> = 10 kW
HTF mass flow	0.00283-0.0531 kg/s
Operating conditions	Dehydration: Pressure = 10 kPa Temperature = 400–590°C Hydration: Pressure = 200 kPa Temperature = 550°C Total Cycles: 10

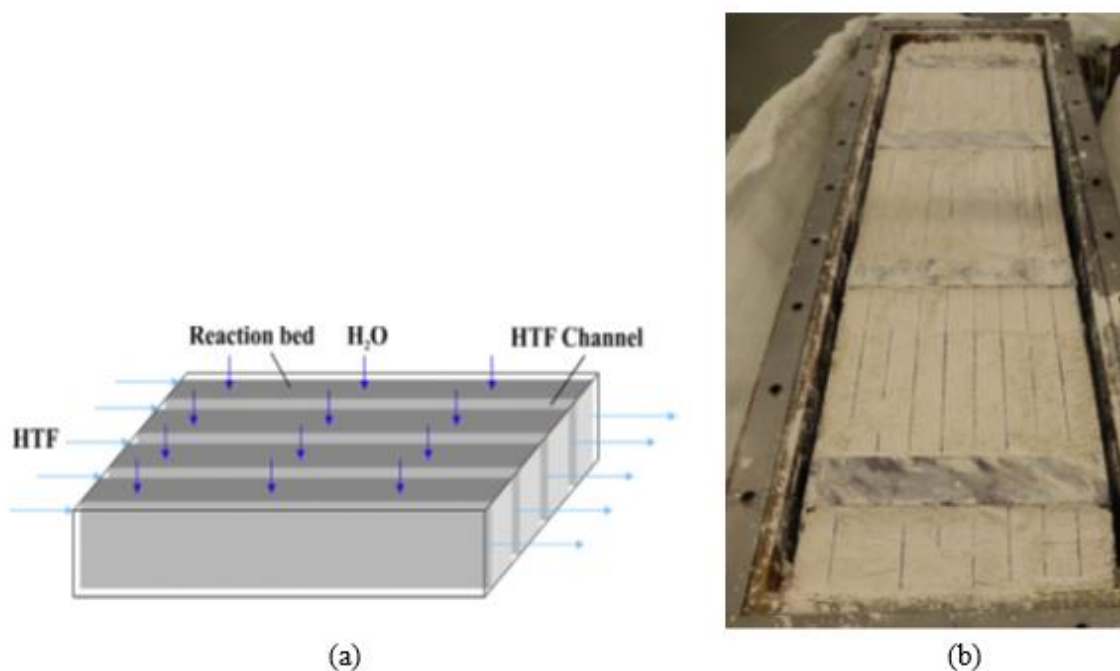


Figure 5.1 (a) Schematic of the cross-flow diagram of the pilot reactor; (b) Reactor filled with 20 kg of Ca(OH)<sub>2</sub> [1]

The cross-flow arrangement between the HTF and the reaction gas allows for sufficient heat exchange area along the length of the reactor while the reaction gas only must overcome a short distance through the reaction bed to the bottom of the reactor, as shown in Fig. 5.1a. The pressure drop over the reaction bed is minimal and a uniform equilibrium temperature over the entire bed volume can be expected. The reactor is filled with a mass of approximately 20 kg of Ca(OH)<sub>2</sub>, as shown in Figure 5.1b.

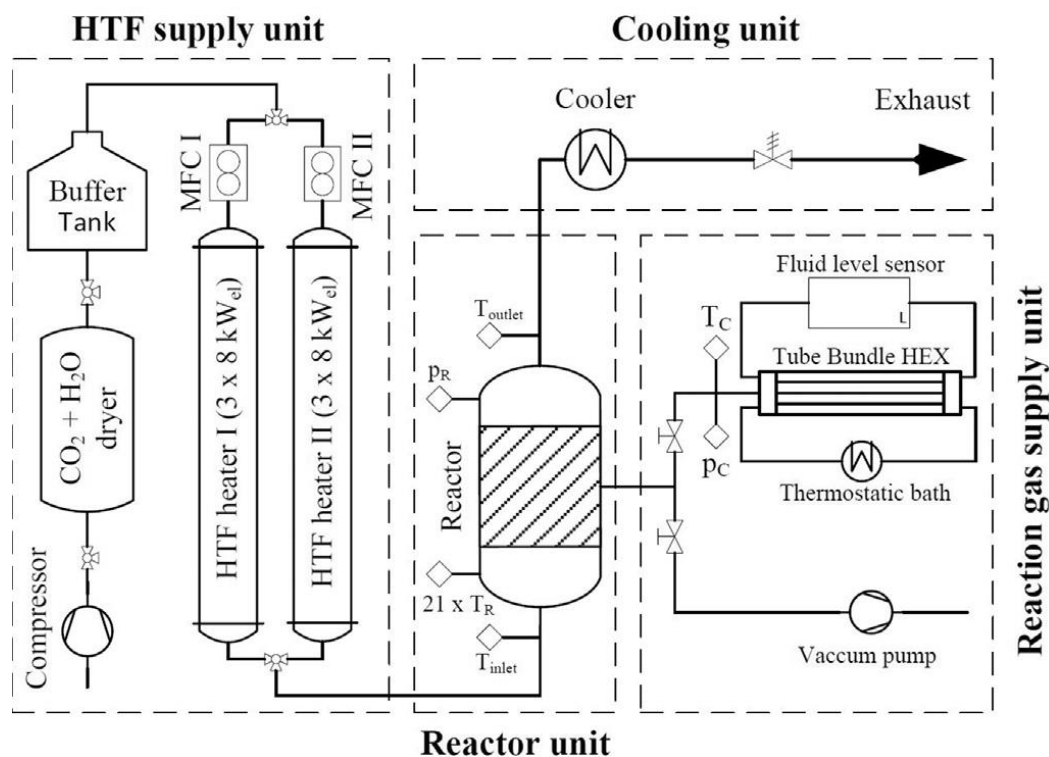


Figure 5.2 Process flow diagram of the test bench [1]

A compressor conveys ambient air with a maximum volume flow of 160 Nm<sup>3</sup>/h at 10 bars. To ensure a continuous availability of the air flow a buffer tank is installed with a capacity of 1 m<sup>3</sup> air and a maximum pressure of 10 bars. The HTF flow can be adjusted in a range of 8 to 160 Nm<sup>3</sup>/h via two mass flow controllers (Bronkhorst, digital flow controller, ±0.5%) at a pressure of up to 5 bar.

For the reaction gas supply an additional evaporator/condenser unit, shown in Fig 5.2, was developed. A tube-bundle heat exchanger with a casing volume of 8.5 l is filled with 2 l of distilled water. A vacuum pump is connected to evacuate the system down to an absolute pressure of 10 mbar to enable a pure water vapor atmosphere. The water level is constantly measured by a fluid level sensor (Vegaflex 65, coaxial measuring probe, ±2 mm).

Similar study was presented by Linder et al. [2], as shown in Fig 5.3, which showed the good agreement between the experimental and simulated results that the reaction kinetics determined in micro-scale measurements as well as the known bed properties offer a sufficient representation of the effective conditions within the bed.

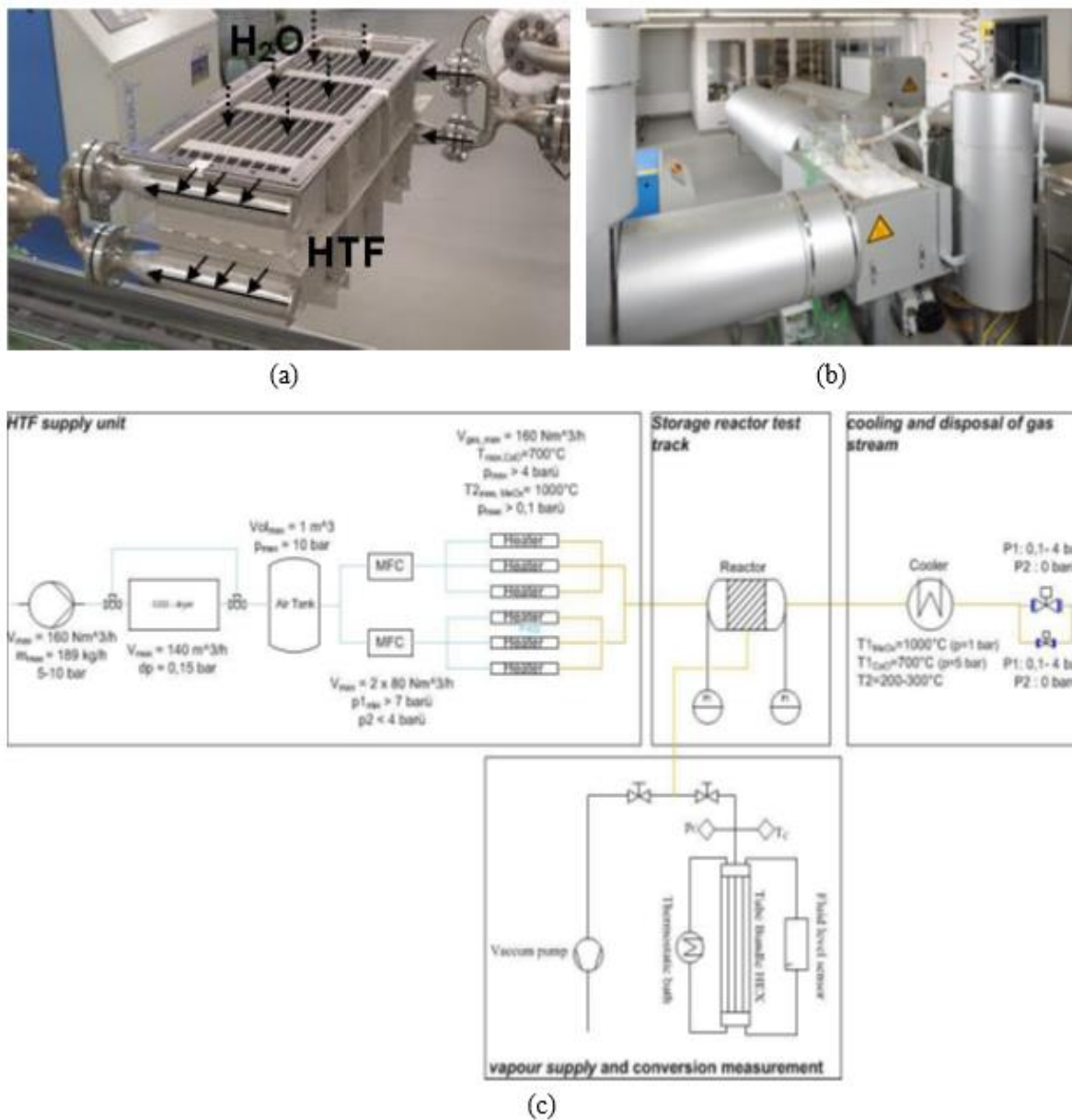


Figure 5.3 (a) Indirectly operated thermochemical storage reactor; (b) multifunctional test bench; (c) process flow diagram of the test bench with integrated indirectly operated reactor [2].

### 5.2.1.2 Design of MW-Scale Thermochemical Energy Storage Reactor

Angerer et al. [3] presented a theoretical study on a novel technical design of a MW-scale thermochemical energy storage reactor for CaO system. The reactor concept features a bubbling fluidized bed with a continuous, guided solid flow and immersed heat exchanger tubes. To investigate the reactor design, a model is build using clustered CSTRs. A fluidized

bed reactor (FBR) was chosen in this work as the most promising reactor concept for large-scale application as shown in Fig 5.4.

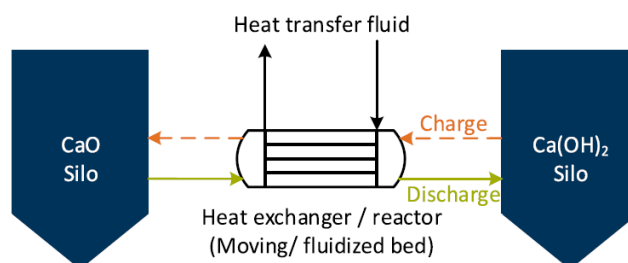


Figure 5.4 Schematic of a thermochemical storage system with separation of power (heat exchanger/reactor) and capacity (silos) [3]

The concept of the design of the reactor is shown in Fig 5.5. The FBR is operated as a dense bubbling bed. A special gas distributor plate with a high number of nozzles is used to distribute the fluidization gas uniformly over the reactor cross section. To improve the residence time distribution, baffles are integrated in the bed leading to a guided flow of solids (powdered reactant) from inlet to outlet.

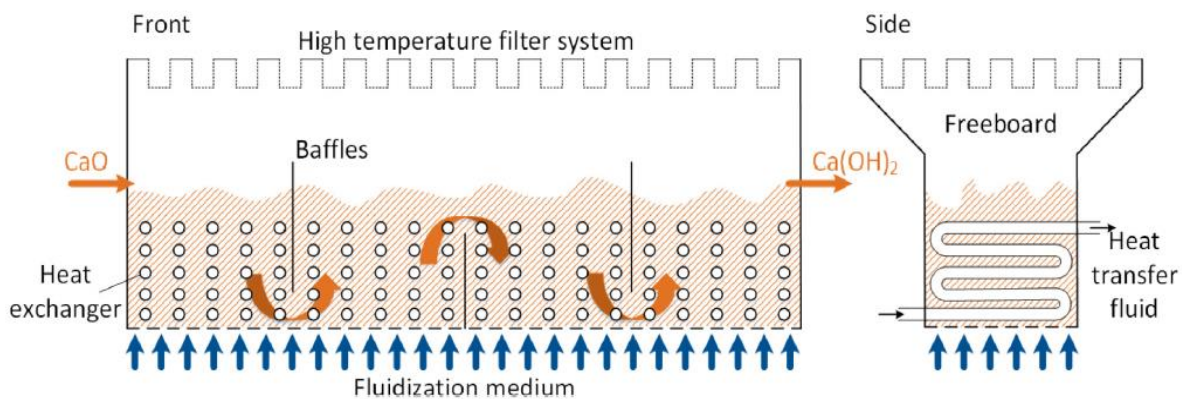


Figure 5.5. Reactor design of a continuous MW-scale FBR for thermochemical energy storage [3]

### 5.2.1.3 Moving Bed Pilot Plant for TCES $\text{CaO}/\text{Ca}(\text{OH})_2$

In this work Schmidt et al. [4] investigated an indirectly heated moving bed concept realized in 10 kW/100 kWh scale. Fig. 5.6a shows the basic design of the heat exchanger. The storage material flows in 158 tubes with an inner diameter of 28 mm. On the shell side of the heat exchanger the HTF air flows in counter-current direction. It enters the reactor at the connection

at the right side and flows around the tubes directed by six baffle plates. The outlet of the HTF leaves the reactor at the opposite side. With an overall heat transfer area of 5 m<sup>2</sup> the heat exchanger is designed to transfer a power of 10 kW at a nominal airflow of 160 Nm<sup>3</sup>/h and a temperature difference between air inlet and outlet of 200 K.

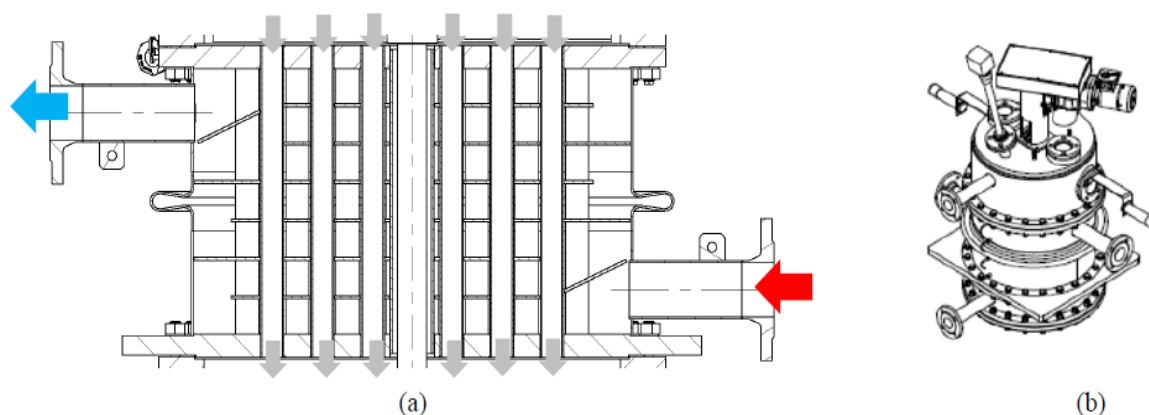


Figure 5.6. (a) Heat exchanger design for moving particles and air; (b) complete reactor design [4]

Fig 5.6b shows the complete reactor consisting of three attachable parts. First part is the top of the reactor where the material inlet is located. In the top is also an additional flange connection where the reaction gas can enter the reactor above the tube bundle. The middle part of the reactor is the heat exchanger. In the bottom of the heat exchanger the outlet area of the reactor is attached. In this part an additional connection is foreseen to supply or remove reaction gas from below the tube bundle. In the flat bottom area, a rotating scraper is installed to move material from the outer tubes to the outlet cross section located in the center.

Fig 5.7 shows the design of the moving bed pilot plant including transport and storage facilities for the material. In the first storage container approximately 270 kg of powdered Ca(OH)<sub>2</sub> material can be stored.

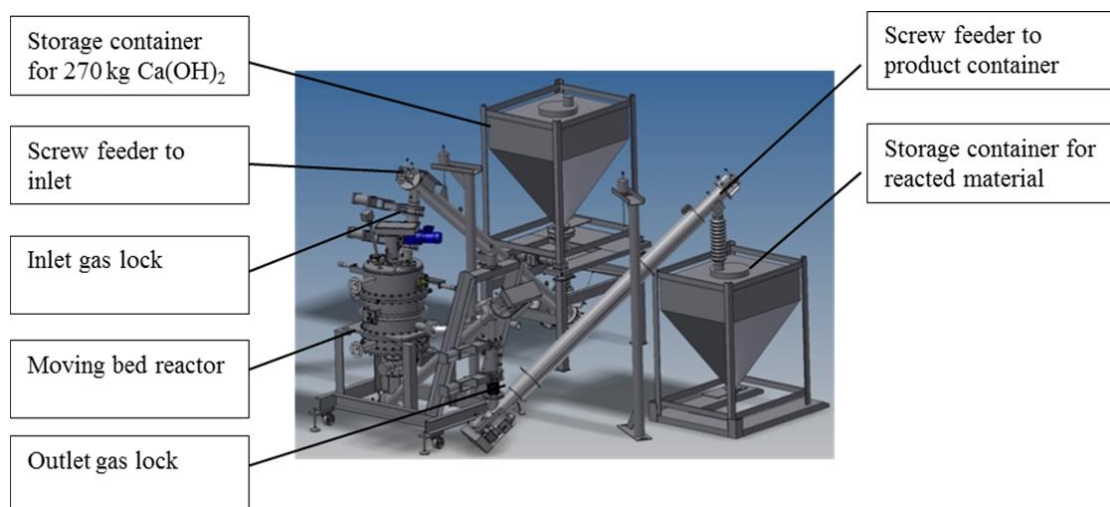


Figure 5.7. Reactor design of a continuous MW-scale FBR for thermochemical energy storage [4]

Fig 5.8 shows the integration of the pilot plant (yellow) into the existing test facility for thermochemical storage systems at DLR. The moving bed reactor is connected to the heat supply unit (green), which can deliver an air flow of  $160 \text{ Nm}^3/\text{h}$  at temperatures up to  $1000^\circ\text{C}$ . Additionally, the two reaction gas inlets of the reactor are connected to the condenser/evaporator unit (blue). With the condenser it is possible to adjust a water vapor atmosphere between 0.1 and 2 bar (10 and 200 kPa) in the reactor. The change of the water level in the condenser is measured giving the level of conversion in the reactor and ten cycles were studied.

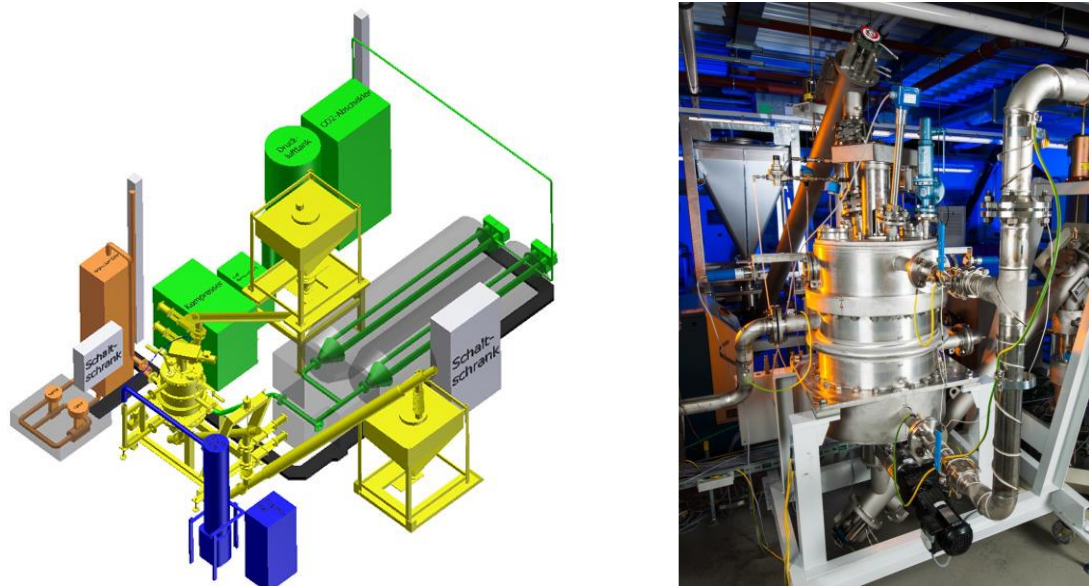


Figure 5.8. Integration scheme of the pilot plant into existing thermochemical test bench at DLR (German Aerospace Center) [4]

#### 5.2.1.4 kW Moving Bed Reactor for TCES

A moving bed reactor for encapsulated storage materials in laboratory scale was developed and set into operation by Mejia et al. [5]. The reactor is designed to operate at pressures between 10 and 150 kPa and a maximum temperature of 550°C (key parameters are summarized in Table 5.2).

Table 5.2. Technical features of the moving bed reactor.

Heat exchanger type	Indirect, tube bundle
Tube diameter	18 mm
Tube length	330 mm
Number of tubes	22
Volume	1.85 l
Heat exchanger area	0.41 m <sup>2</sup>
Thermal power	1 kW
Construction material	Stainless steel 1.4571
Operating Conditions	Dehydration: Pressure = 10 kPa Temperature = 540°C Hydration: Pressure = 100 kPa Temperature = 505°C

Total Cycles: 6
-----------------

The storage material flows inside the tubes, assisted only by gravity as shown in Figure 5.9. Thermal energy is delivered or taken up by the HTF, which flows on the shell side of the heat exchanger directed by baffle plates. These plates ensure a high velocity of the air flow to obtain a good heat transfer coefficient between the gas flow and the tube surface. The length of the tube defines the heat exchange area and the residence time of the reacting material in the tube. The granulated  $\text{Ca}(\text{OH})_2$  was used for experiments of diameters 1–4 mm.

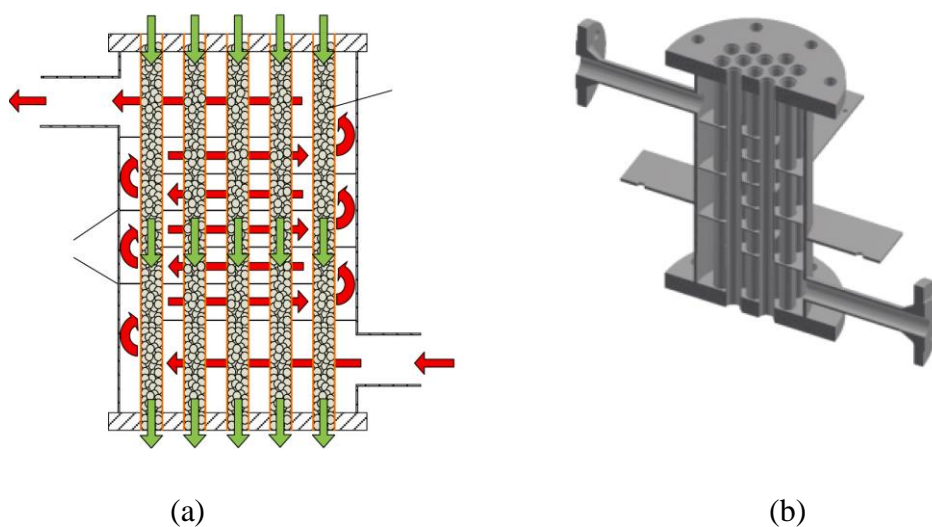


Figure 5.9. (a) Schematic representation of the flow of the HTF and storage material; (b) 3D image of the tube-bundle reactor [5].

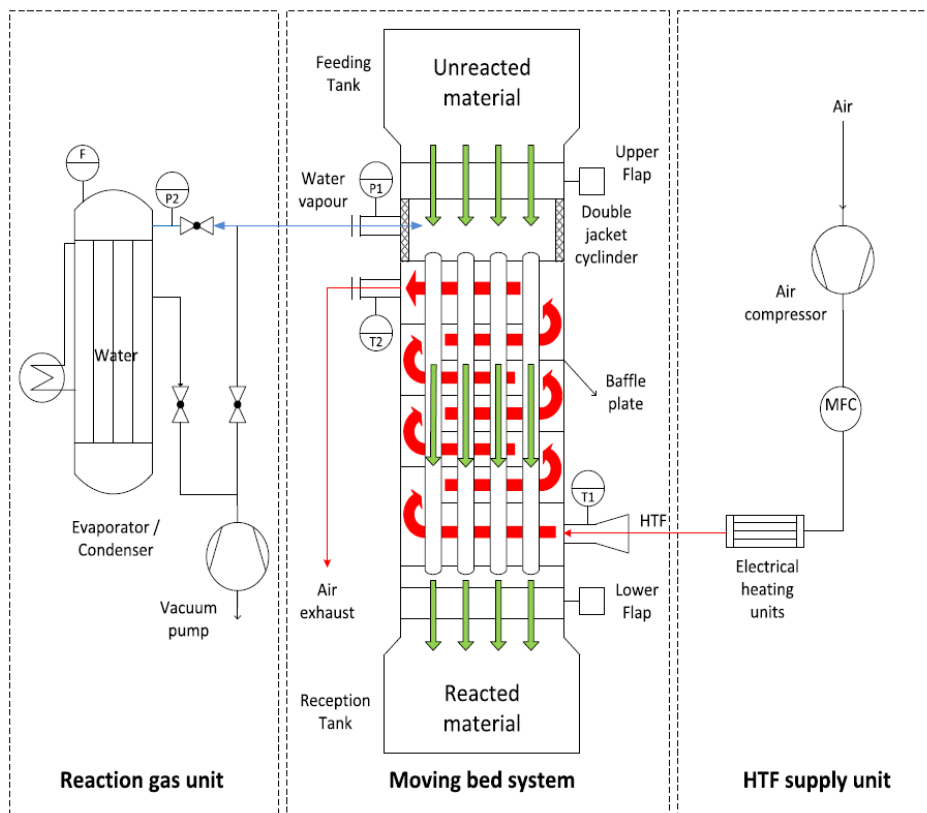


Figure 5.10. Schematics of the moving bed reactor integrated in the test bench [5].

The test bench consists of the moving bed system, the reaction gas unit, and the HTF supply unit as shown in Fig 5.10. Once all the tubes are filled with material, the hydration/dehydration process can start. As soon as the material in the lower part of the tube bundle has reacted completely, the lower flap is opened to allow the material to flow down to the reception tank. By controlling the mass flow in and out of the reactor, the system can be operated as a continuous moving bed, quasi continuous moving bed, or fixed bed, allowing the investigation of such operation modes. The reaction gas unit is composed by the evaporator/condenser, which is equipped with a filling level measurement sensor (Vegaflex 65,  $\pm 2$ mm). The evaporator/condenser supplies water vapor at different pressures and depending on the direction of the reaction occurring in the reactor, the vapor is either taken up or released from the storage material. This causes a pressure change in the system, followed by compensation through further evaporation or condensation of water in the reaction gas unit.

All the studies focused on the indirect heat transfer to transfer heat to/from chemical bed through heat exchangers via HTF. The studies focused on three types of reactors (i.e., fixed

bed, moving bed, and fluidized bed reactors). The some disadvantage of fluidized bed reactor are high pressure drop, poor fluidization because of change in the reaction product mass and density, high potential of attrition and agglomeration of fine particles and large cost when designed for MW systems.

- Due to the low-thermal conductivity of the  $\text{Ca(OH)}_2$  material large storage capacities operated in an indirectly heated fixed bed also require large heat exchangers. One approach was to detach the costly reactor with the heat exchanger (power) from the storage material (capacity) and this can be accomplished by a moving bed concept where the material moves through the reactor.
- In moving bed, the volume of the granules also expanded during the hydration procedure causing clogging in the heat exchanger tubes in the presented reactor. Thus, a free flow of the granules through the reactor after hydration was not achieved yet.
- The fluidized bed concept showed promising MW-scale TCES system claiming that reaction is limited by heat transfer and further research is necessary to identify ideal fluidization conditions to maximize heat transfer while minimizing parasitic losses and improve the storage materials cycling stability and physical properties required for fluidization.

### 5.2.2 Pilot Plant Design

For the pilot-scale study, a two-bed system is considered where one will be dehydrating and other will be hydrating as shown in Fig. 5.11. Once the one bed dehydrates completely will be switched to hydration reaction. The condenser will condense the water vapor coming out during the dehydration reaction. While the evaporator will produce high-pressure steam for hydration process. Both evaporator and condenser will have a mass flow controller to monitor the mass change in the chemical bed to study the kinetics of the reaction. The chemical beds will have several thermocouples and pressure gauges to monitor the temperature and pressure during the reactions, respectively. A storage tank to store the HTF will be connected to a pump. Heaters will be used to heat the HTF. Vacuum pump will be used to ensure there is no trace of impurity within the system and help maintain the sub-atmospheric pressure as well. Cooler will be used to cool down the HTF before storing it in the storage tank. Several temperature readers and pressure gauges will be used to monitor the parameters of interest through the process.

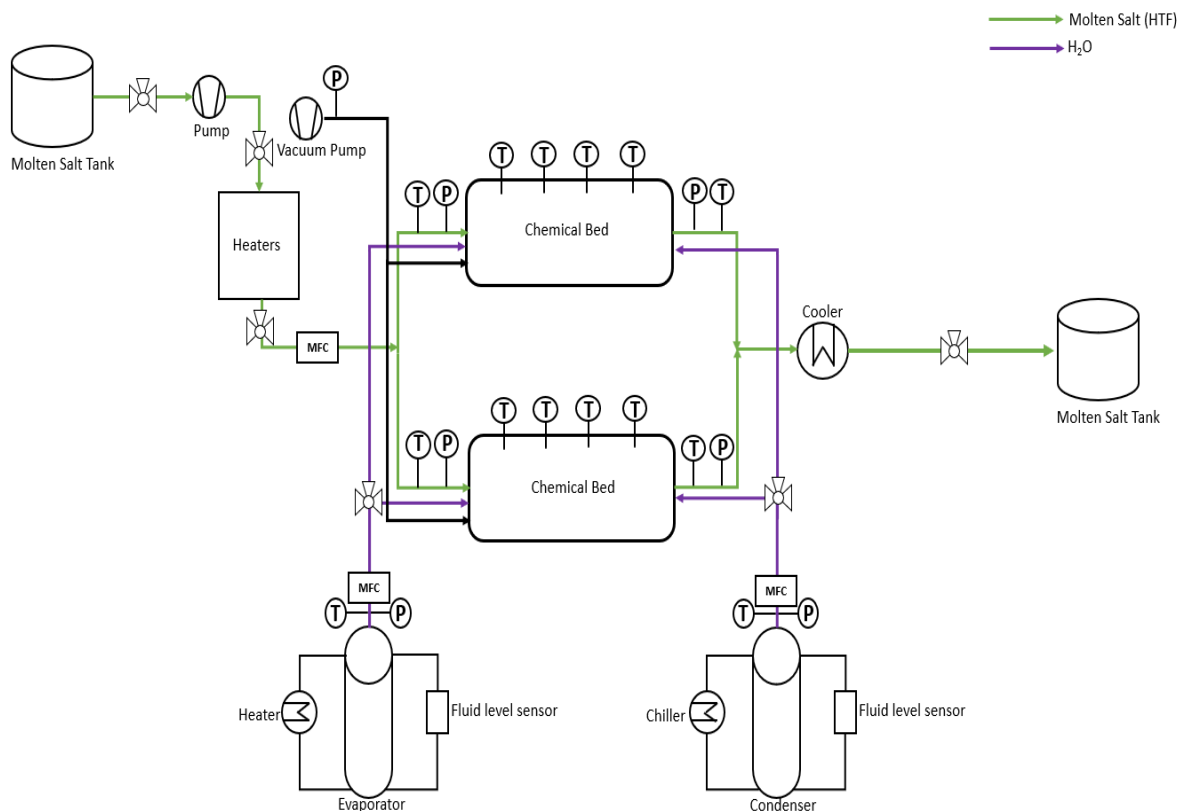


Figure 5.11 Schematics of the pilot-scale ChHP system with two chemical beds

### 5.2.3 Thermal Calculations

For the capital cost of  $\text{Ca}(\text{OH})_2/\text{CaO}$  ChHP, there are no estimates available in literature. A fundamental bottom-up approach for estimation of capital cost is built on based on the chemical bed cost using steady-state thermal model and other facility assumptions. The chemical beds are projected to be the biggest and most costly components in the ChHP system, based on our earlier work by Armatis et al. [6]. To acquire some technical and economic estimates for a big chemical bed design, a quotation from CG Thermal [7] was provided because chemical bed is not effectively represented by heat exchangers or chemical reactor cost curves. The specific cost of chemical bed based on heat transfer is assumed to be ranging from \$400 to \$600/ft<sup>2</sup> as per quotation from CG Thermal [7]. To estimate the specific cost of chemical bed, heat transfer area is estimated by the approach used in our previous work [6]. The system of six unknowns ( $L_{tube}$ ,  $A_{HT}$ ,  $U_{de}$ ,  $U_{hy}$ ,  $\dot{Q}_{de}$ , and  $\Delta T_{hy}$ ) are calculated by six

equations mentioned in Equations 5.1–5.6. Once the heat transfer area is obtained, the chemical cost of the chemical bed can be estimated. The chemical bed volume  $V_{bed}$  is known for the given system size by using the approach from Armatis et al. by knowing the total number of moles and density of the reactant. The  $\dot{Q}_{hy}$  is assumed based on the thermal output of the ChHP.  $\Delta T_{de}$  and  $\Delta T_{hy}$  are defined as the minimal difference between the average CaO/Ca(OH)<sub>2</sub> temperature and the molten salt temperature during dehydration and hydration. The dehydration temperature difference is assumed to be 15.5°C. The bed dimensions are calculated based on the nominal specifications provided by CG Thermal i.e.,  $D_{shell} = 2.9$  m,  $OD_{tube} = 25.4$ mm,  $ID_{tube} = 19.1$  mm and  $n_{tubes}$  ranges from 10 to 550 based on the size of the system.

$$V_{bed} = \left(\frac{\pi}{4}\right) [(OD_{tube} + 2t_{bed})^2 - OD_{tube}^2] n_{tubes} L_{tube} \quad (5.1)$$

$$U_{de} = \left[ \left( \frac{t_{bed}}{k_{bed}} \right) + R_c + \left( \frac{1}{h_{c,de}} \right) \right]^{-1} \quad (5.2)$$

$$U_{hy} = \left[ \left( \frac{t_{bed}}{k_{bed}} \right) + R_c + \left( \frac{1}{h_{c,hy}} \right) \right]^{-1} \quad (5.3)$$

$$\dot{Q}_{de} = U_{de} A_{HT} \Delta T_{de} \quad (5.4)$$

$$\dot{Q}_{hy} = U_{hy} A_{HT} \Delta T_{hy} \quad (5.5)$$

$$A_{HT} = \pi OD_{tube} n_{tubes} L_{tube} \quad (5.6)$$

The schematic of the cross section of a single shell and tube heat exchanger design with chemical bed is shown in Fig. 5.12. The reactant comprising of Ca(OH)<sub>2</sub>/CaO is assumed to be layered around the tube outside in shell section. Most of the volume in shell side will be utilized by the water vapor during dehydration-hydration reactions.

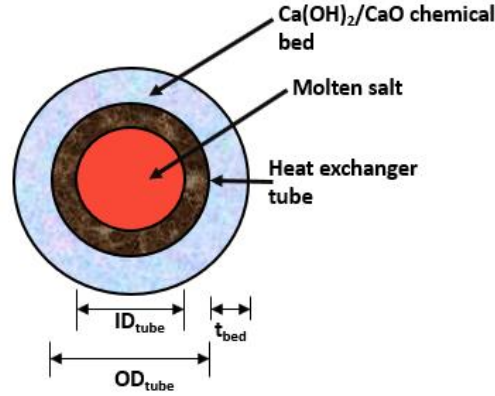


Figure 5.12 Cross-section view of single tube inside

The molten salt convective heat transfer resistance, the CaO/Ca(OH)<sub>2</sub> contact resistance, and the CaO/Ca(OH)<sub>2</sub> conduction resistance are used to estimate the overall heat transfer coefficients for dehydration and hydration reaction. The Dittus-Boelter correlations are used to compute the dehydration and hydration convective heat transfer as shown in Eqs. 5.7–5.11. The heat transport from the reaction steam in the bed via convection and radiation, as well as tube conduction resistance, is assumed negligible. The mass and energy balances of the chemical beds from the system model given above are used to calculate the volume flow rate of the molten salt  $V_f$ . The Nusselt number for dehydration is calculated using Eq. 5.10 and for hydration using Eq. 11. The thermal conductivity of the Ca(OH)<sub>2</sub>/CaO is evaluated between the range of 0.1 to 0.55 W/mK [8] and for this study it is assumed to be 0.5 W/mK. Based on Linder et al. [2] work, the contact resistance  $R_c$  is assumed to be 0.147 m<sup>2</sup>K/kW.

$$h_c = \frac{Nu \cdot k_f}{ID_{tube}} \quad (5.7)$$

$$Re = \frac{\rho_f ID_{tube} u_b}{\mu_f} \quad (5.8)$$

$$u_f = \frac{\dot{V}_f}{\left(\frac{\pi}{4}\right) ID_{tube}^2 n_{tubes}} \quad (5.9)$$

$$Nu = 0.0265 Re^{4/5} Pr^{0.3} \quad (5.10)$$

$$Nu = 0.0243 Re^{4/5} Pr^{0.4} \quad (5.11)$$

$$cost_{bed} = A_{HT} n_{bed} bed_{s,cost} \quad (5.12)$$

After solving for heat transfer area required for a single bed, the total capital cost of the ChHP chemical bed can be calculated by using the Eq. 5.12, where  $n_{bed}$  is number of total chemical bed and  $bed_{s,cost}$  specific cost of bed based on heat transfer area ( $\$/m^2$ ), which is assumed to be \$4,305  $\$/m^2$  CG Thermal [7]. Based on the thermal model, the heat transfer areas are calculated for three different scales (25-, 100-, and 1000-kW) and two different output temperatures (650 and 700°C), which are listed in Table 5.3. The input temperature of ChHP plays an important role and two input temperatures were considered for this study (425 and 450°C). The area required for 425°C is almost double compared with at 450°C because of slow reaction kinetics of Ca(OH)<sub>2</sub>/CaO system at 425°C.

For pilot-scale study, the main contributor to the capital cost of the ChHP is the chemical beds. ChHP capital cost is assumed to be 90% of the total purchased cost of the equipment and other cost includes condenser, evaporator, and pump cost with is assumed to be within the 10% of the total purchased cost. The purchase price of the equipment is only a percentage of the entire investment and other costs are involved in the construction of a facility, which are summarized in Table 5.4. The total capital investment can be calculated using cost estimates for acquired equipment and expected proportions for each category. Based on Perter et al. [9] total capital investments were modified for ChHP system and were adjusted for the total sum to be 100%.

Table 5.3 Pilot-scale process parameters

Heat Transf. Fluid Temp.		Bed Temp.		Heat Output	Single Bed Heat Transfer Area	No. of Tubes	Length of Tubes	Bed Thickness	Cost of Chemical Bed (2 beds)	Other Equipment Cost (Condenser, Storage Tank, Heaters)	Total Equipment Cost
Dehydration	Hydration	Dehydration	Hydration								
°C				kW	m <sup>2</sup>	-	m	mm	\$	\$	\$
425	650	377.5	674.39	1000	219.38	550	4.999	1.938	\$1,901,389.99	\$190,139.0	\$2,091,528.99
425	700	377.5	724.26	1000	223.76	550	5.098	2.005	\$1,939,351.92	\$193,935.1	\$2,133,287.11
450	650	395	680.79	1000	130.99	550	3.985	1.279	\$1,135,304.38	\$113,530.4	\$1,248,834.82
450	700	395	730.48	1000	133.51	550	3.042	1.326	\$1,157,145.49	\$115,714.5	\$1,272,860.04
425	650	380	672.38	100	21.27	40	6.664	1.735	\$184,349.37	\$61,449.79	\$245,799.16
425	700	380	722.28	100	21.702	40	6.799	1.795	\$188,093.56	\$62,697.85	\$250,791.42
450	650	397.5	678.9	100	12.586	40	3.943	1.174	\$109,084.21	\$36,361.40	\$145,445.62
450	700	397.5	728.66	100	12.834	40	4.021	1.216	\$111,233.65	\$37,077.88	\$148,311.54
425	650	380	672.38	25	5.317	10	6.644	1.73	\$46,083.01	\$15,361.00	\$61,444.01
425	700	380	722.28	25	5.426	10	6.928	1.73	\$47,027.72	\$15,675.91	\$62,703.63
450	650	397.5	678.9	25	3.146	10	3.943	1.174	\$27,266.72	\$9,088.91	\$36,355.63
450	700	397.5	728.66	25	3.208	10	4.021	1.216	\$27,804.08	\$9,268.03	\$37,072.11

Table 5.4 Total capital investment for ChHP pilot-scale system

		kW		25				100				1000			
		Input Temperature (°C)		425		450		425		450		425		450	
		Output Temperature (°C)		650	700	650	700	650	700	650	700	650	700	650	700
FCI %		FCI %	adj												
50	Purchased Equipment	46.2963	\$61,444.0 <sub>1</sub>	\$62,703.6 <sub>3</sub>	\$36,355.6 <sub>6</sub>	\$37,072.1 <sub>1</sub>	\$245,799.1 <sub>1</sub>	\$250,791.4 <sub>4</sub>	\$145,445.6 <sub>6</sub>	\$148,311.5 <sub>5</sub>	\$2,091,528.9 <sub>9</sub>	\$2,133,287.1 <sub>1</sub>	\$1,248,834.8 <sub>8</sub>	\$1,272,860.0 <sub>0</sub>	
10	Equipment Installation	9.259259	\$12,288.8 <sub>0</sub>	\$12,540.7 <sub>3</sub>	\$7,271.1 <sub>3</sub>	\$7,414.4 <sub>2</sub>	\$49,159.8 <sub>3</sub>	\$50,158.2 <sub>8</sub>	\$29,089.1 <sub>2</sub>	\$29,662.3 <sub>1</sub>	\$418,305.80	\$426,657.42	\$249,766.96	\$254,572.01	
6	Instrumentation	5.555556	\$7,373.28	\$7,524.44	\$4,362.6 <sub>8</sub>	\$4,448.6 <sub>5</sub>	\$29,495.9 <sub>0</sub>	\$30,094.9 <sub>7</sub>	\$17,453.4 <sub>7</sub>	\$17,797.3 <sub>8</sub>	\$250,983.48	\$255,994.45	\$149,860.18	\$152,743.20	
8	Piping	7.407407	\$9,831.04	\$10,032.5 <sub>8</sub>	\$5,816.9 <sub>0</sub>	\$5,931.5 <sub>4</sub>	\$39,327.8 <sub>7</sub>	\$40,126.6 <sub>3</sub>	\$23,271.3 <sub>0</sub>	\$23,729.8 <sub>5</sub>	\$334,644.64	\$341,325.94	\$199,813.57	\$203,657.61	
3	Electrical	2.777778	\$3,686.64	\$3,762.22	\$2,181.3 <sub>4</sub>	\$2,224.3 <sub>3</sub>	\$14,747.9 <sub>5</sub>	\$15,047.4 <sub>8</sub>	\$8,726.74	\$8,898.69	\$125,491.74	\$127,997.23	\$74,930.09	\$76,371.60	
2	Buildings	1.851852	\$2,457.76	\$2,508.15	\$1,454.2 <sub>3</sub>	\$1,482.8 <sub>8</sub>	\$9,831.97	\$10,031.6 <sub>6</sub>	\$5,817.82	\$5,932.46	\$83,661.16	\$85,331.48	\$49,953.39	\$50,914.40	
2	Yard Improvements	1.851852	\$2,457.76	\$2,508.15	\$1,454.2 <sub>3</sub>	\$1,482.8 <sub>8</sub>	\$9,831.97	\$10,031.6 <sub>6</sub>	\$5,817.82	\$5,932.46	\$83,661.16	\$85,331.48	\$49,953.39	\$50,914.40	
8	Service Facilities	7.407407	\$9,831.04	\$10,032.5 <sub>8</sub>	\$5,816.9 <sub>0</sub>	\$5,931.5 <sub>4</sub>	\$39,327.8 <sub>7</sub>	\$40,126.6 <sub>3</sub>	\$23,271.3 <sub>0</sub>	\$23,729.8 <sub>5</sub>	\$334,644.64	\$341,325.94	\$199,813.57	\$203,657.61	
1	Land	0.925926	\$1,228.88	\$1,254.07	\$727.11	\$741.44	\$4,915.98	\$5,015.83	\$2,908.91	\$2,966.23	\$41,830.58	\$42,665.74	\$24,976.70	\$25,457.20	
5	Engineering and Supervision	4.62963	\$6,144.40	\$6,270.36	\$3,635.5 <sub>6</sub>	\$3,707.2 <sub>1</sub>	\$24,579.9 <sub>2</sub>	\$25,079.1 <sub>4</sub>	\$14,544.5 <sub>6</sub>	\$14,831.1 <sub>5</sub>	\$209,152.90	\$213,328.71	\$124,883.48	\$127,286.00	
5	Construction Expenses	4.62963	\$6,144.40	\$6,270.36	\$3,635.5 <sub>6</sub>	\$3,707.2 <sub>1</sub>	\$24,579.9 <sub>2</sub>	\$25,079.1 <sub>4</sub>	\$14,544.5 <sub>6</sub>	\$14,831.1 <sub>5</sub>	\$209,152.90	\$213,328.71	\$124,883.48	\$127,286.00	
1	Legal Expenses	0.925926	\$1,228.88	\$1,254.07	\$727.11	\$741.44	\$4,915.98	\$5,015.83	\$2,908.91	\$2,966.23	\$41,830.58	\$42,665.74	\$24,976.70	\$25,457.20	
2	Contractor's Fee	1.851852	\$2,457.76	\$2,508.15	\$1,454.2 <sub>3</sub>	\$1,482.8 <sub>8</sub>	\$9,831.97	\$10,031.6 <sub>6</sub>	\$5,817.82	\$5,932.46	\$83,661.16	\$85,331.48	\$49,953.39	\$50,914.40	
5	Contingency	4.62963	\$6,144.40	\$6,270.36	\$3,635.5 <sub>6</sub>	\$3,707.2 <sub>1</sub>	\$24,579.9 <sub>2</sub>	\$25,079.1 <sub>4</sub>	\$14,544.5 <sub>6</sub>	\$14,831.1 <sub>5</sub>	\$209,152.90	\$213,328.71	\$124,883.48	\$127,286.00	
<b>108</b>		<b>100</b>													
	<b>Total FCI (\$)</b>		\$132,719.0	\$135,439.8	\$78,528.1	\$80,075.7	\$530,926.1	\$541,709.4	\$314,162.5	\$320,352.9	\$4,517,702.6	\$4,607,900.1	\$2,697,483.2	\$2,749,377.6	

### 5.3 Techno-Economic Analysis

Techno-economic Analysis (TEA) is a methodology framework utilized to analyze the technical and economic performance of a process, product, or service and “includes studies on the economic impact of research, development, demonstration, and deployment of technologies” quantifying the cost of manufacturing and market opportunities. TEA combines process modeling and engineering design with economic evaluation. It helps to assess the economic viability of a process and provides direction to research, development, investment, and policy making. To study the techno-economic feasibility of the system, the economic parameters are evaluated such as NPV, payback period (PBP), DCFR, and LCOE as described in the subsequent sections.

#### 5.3.1 Methodology

The general methodology used to assess the techno-economic feasibility of a system is shown in Fig. 5.13. The first stage is to estimate the capital costs of the system. In next step, possible market and utility factors are evaluated. Finally, the necessary economic parameters are calculated to determine the techno-economic feasibility of the system or project. This section will focus on the evaluation of economic parameters, specific capital cost, and baseline schematic of ChHP with SMR.

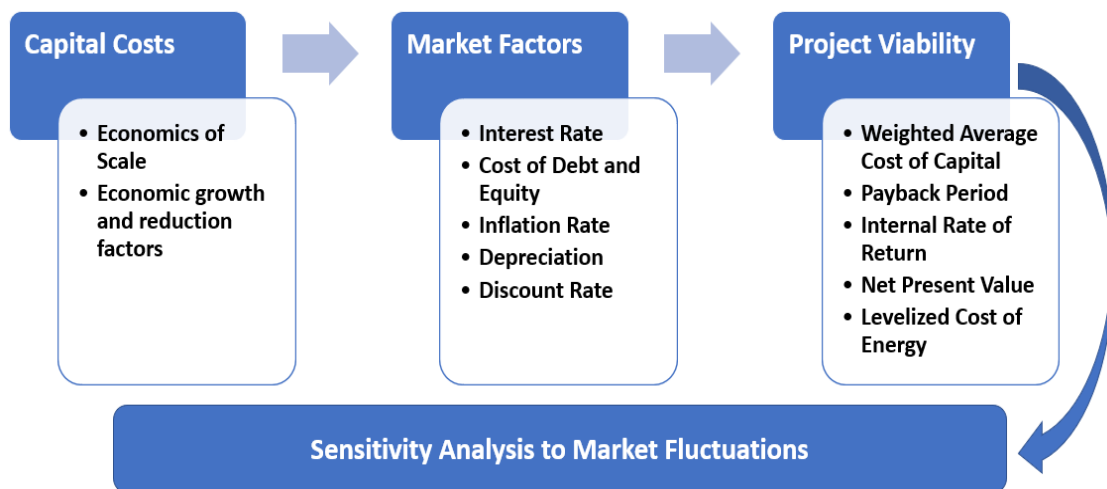


Figure 5.13 Overview of economic analysis methodology

Once the capital costs are calculated for a particular SMR project, it is necessary to assess the market conditions and project viability. This is done by analyzing investment risks and

determining the IRR, NPV, and LCOE for comparison to the weighted average cost of capital (WACC) and expected electricity prices.

### **5.3.1.1 Baseline ChHP Coupled SMR System**

The schematic of the baseline model used in this study is shown in Fig. 5.14 where ChHP is integrated with advanced SMR to deliver heat to high-temperature thermal industrial processes. This flow sheet shows the major components of the techno-economic model. The system uses thermal energy from the advanced SMR via molten salt as HTF and deliver it to chemical bed, which contains  $\text{Ca}(\text{OH})_2$  for dehydration process. In dehydration bed,  $\text{Ca}(\text{OH})_2$  decomposes into  $\text{CaO}$  in an endothermic reaction liberating water vapor. The molten salt returns from the dehydration bed and is reheated in a closed loop. The liberated water vapor from the dehydration bed is condensed in the condenser. At the same time a high-pressure steam from the evaporator is pumped to the Chemical Bed 2, which reacts with  $\text{CaO}$  to form  $\text{Ca}(\text{OH})_2$  in an exothermic reaction. This is a hydration step and the temperature in the hydration bed is higher than temperature in dehydration bed. According to Clausius-Clapeyron equilibrium relation, higher pressure dictates the higher temperature. The heat from the hydration bed is removed using molten salt, which is sent to the high-temperature thermal industrial processes. This salt is again sent back to the hydration bed. This process is continuous; and once the bed is dehydrated, it is ready for hydration and vice-versa.

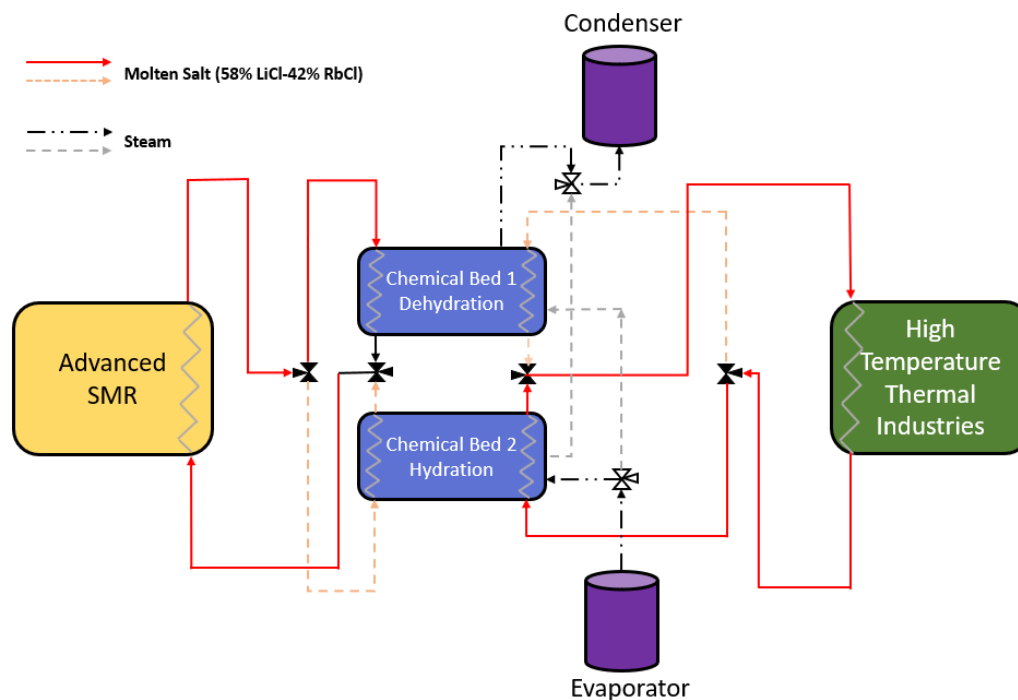


Figure 5.14 Schematic of ChHP coupled with SMR system

The study focuses on advanced SMR with a thermal output of  $100 \text{ MW}_{\text{th}}$  is assumed and a temperature output of  $400^\circ\text{C}$ . The dehydration occurs at  $380^\circ\text{C}$ , and during hydration the molten salt temperature reaches to  $650^\circ\text{C}$  for this study. The conventional light water SMR operates at  $300\text{--}325^\circ\text{C}$ , making the reaction kinetics slow because of that reason dehydration temperature assumed in this study is slightly higher.

### 5.3.1.2 Assessment of Capital Cost of System

The estimation of advanced SMR cost and ChHP are both required for TEA of the system. Many studies have reported the capital cost of the advanced SMR. Sabharwall et al. [10] estimated the overnight capital cost (OCC) of SMR of  $\$4,637/\text{kW}_e$ . Richards et al. [11] estimated the overnight specific capital cost of the molten salt reactors between  $\$2,000$  to  $\$3,846/\text{kW}_e$ . A study conducted by MIT [12] assessed the OCC for NOAK reactors between  $\$3,797$  to  $\$6,880/\text{kW}_e$  based on a different design. FOAK SMRs OCCs were projected with 10<sup>th</sup>-of-a-Kind estimates in a recent report Stewart et al. [13]. FOAK SMRs can range in price from  $\$4,500$  to  $\$8,500/\text{kW}_e$  depending on the reactor type. After ten reactors, the price range can be reduced to  $\$3,000$   $\$5,000/\text{kW}_e$  as per NOAK model. For this study, an OCC of will be  $\$4,637/\text{kW}_e$  assumed and a parametric study is also conducted assuming OCC ranging from

\$4,500 to \$6,500/kWe. According to Boldon [14], the total specific capital cost can be computed by integrating the contingency cost rate, detailed design, and engineering cost rate and the overnight capital cost, as shown in Eq. 5.13. For this study, both the cost rates (contingency cost and detailed design and engineering) were assumed to be 5%.

$$TSCC = OCC(CC + DD\&E + 1) \quad (5.13)$$

### 5.3.1.3 Payback Period

The payback period (PBP) is the length of time required to recoup the funds expended in an investment, or to reach the break-even point and is calculated using the following Eqs. 5.14–5.16 where  $PBP$  is the payback period,  $V$  denotes the fixed capital investment,  $\bar{A}$  denotes the average yearly cash flow over the project's lifetime,  $A$  is the annual cash flow or annuity,  $N$  denotes the project's length in years,  $s$  represents sales,  $c_o$  represents cost,  $d$  represents depreciation,  $\Phi$  represents the corporation tax rate, and  $j$  denotes a specific year [9].

$$PBP = \frac{V}{\bar{A}} \quad (5.14)$$

$$\bar{A} = \frac{1}{N} \sum_{j=1}^N A_j \quad (5.15)$$

$$A_j = (s_j - c_{o,j} - d_j)(1 - \Phi) + d_j \quad (5.16)$$

Compounding and discounting effects do not apply in this calculation since the payback period does not include the time worth of money. If a proposed investment's payback period is smaller than or equal to that of an existing solution for the same application, it may be worthwhile to pursue. If not, more investigation is required.

The concept of depreciation  $d$  is based upon the fact that physical facilities deteriorate and decline in usefulness with time, thus decreasing the values of the facility. There are several ways to estimate the depreciation rate, but the Modified Accelerated Cost Recovery System (MACRS) is used in this study. With MACRS, a recovery period is selected based on the type of facility and a correlation is applied. These rates are based on average recovery period by IRS 2021 [15]. For power plants, a 15-year recovery period is commonly assumed [9].

In this study, the advanced SMR system produce and sells electricity and the combined advanced SMR and ChHP produce and sell both thermal energy and electricity at natural gas and electricity prices, respectively. The cost of selling thermal (heat) energy also account for

carbon tax with natural gas prices. The sales income will be different for above explained cases. For the electricity-only case, the annual sales are evaluated using the Eq. 5.17. The assumptions used in this study for heat engine efficiency ( $\eta$ ) to produce electricity is 34%. The capacity factor ( $CF$ ) is assumed to be 90% based on Sabharwall et al. [10] study.  $\dot{Q}_{SMR}$  is the nominal heat generated by the advanced SMR and  $SP_e$  is the selling price of electricity.

$$S_{j,SMR} = \eta \cdot CF \cdot \dot{Q}_{SMR} \cdot SP_e \cdot 8760 \text{ hrs} \quad (5.17)$$

For the combined advanced SMR-ChHP system, which provides and sell both electricity and heat to the market, a carbon tax was added to the natural gas prices to estimate the selling price of heat. The annual sales for the combined advanced SMR-ChHP system are given by Eq. 5.18 where  $SP_{ht}$  is the selling price of heat (combined natural gas and carbon tax prices),  $\dot{Q}_{ChHP,in}$  is the heat rate from SMR to ChHP and  $\dot{Q}_{ChHP,out}$  is the rate of thermal out energy from ChHP.

$$S_{j,SMR-ChHP} = \left( (\eta \cdot CF \cdot (\dot{Q}_{SMR} - \dot{Q}_{ChHP,in}) \cdot SP_e) + (CF \cdot \dot{Q}_{ChHP,out} \cdot SP_{ht}) \right) \cdot 8760 \text{ hrs} \quad (5.18)$$

The annual costs are calculated using the Eq. 5.19 where the specific and fixed cost of operation and maintenance for the advanced SMR are represented by  $O\&M_{spec}$  and  $O\&M_{fix}$ , respectively. The specific fuel cost the uranium is represented by  $Fuel_{spec}$ . The values assumed for this study will be described in detail in Section 5.3.2. for different cases and scenarios.

$$c_0 = CF \cdot \dot{Q}_{SMR} \cdot (O\&M_{spec} + Fuel_{spec}) \cdot 8760 \text{ hrs} + O\&M_{fix} \cdot 1 \text{ yr} \quad (5.19)$$

#### 5.3.1.4 Net Present Value

Net present value (NPV) also known as net present worth is the difference between the present value of cash inflows and the present value of cash outflows over the lifetime of the plant [9]. The “present” year identification is fairly arbitrary, and we chose the first year of the plant operation to be present. NPV accounts for the time value of money and is estimated using the following Eq. 5.20.

$$NPV = \sum_{j=1}^N PWF_{cf,j} (A_j + rec_j) - \sum_{k=1}^{Nc} PWF_{v,k} T_k \quad (5.20)$$

$$PWF_{cf,j} = (1 + i)^{-j} \quad (5.21)$$

$$PWF_{v,j} = (1 + i)^{Nc-j} \quad (5.22)$$

The  $rec$  is the cost recovered from salvaged components, and  $T$  is the investment cost,  $N_c$  is the construction time in years. Eq. 5.21 represents the present worth factor for the annual cash flows. This factor discounts future cash flows where  $I$  is the discount rate. The same rate,  $I$  can be assumed for the present worth factor in Eq. 5.22, which compounds past investments. Both factors adjust the value of the money from past or future value to the present value. The cost recovered was assumed to be zero for this analysis.

$$i = \frac{WACC+1}{r_{inf}+1} - 1 \quad (5.23)$$

The discount rate  $I$  is an interest rate that provides the current worth of future money, as shown in Eq. 5.23 from Boldon [14]. A nominal discount rate includes inflation, while the real discount rate does not. The assumed inflation rate is expressed as  $r_{inf}$  and  $WACC$  is the weighted average capital cost, calculated in Eq. 5.24. The  $WACC$  is a value describing the percentage of capital that must be paid to the investors, so they see the expected return on investments/assets. The  $WACC$  may be affected by many factors, such as political and financial risks. The  $C_d$  and  $C_{eq}$  representing the rate charged for costs of capital and equity, respectively.  $P_d$  and  $p_{eq}$  representing the portions of debt and equity for the project.

$$WACC = (p_d \times C_d) + (p_{eq} \times C_{eq}) \quad (5.24)$$

The portion of debt and charge rate of debt were assumed for the analysis. The portion of equity is just the portion left over that was not financed ( $1-p_d$ ). The rate charged for cost of equity is evaluated using the Eq. 5.25 from Boldon [14], where  $\Phi$  is the corporate tax rate that is assumed.

$$C_E = C_D(1 - \Phi) \quad (5.25)$$

The construction period of 3 years was assumed and construction schedule for advanced SMR was assumed to be 60%, 20%, and 20% for 1<sup>st</sup>, 2<sup>nd</sup>, and 3<sup>rd</sup> year respectively based on study by Alonso et al. [16]. ChHP construction schedule is assumed to be 0%, 20%, and 80% for 1<sup>st</sup>, 2<sup>nd</sup>, and 3<sup>rd</sup> year respectively. The project is not considered profitable if the net present worth is negative. In making the comparisons of the investments, the larger the NPV, the more favorable is the investment.

### 5.3.1.5 Discounted Cash Flow rate of Return

The DCFR also known as internal rate of return is the return on investment while considering the time value of money. It is obtained from an investment in which all the investment and cash flow are discounted [9]. The DCFR is estimated by making the net present worth equal to zero and solving for the rate used in the present worth factors using Eq. 5.26. If the DCFR exceeds the WACC, the project is considered profitable.

$$0 = \sum_{j=1}^N [(1 + DCFR)^{-j}] (A_j + rec_j) - \sum_{k=1}^{N_c} [(1 + DCFR)^{N_c - k}] T_k \quad (5.26)$$

### 5.3.1.6 Levelized Cost of Energy

The levelized cost of energy is the average cost of energy (\$/MW-h or ¢/kW-h) produced over the lifetime of the plant and is calculated using Eq. 5.27, where  $E_j$  is the energy produced each year. For this study, the LCOE is the combined cost of total electricity and thermal energy produced. It is also defined as “the discounted lifetime cost of ownership and usage of a generation asset, transformed into a \$/MWh equivalent unit of cost of generation.” The energy produced is discounted in LCOE calculations [17]. When comparing different investments or technologies, LCOE is best tool to employ as it measures the competitiveness of the technology. Less-competitive technology is assessed by a higher value of LCOE.

$$LCOE = \frac{\sum_{j=1}^N PWF_{cf,j}(C_{o,j}) + \sum_{k=1}^{N_c} PWF_{v,k} T_k}{\sum_{j=1}^N PWF_{cf,j} E_j} \quad (5.27)$$

### 5.3.2 Study Approach and Assessment Scenarios

To study the TEA of the advanced SMR and SMR combined with ChHP, the utility data were assumed from U.S. Energy Information Administration [18] for six different regions (California, Northwest, Midwest, Southwest, New England, and PJM) of United States as shown in Table 5.5. The values were averaged for industrial gas prices and electricity data for the year 2021.

Table 5.5 Utility data for different regions

Region	2021 Industrial Natural Gas Price (\$/MMBtu)	2021 Electricity Data (\$/MWh)
California	9.06	66.5
Midwest	6.07	57.7
Northwest	8.15	59.78
New England	9.68	47.75
Southwest	5.62	64.78
PJM	6.67	42.55

For this study, an advanced SMR with a thermal output  $100 \text{ MW}_{\text{th}}$  is assumed. For the TEA, different scenarios are considered based on the different thermal output of ChHP, as shown in Fig. 5.15 for an ideal case ( $\text{CF}=100\%$ ). Scenario 1 is when the  $100 \text{ MW}_{\text{th}}$  advanced SMR sells electricity with a heat engine efficiency of 34% is represented as SMR. Scenario 2 has NHES where a  $100\text{-MW}_{\text{th}}$  advanced SMR is coupled with  $50 \text{ MW}_{\text{th}}$  output ChHP with coefficient of performance of 0.58, which sells heat and rest of the energy from SMR sells electricity and is represented as NHES-1. In Scenario 3, NHES-2 is where the advanced SMR is coupled with  $10 \text{ MW}_{\text{th}}$  output ChHP, which offers heat and the rest of the energy from SMR produces electricity. Scenarios 4 and 5, NHES-3 and NHES-4 includes the advanced SMR coupled with 5 and  $1 \text{ MW}_{\text{th}}$  output ChHP, respectively.

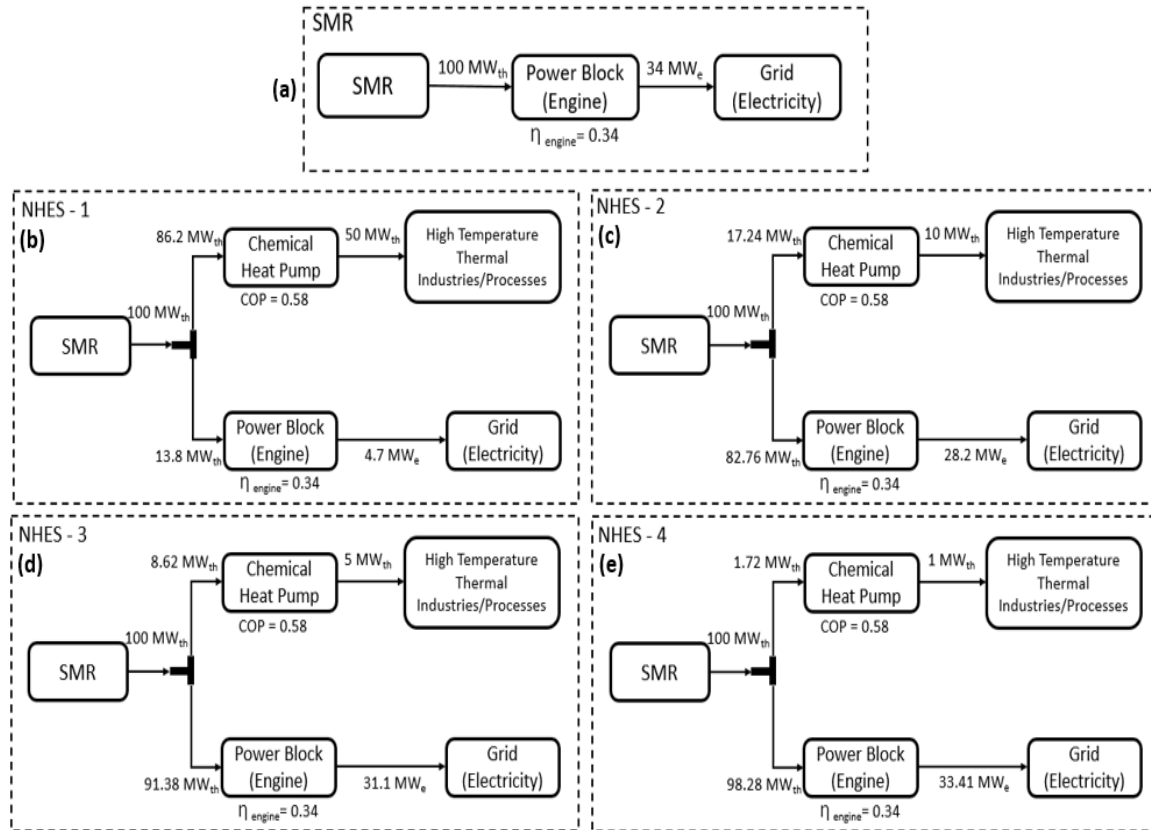


Figure 5.15 Advanced SMR and SMR-ChHP combined scenarios

For conducting the economic analysis, the economic parameters assumed from the literature are listed in Table 5.6. Based on these assumptions and utility prices at different regions, the techno-economic study is conducted to determine the profitable scenarios for the advanced SMR and SMR coupled with ChHP with different thermal output. The economic parameters evaluated are NPV, PBP, DCFR, and LCOE to discover the potential of selling heat from the advanced SMR coupled with ChHP for high-temperature industrial processes. A parametric study based on different OCC of advanced SMR, and carbon taxes is also conducted.

Table 5.6 Parameters assumed for this study

Parameters	Assumed Values	References
Overnight Cap Cost	\$4,637/kW <sub>e</sub>	Sabharwall et al. [10]
Capacity Factor	90%	Sabharwall et al. [10]
Lifetime	60 years	Sabharwall et al. [10], Alonso et al. [16]

Variable O&M Cost	\$0.486/MW <sub>e</sub> -h	Sabharwall et al. [10]
Fixed O&M Cost	\$19,500,000/yr	Sabharwall et al. [10]
Fuel Cost	\$0 (included in O&M)	Sabharwall et al. [10]
Construction Period	3 (60%, 20%, 20%)	Alonso et al. [16]
CO <sub>2</sub> Tax	\$150/tonne	Locatelli et al. [19]
Depreciation	Variable	MACRS Method [15]
Corporate Tax Rate	21%	Nuclear Energy Institute [20]
Inflation Rate	1.1%	MIT report [12]
Cost of Debt	4%	Sabharwall et al. [10]
Debt Portion	30%	Sabharwall et al. [10]

---

#### 5.4 Results and Discussion

In this study, based on the economic input assumptions, the calculated discount rate ( $i$ ) is 3.552%, cost of equity is 4.84%, and WACC is estimated to be 4.588%. ChHP-specific capital cost was estimated as \$4,500/kW based on thermal model for baseline system and the CG Thermal-specific chemical bed cost assumption [7]. These calculated values will be used to determine the economic parameters and profitability of the different scenarios between advanced SMR and SMR-ChHP systems.

### 5.4.1 Economic Parameter Analysis

Based on the utility prices assumed for six different U.S. regions, economic parameters for SMR, NHES-1, NHES-2, NHES-3, and NHES-4 were evaluated, as described in Section 5.3. Fig. 5.16 shows the NPV values of advanced SMR and SMR-ChHP output scenarios. All the NHESs have the higher NPV values than SMR for every region because of higher sales revenue. As per NPV estimates, it is observed that selling heat from NHES-1 with a ChHP thermal out of  $50 \text{ MW}_{\text{th}}$  is most profitable compared with lower thermal output ChHP or selling electricity from  $100 \text{ MW}_{\text{th}}$  advanced SMR. The New England and PJM regions' NPV values of \$162M and \$251.8M show the best case for selling heat for high-temperature industrial processes because of their high natural gas and low electricity prices as per the percentage increase in NPV values compared with SMR in their region.

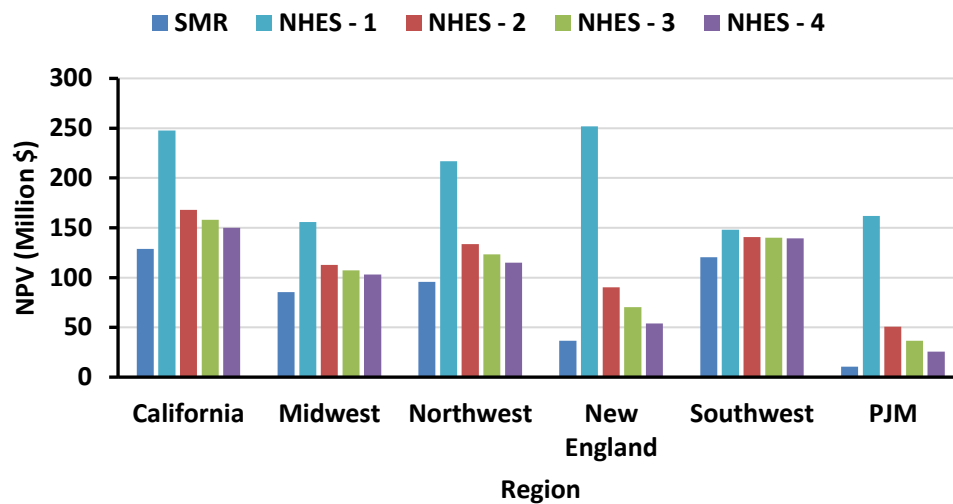


Figure 5.16 NPV values at different regions for SMR and different SMR-ChHP output scenarios

Fig. 5.17 shows the payback period (PBP) of advanced SMR and SMR-ChHP output scenarios and Fig. 5.18 shows the percentage deviation of PBP for different NHES systems from advanced SMR values. The New England and PJM regions showed a shorter payback period of 16.4 and 19.12 years, respectively, for NHES-1 making the most profitable scenario for selling heat at higher scale, whereas for other regions PBP for NHES-1 system were higher. NHES-2, 3, and 4 showed slightly lower PBP from advanced SMR values in the California, Midwest, Northwest, and Southwest regions. NHES-4 is the most profitable case in the California, Midwest, Northwest, and Southwest regions as the PBP period is the lowest among NHES-2 and 3 and advanced SMR asserting that SMR coupled with 1 MW<sub>th</sub> ChHP system providing heat and electricity is always profitable than advanced SMR selling electricity only in terms of PBP calculations. The negative percentage deviation in Figure 5.18 shows the PBP of NHES system is lower than advanced SMR values making system profitable. Except NHES-1 in the California, Southwest, Northwest, and Southwest regions, NHES-2 in the Southwest have positive percentage deviation from SMR values favoring SMR. Even though the ChHP has higher sales income and NPV values, the NPV is computed by making an assumption of 60-year plant life, which means after the capital cost is recovered there are many years to earn a profit.

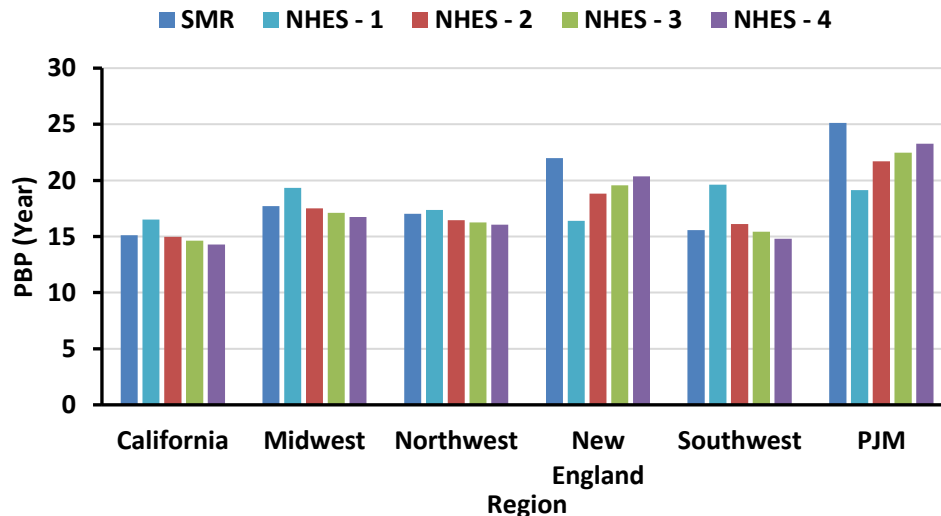


Figure 5.17 PBP at different regions for SMR and different SMR-ChHP output scenarios

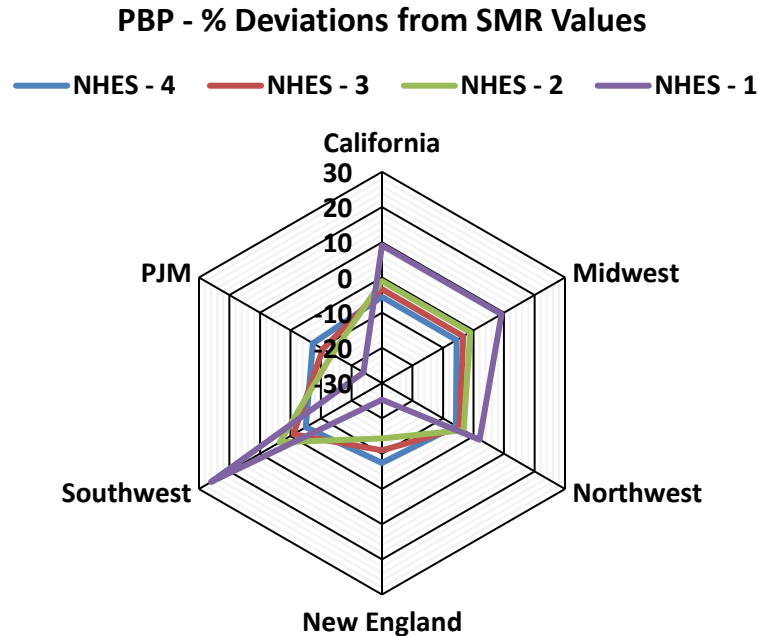


Figure 5.18 Percentage deviation of PBP for different NHES scenarios from SMR values

Fig. 5.19 shows that the DCFR calculations and all the NHES systems have DCFR values greater than WACC, asserting the project is acceptable, which should be compared with other accepted scenarios or projects as per Bolden 2015 [21]. The DCFR values for New England and PJM are significant higher for NHES-1 system compared with advanced SMR making it the most profitable case for selling heat. Figure 5.20 shows the percentage deviation of DCFR for different NHES systems from advanced SMR values. The four cases where DCFR values of NHES systems are less than advanced, the SMR values are California, Midwest, and Southwest for NHES-1 system, and NHES-2 for the Southwest system. The DCFR analysis also confirmed that SMR-ChHP system is always profitable at different regions based on different ChHP thermal output scenarios.

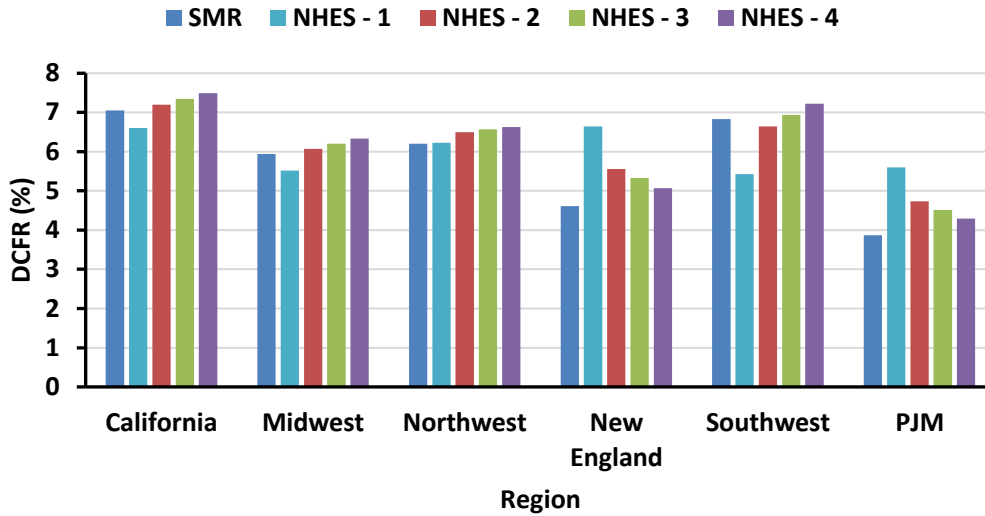


Figure 5.19 DCFR at different regions for SMR and different SMR-ChHP output scenarios

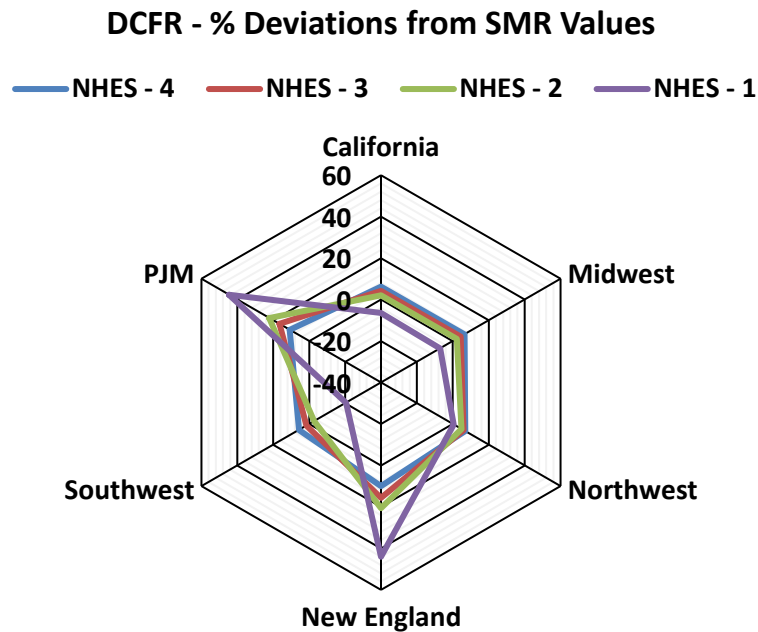


Figure 5.20 Percentage deviation of DCFR for different NHEs scenarios from SMR values

The Fig. 5.21 shows the LCOE values for SMR and NHEs systems for different scenarios. The LCOE for advanced SMR is 36.93 \$/MWh whereas the different coupled SMR-ChHP scenarios have LCOE values 23.85, 36.14, 38.62 and 40.88 \$/MWh for NHEs-1, 2, 3, and 4, respectively. NHEs-1 has lower LCOE when compared to advanced SMR making NHEs-1 a better investment as SMR-ChHP system is producing more energy than advanced SMR and

overcomes the cost of the coupled system well. NHES-2 has slightly higher LCOE value compared to advanced SMR signifying that selling heat and electricity via coupled system balances out the cost of SMR-ChHP. NHES-3 and 4 have higher LCOE as the cost of the system does not balance out the energy produced by the coupled system.

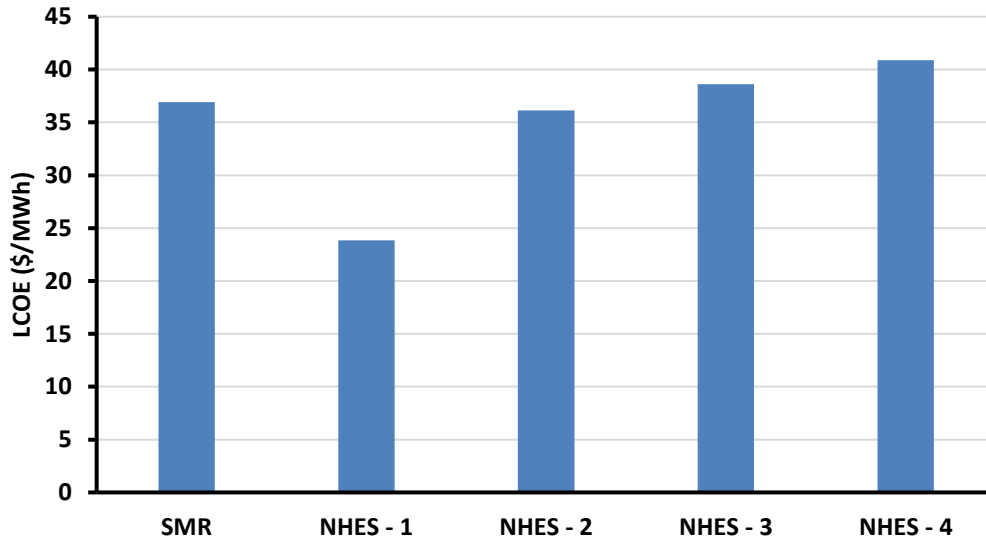


Figure 5.21 LCOE for SMR and different SMR-ChHP output scenarios

Based on the above evaluated economic parameters for different U.S. region, nuclear hybrid energy system comparing of SMR coupled with ChHP showed that selling heat to high-temperature industrial process and electricity to the grid makes advanced SMR more profitable and helps reducing the burning of fossil fuels to produce heat. In the California, Midwest, Northwest, and Southwest regions, it is more profitable to have NHES-3 or 4 compared with NHES-1 and 2 and advanced SMR based on PBP and DCFR values. Though based on high NPV values, NHES-1 can also be considered. In PJM and New England, NHES-1 is more profitable based on their utility prices, asserting selling heat at higher scale is more cost-effective and favorable.

#### 5.4.2 Parametric Study on Overnight Capital Cost of Advanced SMR

To assess the economic competitiveness of advanced SMR and different SMR-ChHP systems, a parametric study on OCC of advanced SMR is conducted for the values ranging from \$4500/kW<sub>e</sub> to \$6,500/kW<sub>e</sub> based on the diverse values reported in literature. The aim of this parametric study is to assess the effect on NPV and PBP of the proposed scenarios for different

utility prices and U.S. regions. Advanced SMR, NHES-1, and NHES-2 will be the focus of this study based on results discussed in Section 5.4.1.

Fig. 5.22, 5.23, 5.24, and 5.25 show the NPV and PBP values at different OCC of advanced SMR for California, Midwest, Northwest, and Southwest, respectively. As the OCC of advanced SMR is increased the NPV of the SMR, NHES-1 and 2 decreased as expected with increase in PBP. For the California, Midwest, Northwest, and Southwest regions, NPV of NHES-1 and 2 are still positive and higher than advanced SMR value when the OCC of advanced SMR is increased from \$4500/kW<sub>e</sub> to \$6,500/kW<sub>e</sub>.

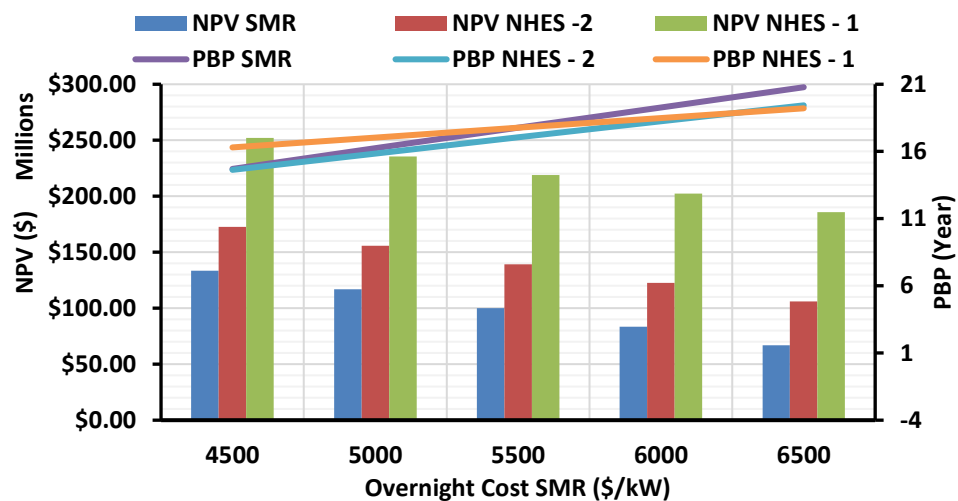


Figure 5.22 NPV and PBP versus overnight cost of advanced SMR for the California region. For California, the PBP starts to get lower for NHES-2 and NHES-1 when compared with advanced SMR once the OCC of SMR is more than \$5,500/kW<sub>e</sub> and \$6,100/kW<sub>e</sub>, respectively. Based on utility data from the Midwest region, the PBP of NHES-2 and NHES-1 when compared with advanced SMR begins to reduce once the OCC of SMR is increased to \$4,500/kW<sub>e</sub> and \$5,500/kW<sub>e</sub>, respectively. The PBP for the Northwest region was already less for NHES-1 when compared with SMR for \$4,500/kW<sub>e</sub> OCC. When the OCC is increased to \$4,800/kW<sub>e</sub> the NHES-1 system had less PBP than advanced SMR. The Southwest region, NHES-1 would not have lower PBP than advanced SMR based on assumed OCC. NHES-2 will have PBP lower than advanced SMR once the OCC is increased to \$5,800/kW<sub>e</sub>.

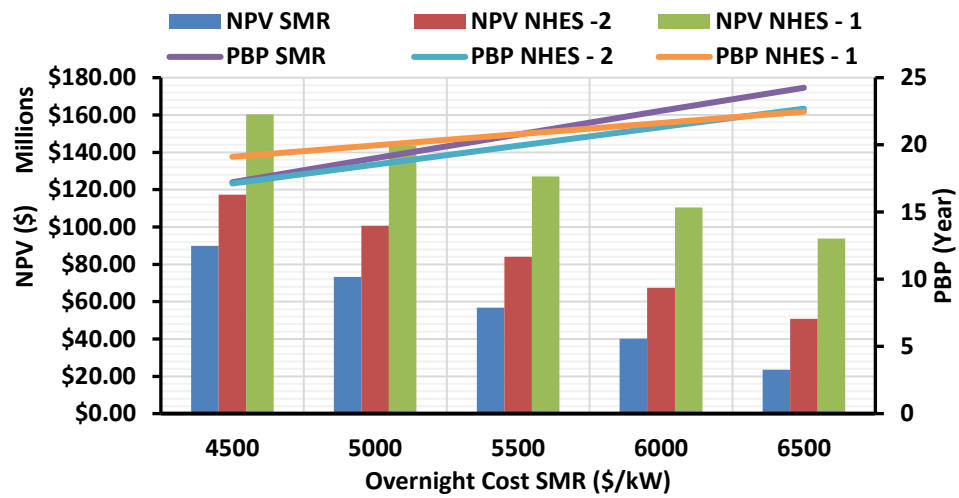


Figure 5.23 NPV and PBP versus overnight cost of advanced SMR for the Midwest region

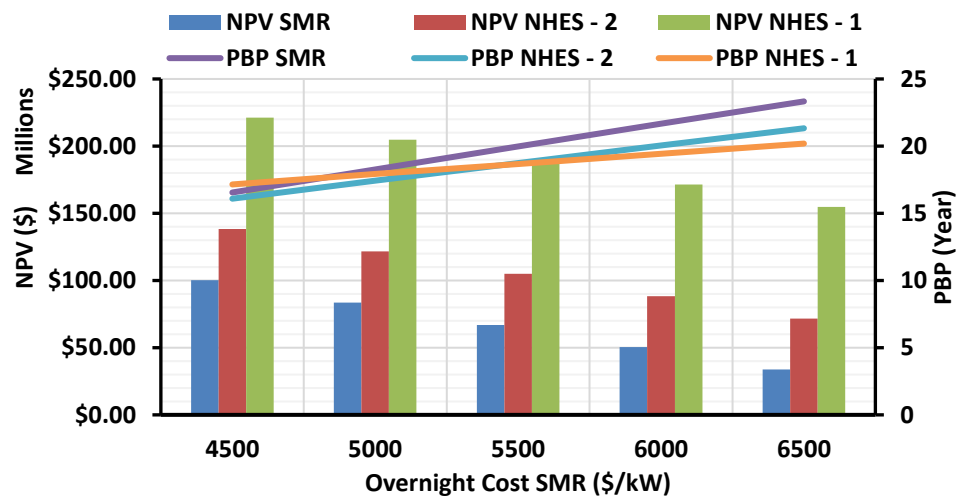


Figure 5.24 NPV and PBP versus overnight cost of advanced SMR for the Northwest region

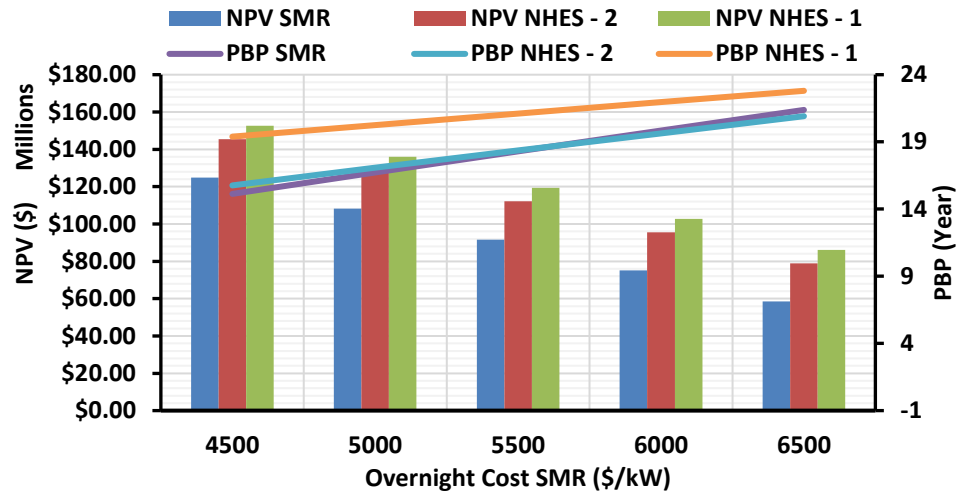


Figure 5.25 NPV and PBP versus overnight cost of advanced SMR for Southwest region

Figs. 5.26 and 5.27 show the NPV and PBP values at different OCC of advanced SMR for New England and PJM, respectively. Based on the New England and PJM utility prices, NHES-1 will always shave lower PBP when compared with NHES-2 and advanced SMR with increased OCC though the individual system PBP value will increase. NPV of both the regions are significantly higher for NHES-1. If the OCC is increased above \$5,500/kWe and \$5,000/kWe for New England and PJM, respectively, then NPV of SMR will become negative making SMR not profitable. In this case, the system will be economic profitable if SMR is coupled with ChHP and sells heat and electricity.

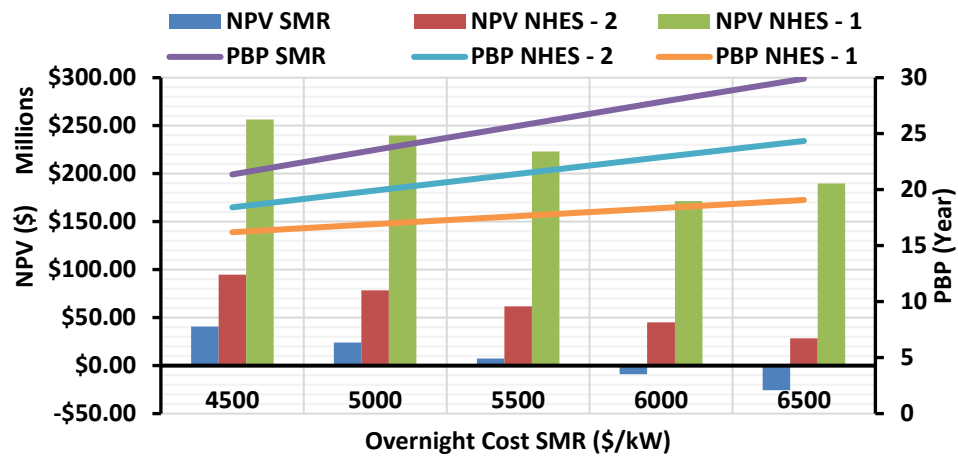


Figure 5.26 NPV and PBP versus overnight cost of advanced SMR for the New England region

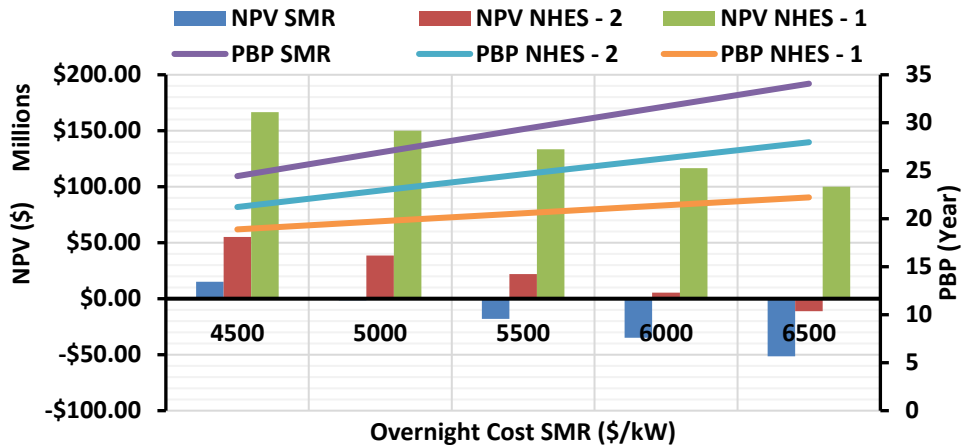


Figure 5.27 NPV and PBP versus overnight cost of advanced SMR for the PJM region

### 5.4.3 Impact of Increased Carbon Taxes

The goal to prevent global temperature from rising above 1.5°C by 2030, which was committed at COP26, the price of carbon tax should be higher. This tax reduces emissions in two ways. First, increasing the cost of carbon-based fuels will motivate to switch to clean energy technologies, such as nuclear, solar, wind, and hydro sources. Taxes will allow industries to find most cost-effective way to reduce emissions, which is a better alternative to free-market

economies than government regulation. This study was conducted to analyze the impact of increased carbon taxes on PBP for NHES (SMR-ChHP) systems.

The two-carbon tax rates were assumed in this study (e.g., \$150/tonne) (which was assumed in Section 5.4.1) and \$200/tonne. As carbon tax rate will impact the heat value that is why different NHES scenarios are studied for different U.S. regions. All the assumption were unchanged except carbon tax. As NPVs of the NHES systems were significantly higher than advanced SMR for all the scenarios and cases, PBP was the focus of this study. For the California region, the percentage deviation of PBP with different carbon taxes were shown in Fig. 5.28 for different NHES systems when compared with advanced SMR. When carbon tax of \$150/tonne was assumed, NHES-1 had 9.1% higher PBP than advanced SMR but as the carbon tax increased to \$200/tonne the PBP was reduced to -3.5% than advanced SMR. PBP of NHES-2, 3, and 4 systems were further lowered than advanced SMR values when carbon tax were increased to \$150/tonne to \$200/tonne. Similar trend was followed by the Midwest region as shown in Fig. 5.29 where PBP of NHES-2, 3 and 4 systems were further lowered than advanced SMR values when carbon tax were increased. Whereas the NHES-1 had 9.2% higher payback period compared with SMR value at \$150/tonne carbon tax and this value was lowered to -5.4% when carbon tax was increased to \$200/tonne.

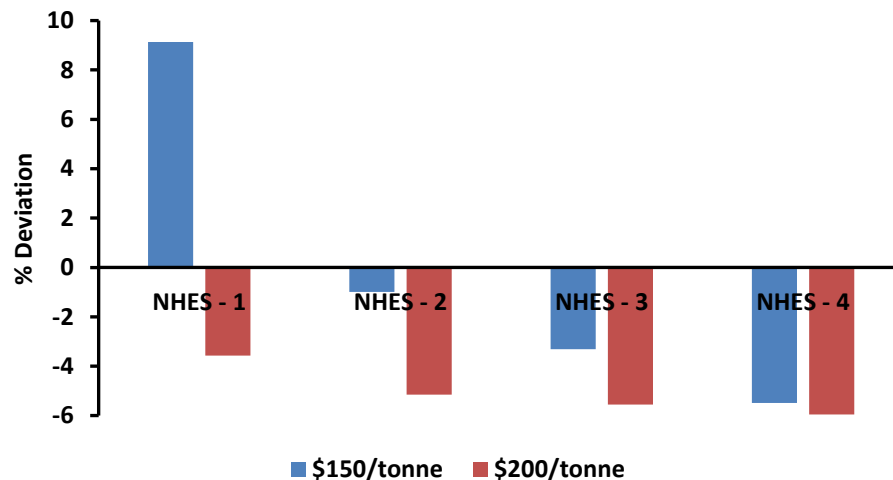


Figure 5.28 Percentage deviation in PBP based on increased carbon tax for the California region

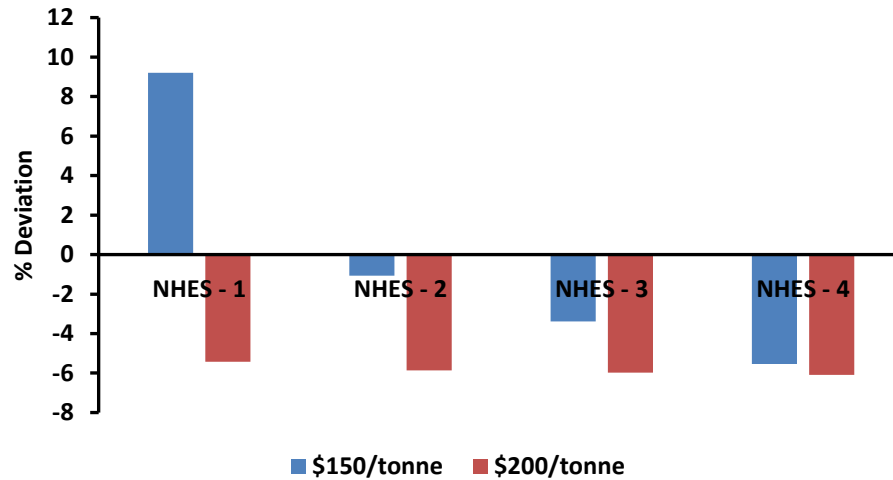


Figure 5.29 Percentage deviation in PBP based on increased carbon tax for the Midwest region

For the Northwest region, the percentage deviation in PBP values for NHES-2, 3, and 4 were further lowered as expected compared with SMR when carbon tax was increased as shown in Fig. 5.30. But for NHES-1, the PBP was 2% higher and was reduced to -10.45% compared with SMR when the carbon tax was increased from \$150/tonne to \$200/tonne, respectively. In the Southwest region, as shown in Fig. 5.31, even after increasing the carbon tax to \$200/tonne, PBP of NHES-1 was still higher than advanced SMR value. Though PBP of NHES-2, 3, and 4 systems were lowered than SMR values with increased carbon tax.

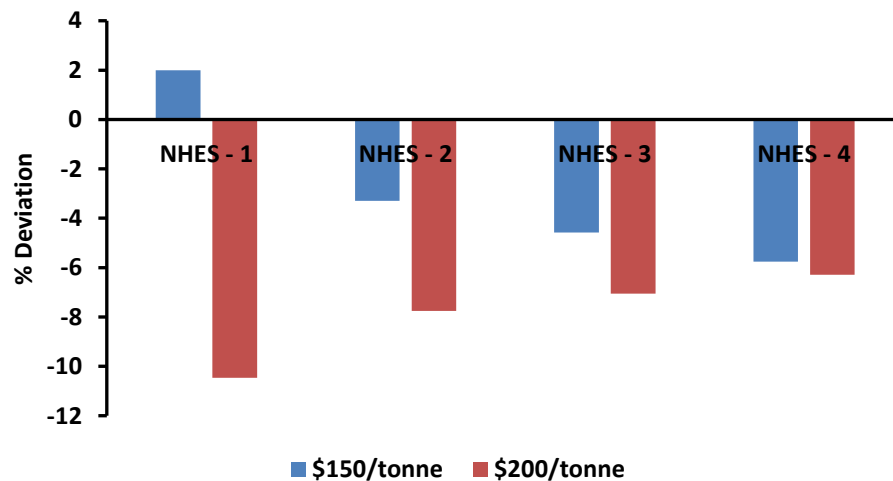


Figure 5.30 Percentage deviation in PBP based on increased carbon tax for the Northwest region

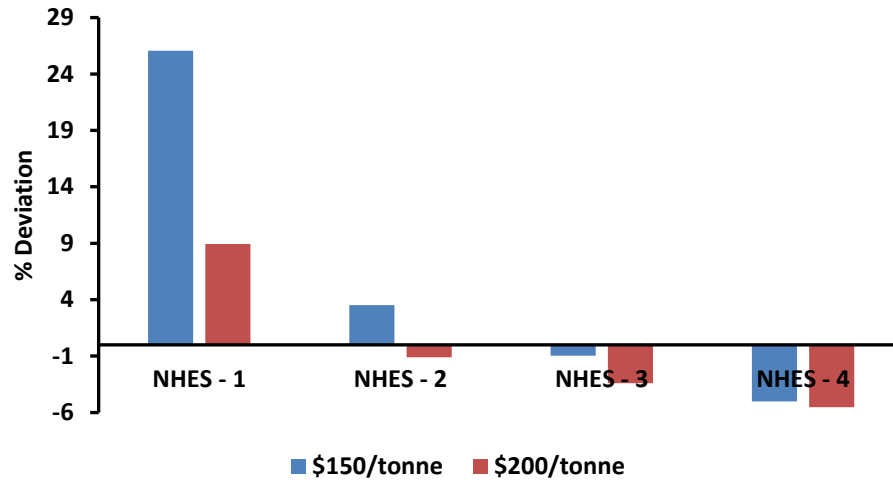


Figure 5.31 Percentage deviation in PBP based on increased carbon tax for the Southwest region

The New England and PJM were the two most profitable cases for the NHES-1 system as per the study described in Section 5.4.1. Increasing the carbon tax rate has further lowered the PBP from -25.35% to -34.04% and -22.88% to -34% from SMR values for New England and PJM regions, respectively, as shown in Figs. 5.32 and 5.33.

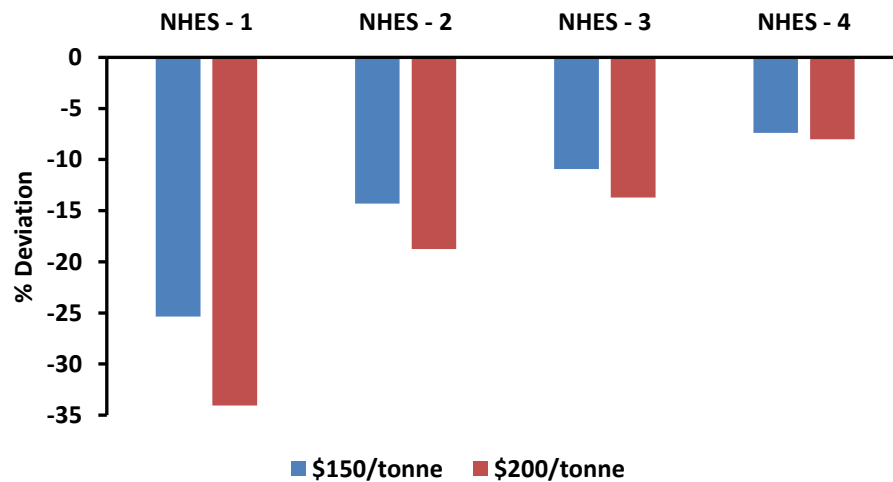


Figure 5.32 Percentage deviation in PBP based on increased carbon tax for the New England region

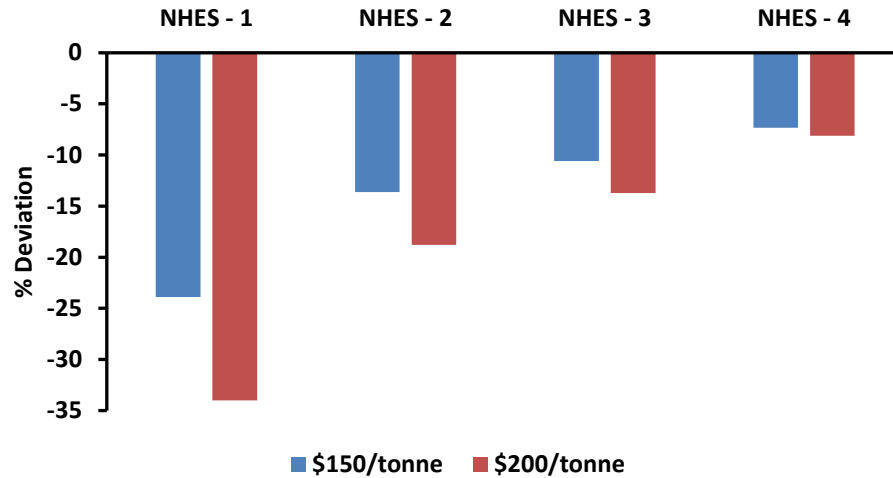


Figure 5.33 Percentage deviation in PBP based on increased carbon tax for the PJM region

### Nomenclature

$\bar{A}$	average annuity	\$
$A$	annuity	\$
$A_{HT}$	heat transfer area	$m^2$
$C$	rate	-
$CC$	contingency cost rate	-
$CF$	capacity factor	-
$c_0$	costs	\$
$DCFR$	discounted cash flow rate of return	-
$DD\&E$	detailed design and engineering rate	-
$d$	depreciation rate	-
$E$	energy	MWh
$Fuel_{spec}$	specific fuel cost	$\$ MW_e^{-1}$
$h_c$	convective heat transfer coefficient	$W m^{-2} K^{-1}$
$ID$	inner diameter	m
$i$	discount rate	-
$k$	thermal conductivity	$W m^{-1} K^{-1}$
$LCOE$	levelized cost of energy	$\$ MW^{-1} h^{-1}$
$L$	length	m

$NPV$	net present worth	\$
$Nu$	Nusselt number	-
$N$	time period	yr
$n$	number or magnitude	-
$O\&M_{fix}$	fixed operations and maintenance	$\$ MW_e^{-1} yr^{-1}$
$O\&M_{spec}$	specific operation and maintenance	$\$ MW_e^{-1}$
$OCC$	overnight capital cost	$\$ kW_e^{-1}$
$OD$	outer diameter	m
$PBP$	payback period	yr
$Pr$	Prandtl number	-
$PWF$	present worth factor	-
$p$	portion	-
$\dot{Q}$	heat transfer rate	W, MW
$Re$	Reynolds number	-
$r$	rate	-
$R_c$	thermal contact resistance	$m^2 K W^{-1}$
$rec$	recovered cost from salvaged equipment	\$
$SP$	selling price of utility	$\$ MW^{-1} h^{-1}$
$SCC$	specific capital cost	$\$ kW_e^{-1}$
$T$	annual investment	\$
$T$	temperature	$^{\circ}C$
$t$	thickness	m
$U$	overall heat transfer coefficient	$W m^{-2} K^{-1}$
$u$	velocity	$m s^{-1}$
$V_{bed}$	volume of bed	$m^3$
$\dot{V}$	volumetric flow rate	$m^3 s^{-1}$
$V$	fixed capital investment	\$
$WACC$	weighted average capital cost	-

*Greek Letters*

$\Delta$	change or difference	-
$\eta$	first law thermodynamic efficiency	-
$\mu$	viscosity	$\text{kg m}^{-1} \text{s}^{-1}$
$\Phi$	tax rate	-
$\rho$	density	$\text{kg m}^{-3}$

*Subscript/superscript*

<i>bed</i>	bed
<i>c</i>	construction
<i>cf</i>	annual cash flow
<i>d</i>	debt
<i>de</i>	dehydration
<i>eq</i>	equity
<i>e</i>	electricity
<i>f</i>	fluid
<i>ht</i>	heat
<i>hy</i>	hydration
<i>inf</i>	inflation
<i>j</i>	plant operation year index
<i>k</i>	plant operation year index
<i>th</i>	thermal
<i>v</i>	investment

## References

1. M. Schmidt, C. Szczukowski, C. Roßkopf, M. Linder, and A. Wörner. 2014. "Experimental results of a 10 kW high temperature thermochemical storage reactor based on calcium hydroxide," *Applied Thermal Engineering* 62:553–559. <https://doi.org/10.1016/j.applthermaleng.2013.09.020>.
2. M. Linder, Chr. Roßkopf, M. Schmidt, and A. Wörner. 2014. "Thermochemical Energy Storage in kW-scale based on CaO/Ca(OH)<sub>2</sub>," *Energy Procedia* 49:888–897. <https://doi.org/10.1016/j.egypro.2014.03.096>.
3. M. Angerer, M. Becker, S. Härzschel, K. Kröper, S. Gleis, A. Vandersickel, and H. Spliethoff. 2018. "Design of a MW-scale thermo-chemical energy storage reactor," *Energy Reports* 4:507–519. <https://doi.org/10.1016/j.egy.2018.07.005>.
4. M. Schmidt, M. Gollsch, F. Giger, M. Grün, and M. Linder. 2016. "Development of a moving bed pilot plant for thermochemical energy storage with CaO/Ca(OH)<sub>2</sub>," *AIP Conference Proceedings* 1734:050041. <https://doi.org/10.1063/1.4949139>.
5. A. Cosquillo Mejia, S. Afflerbach, M. Linder, and M. Schmidt. 2020. "Experimental analysis of encapsulated CaO/Ca(OH)<sub>2</sub> granules as thermochemical storage in a novel moving bed reactor," *Applied Thermal Engineering* 169:114961. <https://doi.org/10.1016/j.applthermaleng.2020.114961>.
6. P. D. Armatis, A. Gupta, P. Sabharwall, V. Utgikar, and B. M. Fronk. 2021. "A chemical-absorption heat pump for utilization of nuclear power in high temperature industrial processes," *International Journal of Energy Research* 45:14612–14629. <https://doi.org/10.1002/er.6721>.
7. Graphite & SIC Heat Exchangers | Fluoropolymers | CG Thermal. 2022. <https://cgthermal.com/> (accessed March 1, 2022).
8. M. Schmidt, A. Gutierrez, and M. Linder. 2017. "Thermochemical energy storage with CaO/Ca(OH)<sub>2</sub> – Experimental investigation of the thermal capability at low vapor pressures in a lab scale reactor," *Applied Energy* 188:672–681. <https://doi.org/10.1016/j.apenergy.2016.11.023>.
9. P. M. Timmerhaus, K. D. West, and P. Ronald. 2003. *Plant Design and Economics for Chemical Engineers*, Fifth Edition. McGraw-Hill.

10. P. Sabharwall, S. Bragg-Sitton, L. Boldon, and S. Blumsack. 2015. "Nuclear Renewable Energy Integration: An Economic Case Study," *The Electricity Journal* 28:85–95. <https://doi.org/10.1016/j.tej.2015.09.003>.
11. J. Richards, P. Sabharwall, and M. Memmott. 2017. "Economic comparison of current electricity generating technologies and advanced nuclear options," *The Electricity Journal* 30:73–79. <https://doi.org/10.1016/j.tej.2017.11.005>.
12. J. Buongiorno, M. Corradini, J. Parsons, D. Petti. 2018. "The Future of Nuclear Energy in a Carbon-Constrained World," MIT, IEEE, vol. 275.
13. W. R. Stewart, and K. Shirvan. 2022. "Capital cost estimation for advanced nuclear power plants," *Renewable and Sustainable Energy Reviews* 155:111880. <https://doi.org/10.1016/j.rser.2021.111880>.
14. L. M. Boldon and P. Sabharwall. 2014. "Small modular reactor: First-of-a-Kind (FOAK) and Nth-of-a-Kind (NOAK) Economic Analysis," INL/EXT-14-32616, Idaho National Laboratory. <https://doi.org/10.2172/1167545>.
15. IRS. 2020. Publication 946, *How To Depreciate Property*. <https://www.irs.gov/publications/p946> (accessed March 1, 2022).
16. G. Alonso, S. Bilbao, and E. del Valle. 2016. "Economic competitiveness of small modular reactors versus coal and combined cycle plants," *Energy* 116:867–879. <https://doi.org/10.1016/j.energy.2016.10.030>.
17. J. Aldersey-Williams and T. Rubert. 2019. "Levelised cost of energy – A theoretical justification and critical assessment," *Energy Policy* 124:169–179. <https://doi.org/10.1016/j.enpol.2018.10.004>.
18. EIA. 2022. U.S. Energy Information Administration. <https://www.eia.gov/index.php> (accessed March 1, 2022).
19. G. Locatelli, C. Bingham, and M. Mancini. 2014. "Small modular reactors: A comprehensive overview of their economics and strategic aspects," *Progress in Nuclear Energy* 73:75–85. <https://doi.org/10.1016/j.pnucene.2014.01.010>.
20. NEI, "Cost Competitiveness of Micro-Reactors for Remote Markets" Nuclear Energy Institute. April 15, 2019. <https://www.nei.org/resources/reports-briefs/cost-competitiveness-micro-reactors-remote-markets> (accessed November 21, 2021).

21. L. Boldon. 2015. "Sustainability Efficiency Factor: Measuring Sustainability in Advanced Energy Systems through Exergy, Exergoeconomic, Life Cycle, and Economic Analyses," PhD Thesis, Rensselaer Polytechnic Institute. <https://ui.adsabs.harvard.edu/abs/2015PhDT.....258B> (accessed March 1, 2022).

## Chapter 6 Summary and Conclusions

### 6.1 Conclusions

The  $\text{Ca(OH)}_2$ - $\text{CaO}$  system shows much promise for TCES as well as ChHP applications, necessitating accurate quantification of thermodynamics and kinetics of the dehydration and hydration processes. A modified Clausius-Clapeyron equation that incorporates the temperature dependence of thermodynamic quantities (enthalpy, entropy, and Gibbs energy) was developed to describe the equilibrium for the reversible calcium hydroxide decomposition/calcium oxide hydration reaction couple. An analysis of the effect of non-ideality of water vapor phase was also presented in the study. Fugacity coefficient values indicate that vapor-phase non-ideality can start to play a significant role at operating pressures above 2 MPa, however, it can be neglected at low and moderate pressures for all practical purposes. Incorporating the temperature dependence of enthalpy change leads to a more accurate equilibrium pressure-temperature relationship. This refined relationship has significant implications for the operation of both dehydration and hydration steps, lessening the severity in the dehydration step while requiring higher energy input to achieve a desired higher temperature in a ChHP.

TGA analysis was employed to study the isothermal decomposition of  $\text{Ca(OH)}_2$  under  $\text{N}_2$  atmosphere. Kinetic parameters were estimated based on the TGA results at different isothermal temperatures. Analysis of the experimental data indicated that the decomposition of pure  $\text{Ca(OH)}_2$  pellets reaction followed a first order kinetics with respect to  $\text{Ca(OH)}_2$  and the temperature dependence of the rate constant was described by the Arrhenius equation with an activation energy of 102.71 kJ/mol and the natural logarithm of Arrhenius constant of 14.119. The obtained parameters are in good agreement with the non-isothermal studies reported in literature.

The effect of addition of  $\text{CaTiO}_3$  as an additive with pure  $\text{Ca(OH)}_2$  in a form of composite pellet 1:0.5 and 1:1  $\text{Ca(OH)}_2$ : $\text{CaTiO}_3$  (by wt. %) on kinetic parameters was also studied. The results indicated that the rate of decomposition increased significantly for the composite pellets. The first order rate constant for 1:0.5  $\text{Ca(OH)}_2$ : $\text{CaTiO}_3$  had activation energy of 112.52 kJ/mol and the natural logarithm of Arrhenius constant of 16.356. The values of these parameters for 1:1  $\text{Ca(OH)}_2$ : $\text{CaTiO}_3$  were 129.43 kJ/mol and 19.356, respectively. The

addition of  $\text{CaTiO}_3$  likely facilitated the decomposition through an increasing in the reaction surface area. The XRD analysis of pellets before and after the reaction indicated that the  $\text{CaTiO}_3$  acted as an inert agent. The compressive strength test showed that composite pellets have higher mechanical strength. The obtained kinetics can be used in the design, simulation, and experimentation of bench- and larger-scale systems.

The reversible reaction system calcium hydroxide decomposition – hydration of calcium oxide was studied to understand its potential for thermal energy storage and thermoamplification. The decomposition study in the TGA-DSC apparatus showed that optimum heating rate ranged from 10-15 K/min for decomposition of  $\text{Ca}(\text{OH})_2$ .

The addition of  $\text{CaTiO}_3$  likely facilitated the decomposition through an increasing in the reaction surface area. Temperature amplification of  $\sim 180\text{-}190^\circ\text{C}$  was achieved in the bench scale experiment during hydration reaction with composite pellets (1:0.5 ::  $\text{Ca}(\text{OH})_2$ : $\text{CaTiO}_3$ ). The compressive strength test showed that composite pellets have higher mechanical strength. The addition of  $\text{CaTiO}_3$  in  $\text{Ca}(\text{OH})_2$  also resulted in enhanced reaction rate. Adding  $\text{CaTiO}_3$  to the hydroxide appears to be promising technique to construct a new advanced hydroxide-based material with improved kinetic properties for ChHP.

A steady state model was built to develop a ChHP capital cost system for pilot-scale (25-, 100-, and 1000-kW) study. A TEA was conducted for advanced SMR and SMR coupled with different thermal output ChHP system to determine the profitability of selling heat rather than electricity only. A steady-state thermal model of ChHP was used for TEA. The electricity and natural gas prices were assumed for six different U.S. regions (California, Northwest, Midwest, Southwest, New England, and PJM) based on Energy Information Administration data. For this study, advanced SMR, combined with ChHP, was referred as NHES. Advanced SMR with 100 MWth and four different scenarios of NHES were considered based on thermal output from ChHP (e.g., 50-, 10-, 5-, and 1-MWth represented as NHES-1, 2, 3, and 4, respectively). The NPV, PBP, DCFR, and LCOE were evaluated for SMR and NHES systems. The economic analysis showed that selling heat and electricity from SMR-ChHP was profitable in most cases based on utility prices of different regions. The parametric study on increasing OCC of advanced SMRs indicated selling heat will be economically profitable than selling only electricity. Increased carbon tax also showed a significant improvement in economic

parameters for configurations involving selling heat. Providing heat to the high-temperature thermal industries could be a game changer for nuclear power and help achieve the climate change goal by reducing the burning of fossil fuel.

## **6.2 Future Considerations**

Results from the bench scale experiments can be used for detailed design of pilot-scale setup which will accurately model the full-scale process. Experimental and theoretical results at pilot-scale will yield valuable information for commercial scale INHESs, thus supporting missions in enhancing the energy security, and increase the role of nuclear energy in nation's energy system.

To better understand the influence of the capital cost with greater certainty, a more extensive examination of chemical bed design is required. Process intensification and capital cost reduction may be possible with a moving bed design. The size of the ChHP should be tailored for a specific application, balancing the reduced capital cost of a smaller thermal capacity system with the higher utility sales profit of a larger thermal capacity system.